Robust and Energy-Efficient Controller Design for a Quad-Rotor Helicopter

（４ロータヘリコプタのロバスト省エネルギー制御）

July, 2015

Doctor of Engineering

BAMBANG SUMANTRI

Toyohashi University of Technology

Doctor of Engineering Thesis

in

Robotics and Mechatronics Laboratory

Department of Mechanical Engineering

Toyohashi University of Technology

Author:

Bambang Sumantri

Supervisor:

Prof. Naoki Uchiyama

Committee members:

Prof. Kazuhiko Terashima

Prof. Shinichi Suzuki

Abstract

Unmanned aerial vehicles (UAVs) have been used for many applications such as surveillance, traffic monitoring, and monitoring areas surrounding a damaged nuclear plant, where the risks to a pilot are relatively high. Rotorcrafts have advantages over fixed-wing UAVs in numerous applications because of their vertical take-off and landing capability and their augmented payload capacity. A quad-rotor helicopter (quadcopter) is a rotorcraft that has many advantages over a conventional helicopter. These include compactness, simple mechanical parts, and high maneuverability. In addition, a quadcopter provides a larger lift-thrust force than a conventional helicopter, and the payload capacity is greater. However, the quadcopter has highly nonlinear, time-varying behavior and is always influenced by unpredictable disturbances such as wind gusts, particularly in outdoor applications. Therefore, a robust control strategy is required to achieve good performance during autonomous flight. For most applications, the quadcopter is provided with a limited power source. Therefore, an energy-efficient controller is useful for extending its operating time.

In this thesis, robust and energy-efficient control strategies are designed on the basis of the sliding mode control algorithm. An underactuated problem, which occurs in the dynamics of the quadcopter, is solved by designing a cascade control structure that consists of two control loops: an inner loop and an outer loop. The inner loop handles the rotational motion of the quadcopter, whereas the outer loop handles translational motion. A least squares algorithm is utilized to solve an overdetermined problem in the translational dynamics; therefore, all motions are considered for calculating the control inputs. This control structure has a general structure; thus, it can be used for designing any control algorithm for the quadcopter.

First, to design a robust controller, we design a standard sliding mode control algorithm. Energy savings are attempted by reducing chatter, which is a common problem in sliding mode control design, by designing a thin boundary layer around the sliding surface. This technique is effective in reducing energy consumption, which is experimentally evaluated using an experimental quadcopter testbed. However, the robustness of the sliding mode control is reduced because within the boundary layer, the discontinuous control law is replaced with a continuous one. Nevertheless, the discontinuous control law provides robustness in the sliding mode control strategy. Second, we improve the performance of the sliding mode control strategy by designing the nonlinear sliding surface. We propose two nonlinear sliding surfaces, which have different characteristics. The first nonlinear sliding surface is designed to reduce the time-constant if the error increases; therefore, the control system responds faster to reduce the error. If the error converges to zero, the time-constant increases and converges to a constant value. Conversely, the second nonlinear sliding surface is designed to increase the time-constant when the error increases, and the time-constant converges to a constant value if the error decreases to zero.

These techniques are also effective in reducing the energy consumption in the condition of a disturbance, which is evaluated in the experiment.

Reducing the chatter and designing the nonlinear sliding surfaces are effective in reducing the energy consumption in the sliding mode control strategy. However, it is also important to maintain the discontinuous control input that causes the chatter, because it provides robustness in the sliding mode condition. A second-order sliding mode control with a super-twisting algorithm (STA) provides a good solution for reducing the chattering phenomenon by maintaining the discontinuous control portion. The discontinuous control input occurs in the second-order time-derivative of the sliding surface function, whereas in the standard sliding mode control strategy, it occurs in the first-order time-derivative. However, the original STA provides strong behavior only around the origin of the sliding surface. To also provide a strong behavior when the states are far from the origin of the sliding surface, a generalized-STA is designed to include a linear stabilizing term. Furthermore, to reduce the energy consumption during the control operation, we utilize the nonlinear sliding surface. The robustness and energy efficiency of the generalized-STA with the nonlinear sliding surface are experimentally evaluated using an experimental quadcopter testbed.

Contents

Abstract **v**

Contents **vii**

List of Figures **xi**

List of Tables **xv**

1 Introduction **1**
1.1 Introduction 1
1.1.1 Background 1
1.1.2 Control of a Quad-Rotor Helicopter 3
1.1.3 Sliding Mode Control 3
1.2 Motivation and Research Objectives 5
1.3 Thesis Contributions 5
1.4 Thesis Organization 5

2 Modeling of Quadcopter and Experimental Setup **7**
2.1 Modeling of Quadcopter 7
2.1.1 Kinematics Modeling 7
2.1.2 Dynamics Modeling 10
2.2 Experimental Setup 12
2.2.1 Sensor Configuration and Coordinate Frame 13
2.2.2 Actuator Dynamics 16
2.2.2.1 Thrust Force 16
2.2.2.2 Electric Power Consumption 16
2.2.3 Experimental Testbed Parameters 18

3 Closed-Loop Controller Configuration and Velocity States Estimation **21**
3.1 Introduction 21
3.2 Dynamics Decoupling 22
3.3 Closed-Loop Configuration 22
3.3.1 Control Input Calculation 23
3.3.1.1 Translational Motion 23
3.3.1.2 Rotational Motion 24
3.4 Design of Reduced-Order Observer 24
3.5 Experiment 25

3.5.1 PID Controller Design 25
3.5.2 Experimental Results 26
3.6 Conclusion 33

4 Chatter Reduction in Sliding Mode Control for Energy Saving Controller of a Quad-Rotor Helicopter 35
4.1 Introduction 35
4.2 Controller Design 36
4.2.1 Design of Sliding Surface 36
4.2.2 Sliding Mode Control 37
4.3 Stability Analysis 38
4.3.1 Existence of Sliding Mode 38
4.3.2 Stability of Sliding Surface 39
4.3.2.1 PD-based Sliding Surface 39
4.3.2.2 PID-based Sliding Surface 40
4.4 Experiments 40
4.4.1 Robustness Evaluation 40
4.4.2 Power and Energy Evaluation 59
4.5 Conclusion 63

5 Robust Tracking Control of a Quad-Rotor Helicopter Utilizing Sliding Mode Control with a Nonlinear Sliding Surface 65
5.1 Introduction 65
5.2 Control System Design 66
5.2.1 Nonlinear Sliding Surface Design 66
5.2.2 Controller Design Via Lyapunov Stability Analysis 68
5.3 Experimental Results 70
5.3.1 Robustness Evaluation 71
5.3.2 Power and Energy Evaluation 80
5.4 Conclusion 81

6 A Nonlinear Sliding Surface for the Second-Order Sliding Mode Control 83
6.1 Introduction 83
6.2 Development of Control System 84
6.2.1 Sliding Surface Equation 84
6.2.2 Stability of Sliding Surface 85
6.2.3 Controller Design 86
6.2.4 Existence of Sliding Mode 87
6.2.5 Closed Loop Configuration 88
6.3 Experimental Results 89
6.3.1 Robustness Evaluation 89
6.3.2 Energy Evaluation 105
6.4 Conclusion 109

7 Summary and Future Works 111
7.1 Summary 111
7.2 Future Works 114

A Overview of reduced-order observer **117**

Bibliography **119**

Publications **127**

Acknowledgements **129**

List of Figures

2.1 Coordinate system of a quadcopter. 8
2.2 Experimental quadcopter testbed 13
2.3 Sensors placement on the experimental quadcopter testbed: (a) actual configuration, (b) schematic 15
2.4 Frame transformation on the experimental quadcopter testbed 16
2.5 Applied voltages versus thrust force of a rotor. 17
2.6 Electric power of a motor during the hovering motion. 17
2.7 Total energy consumed by a motor during the hovering motion. 18

3.1 Closed-loop controller configuration for a quadcopter. 22
3.2 Closed-loop controller configuration with observer for the experimental quadcopter testbed. 25
3.3 3-dimensional desired trajectory. 27
3.4 Velocity profiles obtained from a reduced-order observer and a backward-difference method. 28
3.5 Tracking control results by PID control with a reduced-order observer. 29
3.6 Tracking control results by PID control with a backward-difference method. . . 30
3.7 Tracking error with a reduced-order observer and a backward-difference method. 31
3.8 RMSE and error variance with a reduced-order observer and a backward-difference method. 32

4.1 Desired trajectory in $x-y-z$ coordinate system. 41
4.2 Profiles of sliding surface for each DOF. 42
4.3 Trajectory tracking results in all motion for controllers C1, C2, and C3 without disturbance. 45
4.4 Tracking error for controllers C1, C2, and C3 without wind disturbance. 46
4.5 Tracking error for controllers C1, C2, and C3 under wind disturbance. 47
4.6 Tracking error for controllers C4, C5, and C6 without disturbance. 48
4.7 Tracking error for controllers C4, C5, and C6 under wind disturbance. 49
4.8 Profiles of control input for controllers C1, C2, and C3 (a) without disturbance, (b) under wind disturbance. 50
4.9 Profiles of control input for controllers C4, C5, and C6 (a) without disturbance, (b) under wind disturbance. 51
4.10 Mean and variance of control input for multiple times experiments for controllers C1, C2, and C3 without disturbance. 52
4.11 Mean and variance of control input for multiple times experiments for controllers C1, C2, and C3 under wind disturbance. 53
4.12 Mean and variance of control input for multiple times experiments for controllers C4, C5, and C6 without disturbance. 54

4.13 Mean and variance of control input for multiple times experiments for controllers C4, C5, and C6 under wind disturbance. 55
4.14 RSME and error variance for multiple times experiments for controllers C1, C2, and C3 without disturbance. 56
4.15 RSME and error variance for multiple times experiments for controllers C1, C2, and C3 under wind disturbance. 57
4.16 RSME and error variance for multiple times experiments for controllers C4, C5, and C6 without disturbance. 58
4.17 RSME and error variance for multiple times experiments for controllers C4, C5, and C6 under wind disturbance. 59
4.18 Profiles of power on each motor for controllers C1, C2, and C3 (a) without disturbance, (b) under wind disturbance. 61
4.19 Profiles of power on each motor for controllers C4, C5, and C6 (a) without disturbance, (b) under wind disturbance. 62
4.20 Total energy consumption of the motors; (a) controllers C1, C2, and C3 without disturbance; (b) controllers C1, C2, and C3 under wind disturbance; (c) controllers C4, C5, and C6 without disturbance; (d) controllers C4, C5, and C6 under wind disturbance. 63

5.1 Characteristic of LSS, NSS-1, and NSS-2. 67
5.2 Profiles of sliding surface functions for LSS, NSS-1, and NSS-2. 67
5.3 Profiles of damping ratio and natural frequency for SMC with NSS-1, NSS-2, and LSS. 70
5.4 Trajectory tracking without disturbance 73
5.5 Tracking error without disturbance 74
5.6 Trajectory tracking under wind disturbance 75
5.7 Tracking error under wind disturbance 76
5.8 RSME and error variance in several times experiments without disturbance . . 77
5.9 RSME and error variance in several times experiments under wind disturbance 78
5.10 Profiles of control inputs in the experiment without disturbance 79
5.11 Profiles of control inputs in the experiment under wind disturbance 79
5.12 Profiles of power on each motor in the experiment without disturbance 80
5.13 Profile of power on each motor in the experiment under wind disturbance . . . 81
5.14 Total energy consumed by the actuators in several times experiments: (a) without disturbance; (b) under wind disturbance. 81

6.1 Profiles of sliding surface without disturbance 90
6.2 Profiles of sliding surface under wind disturbance 91
6.3 Trajectory tracking without disturbance 93
6.4 Trajectory tracking under wind disturbance 94
6.5 Tracking error and its distribution without disturbance 95
6.6 Tracking error and its distribution under low wind disturbance 96
6.7 Tracking error and its distribution under high wind disturbance 97
6.8 RSME and error variance for experiments without disturbance 98
6.9 RSME and error variance for experiments under low wind disturbance 99
6.10 RSME and error variance for experiments under high wind disturbance 100
6.11 Profiles of Ψ and $\dot{\Psi}$ in experiment without disturbance 101
6.12 Profiles of Ψ and $\dot{\Psi}$ in experiment under low wind disturbance 102

6.13 Profiles of closed-loop properties in experiment without wind disturbance . . . 103
6.14 Profiles of closed-loop properties in experiment under low wind disturbance . . 104
6.15 Profiles of closed-loop properties in experiment under high wind disturbance . 105
6.16 Profiles of control inputs in experiment without disturbance 106
6.17 Profiles of control inputs in experiment under low wind disturbance 107
6.18 Profiles of power applied on each actuator in experiment without disturbance . 107
6.19 Profiles of power applied on each actuator in experiment under low wind disturbance 108
6.20 Profiles of energy; (a) without disturbance; (b) under low wind disturbance; (c) under high wind disturbance. 109

List of Tables

2.1 Components of experimental testbed. 18
2.2 Parameters of quadcopter experimental testbed. 19

3.1 Average of RSME and error variance (Var) for all trials in Fig. 3.8. 33

4.1 Mean and variance of control input for experiment without disturbance. 43
4.2 Mean and variance of control input for experiment under wind disturbance. . . 43
4.3 Root-squared of mean error (RSME) and error variance (Var) for experiment without disturbance. 44
4.4 Root-squared of mean error (RSME) and error variance (Var) for experiment under wind disturbance. 44

5.1 Average of root-squared of mean error (RSME) and error variance (Var) for experiments without disturbance. 72
5.2 Average of root-squared of mean error (RSME) and error variance (Var) for experiments under wind disturbance. 72

6.1 Average of root-squared mean error (RSME) and error variance (Var) for experiments without disturbance. 92
6.2 Average of root-squared mean error (RSME) and error variance (Var) for experiments under low wind disturbance. 92
6.3 Average of root-squared mean error (RSME) and error variance (Var) for experiments under high wind disturbance. 92

7.1 Root-squared mean error (RSME) and error variance (Var) for experiment without disturbance. 113
7.2 Root-squared mean error (RSME) and error variance (Var) for experiment under wind disturbance. 113
7.3 Total energy consumption during the control operation. 114

Chapter 1

Introduction

1.1 Introduction

1.1.1 Background

In recent years, unmanned aerial vehicles (UAVs) have attracted significant attention because of their wide range of applications. UAVs provide many advantages over a piloted aircraft, particularly for applications in areas in which it is difficult or dangerous for humans to operate, such as monitoring the disaster areas of a damaged nuclear plant. They also have lower costs than manned vehicles for many applications such as surveillance, traffic monitoring, aerial photography, and inspection. Rotorcrafts have advantages over fixed-wing UAVs in numerous applications because of their vertical take-off and landing capability, stationary flight capability, and augmented payload capacity. A quad-rotor helicopter (quadcopter) is a rotorcraft that has many advantages over a conventional helicopter, including compactness, simple mechanical parts, and high maneuverability. Maneuvers are performed by simply varying the speed of its propellers. In addition, the quadcopter provides a larger lift-thrust force than a conventional helicopter, and payload capacity is greater. These advantages qualify the quadcopter as a good platform for autonomous UAV research.

However, in most applications, the quadcopter is provided with a limited power source. Therefore, the energy consumption should be considered. If energy can be saved during its operation, we can lengthen the operating time. Some studies have been conducted to minimize the energy consumption of a quadcopter. Roberts *et al.* tackled the energy problem related to aerial exploration in indoor environments using a ceiling attachment feature to maintain a bird's-eye view, while allowing the actuators to be shut down; thus, energy can be saved in the performance of an indoor task because the propellers are stopped [1]. However, this feature is not applicable for

outdoor applications. Aleksandrov and Penkov optimized the energy of a quadcopter by evaluating the optimal gap distance between the rotors of a quadcopter to obtain the optimal thrust from all rotors [2]. Fresk and Nikolakopoulos designed variable-pitch propellers to replace the fixed-pitch propeller to make the quadcopter's actuators power efficient [3]. However, most studies on energy saving for a quadcopter do not discuss the control algorithm, excluding the design of the quadcopter's platform or mechanical parts.

A quadcopter is categorized as an underactuated system because it has six degrees of freedom (DOF) with only four independent inputs (the inputs number are less than the DOF number). Consequently, it is not possible to control all the DOF directly and simultaneously. In general, two control structures are developed for the quadcopter. The first control structure is based on a block control structure [4–12]. This structure divides the dynamics of the quadcopter into two main blocks: a fully actuated block that consists of dynamics for altitude and heading motions and an underactuated block that consists of longitudinal and latitudinal motions. The control inputs of the fully actuated dynamics are designed independently, whereas the underactuated dynamics needs a further strategy such as backstepping or block control technique. The second control structure is a cascade control structure, which constructs the control system into two loops: an outer loop and an inner loop [13–24]. In this structure, the dynamics of the quadcopter is divided into two subsystems: translational dynamics (3-DOF) and rotational dynamics (3-DOF). The rotational dynamics is fully actuated and designed in the inner loop, whereas the translational dynamics is underactuated and designed in the outer loop. First, to handle the underactuated parts, the desired outputs are selected as a translational motion coordinate position and heading. Therefore, the outputs number is equal to the inputs number that is four. The outer loop provides one control input for translational motion and the desired attitude for the inner loop through an algebraic calculation.

However, the second control structure is simpler than the first one because all motions can be treated in the same manner. Therefore, it is possible to use a general method to design the control law for all motions simultaneously. In the translational motion dynamics of the quadcopter, there are three equations with only one control input. Therefore, to obtain the control input, an overdetermined problem occurs. In the references, the control input for translational dynamics is usually solved by taking into account the equation for altitude motion only, which is fully actuated or assuming a zero angle heading. However, it is useful if the control input is calculated by considering all motions and actual states so that an optimal control input is obtained.

1.1.2 Control of a Quad-Rotor Helicopter

A quadcopter has highly nonlinear and time-varying behavior. It is also influenced by unpredictable disturbances such as wind gusts, particularly in outdoor applications. Therefore, controller design and stabilization to make the quadcopter fully autonomous remain challenging problems. Many control strategies have been proposed to date. Linear control strategies have been proposed and implemented in references [25–33]. Pounds *et al.* designed a proportional-integral-differential (PID)-based controller to regulate the quadcopter attitude [27, 28]. Bouabdallah *et al.* designed a linear quadratic (LQ) controller and compared it with a classical PID controller [29]. A PD-based controller was designed in [30, 31] and a PI-based controller was proposed in [32].

Nonlinear control strategies have also been attempted by many researchers. Feedback linearization methods were utilized for controlling a quadcopter in references [14, 18–20, 34–37]. In [18–20], feedback linearization combined with an observer was utilized to reduce the sensor parts. Feedback linearization was designed to control a partially dynamic system based on a fully actuated subsystem and combined with an observer to obtain translational motion information. Mian and Daobo utilized feedback linearization coupled with a PD controller for controlling the translational motion of a quadcopter [22]. They also designed a backstepping-based PID nonlinear controller for rotational motion. A backstepping method was also presented in [23, 38]. Saturation nonlinearity, known as nested saturation, was also being examined by researchers to consider the input saturation [11, 39–41].

However, linear-based controller or feedback linearization strategies cannot deal with the uncertainty of the quadcopter dynamics and disturbances as well. Sliding mode control (SMC) is a renowned control strategy because of its robustness against disturbances, uncertainty, unmodeled dynamics, and invariance during the sliding mode condition. This control strategy has also been applied to a quadcopter in references [4, 6–8, 10, 12, 14, 17, 21, 24, 42–55]. In [17, 24, 50], SMC was combined with an observer to increase control performance against an external disturbance. SMC based on the block control technique was developed in [4, 10] to solve the underactuated problem.

1.1.3 Sliding Mode Control

Sliding mode control is a class of variable structure control that was first introduced in the early 1950's and received much attention after it was published in [56, 57]. SMC is attractive as a robust controller because of its invariance property, by which the system is completely insensitive to parametric uncertainty and external disturbances [58], with a relatively simple design. Design of SMC involves two important steps: (1) the design of a stable sliding surface

by considering the desired closed-loop performance and (2) the design of an appropriate control law to provide the robustness.

The design of a sliding surface can determine the performance of the overall closed-loop dynamics of the control system. The basic sliding surface design is based on a linear differential function with a proportional gain [59, 60]. To improve the tracking performance, an integrator is added in [61, 62]. Gain parameters of the sliding surface govern the performance of the controller. A larger gain makes the response of controller fast; however, the system may be unstable and contrarily, whereas a smaller gain makes the response of controller slow; however, the system is more stable [63]. To improve the performance of a SMC strategy, a time-varying sliding surface was proposed in [60, 63–77]. Promkajin and Parnichkun designed an adaptive sliding surface for the attitude and altitude control of a quadcopter [60]. A fuzzy system strategy was utilized to update the sliding surface parameter in [63–66]. Salamci and Tombul designed a time-varying sliding surface based on a frozen-time approach for a nonlinear system, which behaves as a linear time-invariant system [67]. A sliding surface based on a nonlinear function was proposed in [68–77].

Although SMC provides robustness to the disturbance, in an implementation, it suffers from the chattering phenomenon caused by high-frequency bang-bang or switching control. In an ideal SMC, the controller is assumed to switch with an infinite frequency. However, in a real implementation, because of the actuator properties and finite sampling time of digital components, the switching occurs at high frequencies, which is known as chattering. The chattering at high frequencies may harm the actuator and increase the energy consumed by the system. Therefore, it is necessary to reduce the chatter in an SMC design. However, the switching-type controller, which is the source of chatter, provides the invariant property and robustness in the sliding mode condition. Substituting the switching controller with a continuous-type control in a small neighborhood or boundary layer around the sliding surface is effective in reducing the chatter [59]. Unfortunately, the invariant property, which is source of robustness, vanishes inside the boundary layer. The second-order SMC offers a promising solution for reducing the chattering phenomenon because it guarantees the existence of the invariant property [78]. Using this SMC method, the switching controller occurs in the second time-derivative of the sliding variable, whereas in the standard SMC, it occurs in the first time-derivative. The second-order SMC increases the control accuracy because it involves an integral part to obtain the control input. The super-twisting algorithm (STA) SMC becomes an interesting choice among the other second-order SMC methods because it only needs the sliding variable information, whereas the others require information of the first time-derivative of the sliding variable, which was applied to a quadcopter in [4, 6, 10, 52–54]. However, STA-SMC only provides strong behavior when the system states are close to the sliding mode condition because it only involves a nonlinear square-root part in the control law. To provide strong behavior from any initial condition, a generalized-STA (GSTA) was proposed by including a linear part in the control law [79, 80].

1.2 Motivation and Research Objectives

In its applications, the flight duration of a quadcopter is limited by the power source, which is generally from a battery. Research on the energy savings of a quadcopter mostly considers only the design of mechanical parts. However, if we are able to reduce energy consumption by changing only the control software, it is applicable to hardware currently in use. Therefore, the software approach is cost-effective and highly efficient.

To date, many control strategies have been proposed and applied the the quadcopter. These are from the linear-based controller approach to the robust control strategies. Mostly, the controller designs only consider the performance and robustness of stabilization and tracking and do not consider energy efficiency. In addition, for simplifying the controller design of a quadcopter, which is categorized as an underactuated system, a simple and general control structure is required. A cascade structure provides a simple control structure, but an overdetermined problem occurs in calculating the control input for translational motion.

Therefore, this thesis proposes a simple and general control structure for the quadcopter by considering all motion for calculating the control inputs. A robust and energy-efficient control strategy based on SMC is developed through chatter reduction and designing a nonlinear sliding surface.

1.3 Thesis Contributions

The main contributions of this thesis are as follows:

1. Design of a simple and general control structure utilizing a least-squares algorithm to solve the overdetermined problem in the translational dynamics of a quadcopter.
2. Design of a nonlinear sliding surface to change the time-constant of the control system during the sliding mode condition as a function of the tracking error.
3. Design of a robust and energy-efficient SMC strategy for a quadcopter based on GSTA-SMC with a nonlinear sliding surface.

1.4 Thesis Organization

This thesis is divided into seven chapters. A brief description of contents of each chapter is presented as follows:

- Chapter 2: In this chapter, we describe the dynamics model of the quadcopter. The experimental system of a quadcopter, which is used to demonstrate the proposed control design, is described as well as the parameters of the experimental system.

- Chapter 3: In this chapter, the control structure of the quadcopter is presented. A cascade control structure is designed by introducing a least-squares algorithm to solve the overdetermined problem in the translational motion dynamics. A reduced order observer is described and utilized for estimating the velocities of the quadcopter testbed from the measured position states. The effectiveness of the control structure and reduced-observer design are experimentally evaluated by applying a simple PID controller.

- Chapter 4: In this chapter, the SMC strategy is applied for a robust quadcopter controller. Energy saving is addressed through the controller design by chatter reduction using a boundary layer method. An integral sliding surface is utilized to improve tracking performance. The reaching rate is increased by using a constant plus proportional reaching law. The effectiveness of this approach in terms of robustness and energy consumption is evaluated by performing trajectory tracking control experiments under significant wind gusts.

- Chapter 5: In this chapter, two nonlinear sliding surfaces for SMC are presented with an opposite characteristic as a function of error. These nonlinear sliding surfaces are designed to change the time-constant within the sliding mode condition. The first nonlinear sliding surface reduces the time-constant if error increases, and if error convergences to zero, the time-constant increases to a constant number. The second nonlinear sliding surface has an opposite characteristic. The large error increases the time-constant to a maximum value, and by decreasing the error, the time-constant is reduced and converges to a minimum value. Therefore, by varying the time-constant, the tracking performance is improved. These nonlinear sliding surfaces also change the closed-loop properties of the system. In addition, these nonlinear sliding surfaces reduce energy consumption during the control operation. The effectiveness of these strategies in terms of robustness and energy efficiency are experimentally evaluated using an experimental quadcopter testbed.

- Chapter 6: In this chapter, the second-order SMC based on the generalized-STA is presented for the robust tracking control of a quadcopter. The new nonlinear sliding surface equation as a function of tracking error is introduced to reduce the energy consumption through designing a time varying properties of the closed-loop dynamics (damping ratio and natural frequency). The Lyapunov stability theory is utilized to prove the stability of the proposed method within and out of the sliding mode. The effectiveness and reliability of the proposed method are evaluated using the experimental quadcopter testbed.

- Chapter 7: In this chapter, the summary of the thesis is presented. Future works to extend this thesis are also described.

Chapter 2

Modeling of Quadcopter and Experimental Setup

In this chapter, the dynamics model of a quadcopter is described. The model is derived by utilizing the Newton-Euler formulation for a rigid-body in free motion. The experimental quadcopter testbed used in this works is explained together with the sensors configuration. The quadcopter testbed parameters are also described.

2.1 Modeling of Quadcopter

The motions of a quadcopter are achieved by using two pairs of contra-rotating rotors. One pair of rotors rotates in the clockwise direction and the other in the counter-clockwise as shown in Fig. 2.1. Forward motion is achieved by increasing the speed of rear rotors and simultaneously decreasing the speed of front rotors. Backward, leftward, and rightward motions are obtained in a similar manner. Yaw motion in one direction or another is performed by accelerating counter-clockwise rotors and simultaneously decelerating the clockwise rotors, or vice versa. To derive the model of a quadcopter, we describe its kinematics and dynamics aspects as follows.

2.1.1 Kinematics Modeling

A quadcopter is considered as a rigid body in free motion which has six degrees of freedom (6-DOF). First, let us consider two coordinate frames: an earth fixed frame $\{E\}$ and a body frame $\{B\}$ that fixed at the center of gravity of the quadcopter as shown in Fig. 2.1. Since the frame $\{B\}$ moves freely then the orientation of frame $\{B\}$ relative to frame $\{E\}$ is achieved by

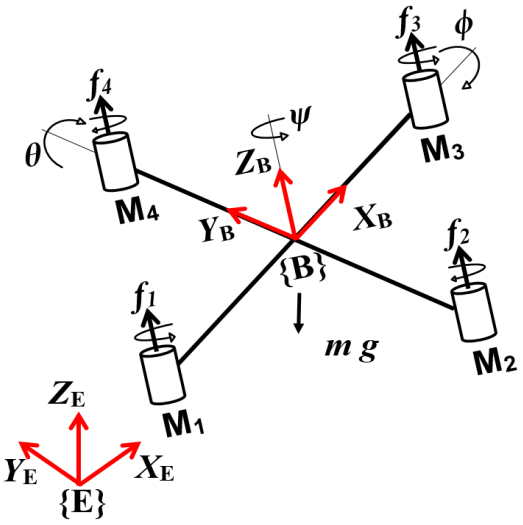

FIGURE 2.1: Coordinate system of a quadcopter.

a rotational matrix as follows:

$$
\begin{aligned}
R &= R_z(\psi)R_x(\phi)R_y(\theta) \\
&= \begin{bmatrix} c\psi & -s\psi & 0 \\ s\psi & c\psi & 0 \\ 0 & 0 & 1 \end{bmatrix} \begin{bmatrix} 1 & 0 & 0 \\ 0 & c\phi & -s\phi \\ 0 & s\phi & c\phi \end{bmatrix} \begin{bmatrix} c\theta & 0 & s\theta \\ 0 & 1 & 0 \\ -s\theta & 0 & c\theta \end{bmatrix} \\
&= \begin{bmatrix} -s\phi s\theta s\psi + c\theta c\psi & -c\phi s\psi & s\phi c\theta s\psi + s\theta c\psi \\ s\phi s\theta c\psi + c\theta s\psi & c\phi c\psi & -s\phi c\theta c\psi + s\theta s\psi \\ -c\phi s\theta & s\phi & c\phi c\theta \end{bmatrix}
\end{aligned} \tag{2.1}
$$

where s and c denote sine and cosine, respectively. Let $\xi = [X^T, \Theta^T]^T$ be the pose of quadcopter in frame $\{\mathrm{E}\}$ where $X = [x, y, z]^T \in \Re^3$ and $\Theta = [\phi, \theta, \psi]^T \in \Re^3$ represent a coordinate position and attitude, respectively. The linear velocity of the quadcopter in frame $\{\mathrm{E}\}$, $\dot{X}$, is obtained by differentiating the vector position X. Since it is measured in frame $\{\mathrm{B}\}$ then we have the following relation

$$\dot{X} = Rv \tag{2.2}$$

where $v = [v_x, v_y, v_z]^T$ is vector of linear velocity in frame $\{\mathrm{B}\}$. Therefore, to obtain the linear velocity $\dot{X}$, we need information of Euler angles Θ. However, Θ is function of time where $\dot{\Theta} = [\dot{\phi}, \dot{\theta}, \dot{\psi}]^T$ depends on the angular velocity of quadcopter's body which is measured in frame $\{\mathrm{B}\}$.

The angular velocity is obtained from the property of rotational matrix R as an orthogonal matrix, therefore

$$
\begin{aligned}
RR^T &= I \\
R^T &= R^{-1}
\end{aligned} \tag{2.3}
$$

By taking the derivative of Eq. (2.3) we have

$$\dot{R}R^T + R\dot{R}^T = 0 \tag{2.4}$$

Taking the advantage of skew symmetric matrix $S(\cdot) \in SO(3)$ as follows [81]:

$$S(\Omega) + S(\Omega)^T = 0 \tag{2.5}$$

where $\Omega = [\Omega_x, \Omega_y, \Omega_z]^T$ is the angular velocity in frame $\{\mathrm{E}\}$, and we have

$$S(\Omega) = \dot{R}R^T \tag{2.6}$$

Solving Eq. (2.6) by considering Eqs. (2.1) and (2.3), we have

$$\begin{aligned} S(\Omega) =& \dot{R}_z {R_z}^T + R_z \dot{R}_x {R_x}^T {R_z}^T + R_z R_x \dot{R}_y {R_y}^T {R_x}^T {R_z}^T \\ \begin{bmatrix} 0 & -\Omega_z & \Omega_y \\ \Omega_z & 0 & -\Omega_x \\ -\Omega_y & \Omega_x & 0 \end{bmatrix} =& \dot{\psi} \begin{bmatrix} 0 & -1 & 0 \\ 1 & 0 & 0 \\ 0 & 0 & 0 \end{bmatrix} + \dot{\phi} \begin{bmatrix} 0 & 0 & s\psi \\ 0 & 0 & -c\psi \\ -s\psi & c\psi & 0 \end{bmatrix} \\ &+ \dot{\theta} \begin{bmatrix} 0 & -s\phi & c\phi c\psi \\ s\phi & 0 & c\phi s\psi \\ -c\phi c\psi & -c\phi s\psi & 0 \end{bmatrix} \end{aligned} \tag{2.7}$$

By equating the left and right side of Eq. (2.7), we have

$$\Omega = \begin{bmatrix} c\psi & -c\phi s\psi & 0 \\ s\psi & c\phi c\psi & 0 \\ 0 & s\phi & 1 \end{bmatrix} \begin{bmatrix} \dot{\phi} \\ \dot{\theta} \\ \dot{\psi} \end{bmatrix} \tag{2.8}$$

However, the angular velocity of a quadcopter is measured in frame $\{\mathrm{B}\}$ by using a sensor attached on its body. By utilizing rotational matrix R, we can obtain the angular velocity in frame $\{\mathrm{B}\}$, $\omega = [\omega_x, \omega_y, \omega_z]^T$, as follows:

$$\begin{aligned} \omega =& R^T \Omega = \begin{bmatrix} c\theta & 0 & -c\phi s\theta \\ 0 & 1 & s\phi \\ s\theta & 0 & c\phi c\theta \end{bmatrix} \begin{bmatrix} \dot{\phi} \\ \dot{\theta} \\ \dot{\psi} \end{bmatrix} \\ \omega =& T\dot{\Theta} \end{aligned} \tag{2.9}$$

2.1.2 Dynamics Modeling

The motions of a quadcopter in all 6-DOF are performed by controlling the inputs producing from combination of its four rotors as shown in Fig. 2.1. The quadcopter has only four independent inputs consist of $u_1 = \sum_{i=1}^{4} f_i$ is the total thrust produced by the four rotors, $u_2 = L(f_4 - f_2)$ is the torque difference between the right and left rotors, $u_3 = L(f_1 - f_3)$ is the torque difference between the rear and front rotors, and $u_4 = d(f_4 + f_2 - f_1 - f_3)$ is the torque difference between clockwise rotors (M4 and M2) and counter-clockwise rotors (M1 and M3). L is the distance of each rotor from the center of gravity, and d is a scaling coefficient from force to moment. Since the quadcopter has only four independent inputs with 6-DOF, then it is categorized as an underactuated system.

The dynamics of a quadcopter is derived by employing the Newton's second law for translational and rotational motions [13, 18, 22, 27, 42, 82]. Employing the Newton's second law for a translational motion of a rigid body in frame $\{\mathrm{E}\}$, we have

$$\begin{aligned}
\ddot{X} =& \frac{1}{m}\sum F_{ext} \\
=& R\begin{bmatrix} 0 \\ 0 \\ \frac{u_1}{m} \end{bmatrix} + \begin{bmatrix} 0 \\ 0 \\ -g \end{bmatrix} \\
\begin{bmatrix} \ddot{x} \\ \ddot{y} \\ \ddot{z} \end{bmatrix} =& \begin{bmatrix} (s\phi c\theta s\psi + s\theta c\psi)\frac{u_1}{m} \\ (-s\phi c\theta c\psi + s\theta s\psi)\frac{u_1}{m} \\ c\phi c\theta \frac{u_1}{m} \end{bmatrix} + \begin{bmatrix} 0 \\ 0 \\ -g \end{bmatrix}
\end{aligned} \tag{2.10}$$

where $\ddot{X} = [\ddot{x}, \ddot{y}, \ddot{z}]^T$ is the translational acceleration vector in frame $\{\mathrm{E}\}$, $\sum F_{ext}$ is the total force applied on the body of quadcopter with respect to frame $\{\mathrm{E}\}$, m is the total mass of quadcopter, and g is the gravitational acceleration.

Furthermore, in a rotational motion, we have the inertia matrix as follows:

$$I = \begin{bmatrix} I_{xx} & -I_{xy} & -I_{xz} \\ -I_{yx} & I_{yy} & -I_{yz} \\ -I_{zx} & -I_{zy} & I_{zz} \end{bmatrix} \tag{2.11}$$

where I_{xx}, I_{yy}, and I_{zz} are called moments of inertia with respect to x, y, and z axis, respectively. I_{xy}, I_{xz}, I_{yx}, I_{yz}, I_{zx}, and I_{zy}, are called products of inertia, respectively. Assuming the quadcopter is a rigid body with constant mass and its axis is aligned with principal axis of inertia, then the product of inertia $I_{xy} = I_{xz} = I_{yx} = I_{yz} = I_{zx} = I_{zy} = 0$, and the inertia matrix in Eq. (2.11)

becomes a diagonal matrix as follows:

$$I = \begin{bmatrix} I_{xx} & 0 & 0 \\ 0 & I_{yy} & 0 \\ 0 & 0 & I_{zz} \end{bmatrix} \tag{2.12}$$

Exploiting now the Newton's second law on a rotational motion, we have the equation of moment for a quadcopter in body frame $\{\mathrm{B}\}$ as follows:

$$I\dot{\omega} = -\omega \times I\omega + \sum T_{ext} \tag{2.13}$$

where $\dot{\omega} = [\dot{\omega}_x, \dot{\omega}_y, \dot{\omega}_z]^T$ is the rotational acceleration vector in frame $\{\mathrm{B}\}$ and $\sum T_{ext} = [u_2, u_3, u_4]^T$ is the total torque acts on the body of quadcopter with respect to frame $\{\mathrm{B}\}$. Substituting Eq. (2.9) together with its time-derivative into Eq. (2.13), we have

$$I(\dot{T}\dot{\Theta} + T\ddot{\Theta}) = -T\dot{\Theta} \times IT\dot{\Theta} + \sum T_{ext} \tag{2.14}$$

where $\dot{T}$ is the time-derivative of transformation matrix T in Eq. (2.9) and $\ddot{\Theta} = [\ddot{\phi}, \ddot{\theta}, \ddot{\psi}]^T$ is the angular acceleration vector in frame $\{\mathrm{E}\}$. Solving Eq. (2.14) we have

$$\begin{bmatrix} \ddot{\phi} \\ \ddot{\theta} \\ \ddot{\psi} \end{bmatrix} = J^{-1} \begin{bmatrix} K_1(\Theta, \dot{\Theta}) \\ K_2(\Theta, \dot{\Theta}) \\ K_3(\Theta, \dot{\Theta}) \end{bmatrix} + J^{-1} \begin{bmatrix} u_2 \\ u_3 \\ u_4 \end{bmatrix} \tag{2.15}$$

where

$$J = \begin{bmatrix} I_{xx}c\theta & 0 & -I_{xx}c\phi s\theta \\ 0 & I_{yy} & I_{yy}s\phi \\ I_{zz}s\theta & 0 & I_{zz}c\phi c\theta \end{bmatrix},$$

$$\begin{aligned} K_1(\Theta, \dot{\Theta}) &= (I_{xx} + I_{yy} - I_{zz})\dot{\phi}\dot{\theta}s\theta + (-I_{xx} + I_{yy} - I_{zz})\dot{\phi}\dot{\psi}s\phi s\theta \\ &\quad + (I_{xx} + I_{yy} - I_{zz})\dot{\theta}\dot{\psi}c\phi c\theta + (I_{yy} - I_{zz})\dot{\psi}^2 s\phi c\phi c\theta, \\ K_2(\Theta, \dot{\Theta}) &= (-I_{yy} + (I_{zz} - I_{xx})c(2\theta))\dot{\phi}\dot{\psi}c\phi \\ &\quad + (I_{zz} - I_{xx})(\dot{\phi}^2 - \dot{\psi}^2 c^2\phi)s\theta c\theta, \\ K_3(\Theta, \dot{\Theta}) &= (-I_{zz} + I_{xx} - I_{yy})\dot{\phi}\dot{\theta}c\theta + (I_{zz} + I_{xx} - I_{yy})\dot{\phi}\dot{\psi}s\phi c\theta \\ &\quad + (I_{zz} - I_{xx} + I_{yy})\dot{\theta}\dot{\psi}c\phi s\theta - (I_{xx} - I_{yy})\dot{\psi}^2 s\phi c\phi s\theta. \end{aligned}$$

Combining Eqs. (2.10) and (2.15), we have complete dynamics model of a quadcopter as follows:

$$\ddot{\xi} = f_1(\Theta, \dot{\Theta}) + f_2(\Theta, u) \tag{2.16}$$

where

$$
\begin{aligned}
\ddot{\xi} &= [\ddot{x}, \ddot{y}, \ddot{z}, \ddot{\phi}, \ddot{\theta}, \ddot{\psi}]^T, \\
f_1(\Theta, \dot{\Theta}) &= J_m^{-1}[0, 0, -mg, K_1(\Theta, \dot{\Theta}), K_2(\Theta, \dot{\Theta}), K_3(\Theta, \dot{\Theta})]^T, \\
f_2(\Theta, u) &= J_m^{-1} \begin{bmatrix} (s\phi c\theta s\psi + s\theta c\psi)u_1 \\ (-s\phi c\theta c\psi + s\theta s\psi)u_1 \\ c\phi c\theta u_1 \\ u_2 \\ u_3 \\ u_4 \end{bmatrix}, \\
J_m &= \begin{bmatrix} mI_{3\times3} & 0_{3\times3} \\ 0_{3\times3} & J \end{bmatrix},
\end{aligned}
$$

$I_{3\times3}$ and $0_{3\times3}$ are a 3×3 identity matrix and a 3×3 null matrix, respectively. The dynamics of quadcopter in Eq. (2.16) is obtained by neglecting the aerodynamics effects and gyroscopic terms. These terms will be considered as disturbances in the controller design.

2.2 Experimental Setup

In this works, we design an experimental testbed of a quadcopter as shown in Fig. 2.2. In this testbed, the quadcopter is attached to the rigid links for conducting the same experiments multiple times to verify the effectiveness and repeatability of the control strategy. This rigid links also function as safety link to prevent the quadcopter crashing caused by unstable flight. The flight controller is developed in a personal computer (PC) and connected to the quadcopter through analog to digital and digital to analog-converter (AD/DA). AD-converter is utilized for capturing the states information from the sensors while DA-converter is for sending the control signal generated in PC into the actuators. In oder to verify the robustness of the control design, the disturbance generated by three different electric fan (power: 57 W, 49 W, and 37 W) is applied in distance about 0.5-1.5 m and located in different location from the quadcopter. Magnitude of the disturbance is proportional to the distance between the quadcopter and the fan, and can be chosen by turn on all fan or one of them.

In this experimental testbed, we only measure the position states by using potentiometers those are attached on each link as shown Fig. 2.3. Because the quadcopter is a second-order system as presented in Eq. (2.16), we need information of position (absolute position and attitude) and velocity (linear and angular) states for the controller design. Furthermore, an observer is developed to estimate the velocity states. In this chapter, we only discuss the derivation process

to obtain position and attitude states of the quadcopter testbed from the sensors. The design of observer to estimate the velocity is described in the next chapter.

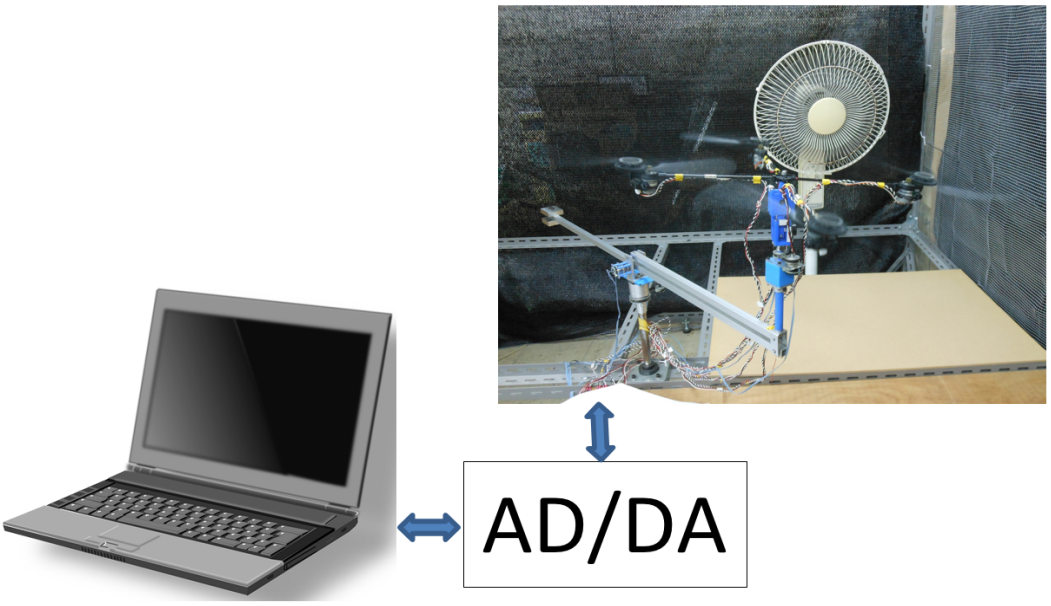

FIGURE 2.2: Experimental quadcopter testbed

2.2.1 Sensor Configuration and Coordinate Frame

States variable for controller are measured by potentiometers (S_1-S_5) those are located on each link as shown Fig. 2.3. These potentiometers are used to measure all positions of the rotational motion on each link ($\theta_1 - \theta_5$). A coordinate frame transformation is utilized to obtain position of the quadcopter with respect to frame $\{E\}$. We assign a coordinate frame on each link as shown in Fig. 2.4. Frame $\{B\}$ is assigned as body frame, frames $\{0\text{-}5\}$ are assigned on each rotational link, frame$\{E\}$ is an inertial frame, and the corresponding rotational angles are as shown in Fig. 2.4. Motion of link L_2 depends on link L_1 and therefore rotational angle $\theta_2' = \theta_2$. The transformation matrices for each frame are given as follows:

$$
\begin{aligned}
{}^{E}_{0}T &= \begin{bmatrix} c\theta_1 & -s\theta_1 & 0 & 0 \\ s\theta_1 & c\theta_1 & 0 & 0 \\ 0 & 0 & 1 & 0 \\ 0 & 0 & 0 & 1 \end{bmatrix} & {}^{0}_{1}T &= \begin{bmatrix} 0 & 0 & 1 & 0 \\ c\theta_2 & -s\theta_2 & 0 & 0 \\ s\theta_2 & c\theta_2 & 0 & 0 \\ 0 & 0 & 0 & 1 \end{bmatrix} \\
{}^{1}_{2}T &= \begin{bmatrix} -c\theta_2' & s\theta_2' & 0 & L_1 \\ s\theta_2' & c\theta_2' & 0 & 0 \\ 0 & 0 & -1 & 0 \\ 0 & 0 & 0 & 1 \end{bmatrix} & {}^{2}_{3}T &= \begin{bmatrix} -c\theta_3 & s\theta_3 & 0 & 0 \\ 0 & 0 & 1 & L_2 \\ s\theta_3 & c\theta_3 & 0 & 0 \\ 0 & 0 & 0 & 1 \end{bmatrix} \\
{}^{3}_{4}T &= \begin{bmatrix} s\theta_4 & c\theta_4 & 0 & 0 \\ 0 & 0 & 1 & 0 \\ c\theta_4 & -s\theta_4 & 0 & L_3 \\ 0 & 0 & 0 & 1 \end{bmatrix} & {}^{4}_{5}T &= \begin{bmatrix} c\theta_5 & -s\theta_5 & 0 & L_4 \\ 0 & 0 & 1 & 0 \\ -s\theta_5 & -c\theta_5 & 0 & 0 \\ 0 & 0 & 0 & 1 \end{bmatrix} \\
{}^{5}_{B}T &= \begin{bmatrix} 0 & 0 & 1 & L_5 \\ 1 & 0 & 0 & 0 \\ 0 & 1 & 0 & 0 \\ 0 & 0 & 0 & 1 \end{bmatrix}
\end{aligned}
\tag{2.17}
$$

The transformation matrix from body coordinate frame {B} into inertial frame {E} is obtained as:

$$
\begin{aligned}
{}^{E}_{B}T &= {}^{E}_{0}T\,{}^{0}_{1}T\,{}^{1}_{2}T\,{}^{2}_{3}T\,{}^{3}_{4}T\,{}^{4}_{5}T\,{}^{5}_{B}T \\
&= \begin{bmatrix} & {}^{E}_{B}R & & {}^{E}_{B}P \\ 0 & 0 & 0 & 1 \end{bmatrix} \\
{}^{E}_{B}R &= \begin{bmatrix} c\theta_5 c\theta_{1+3} + s\theta_4 s\theta_5 s\theta_{1+3} & -c\theta_4 s\theta_{1+3} & s\theta_5 c\theta_{1+3} - c\theta_5 s\theta_4 s\theta_{1+3} \\ c\theta_5 s\theta_{1+3} - s\theta_4 s\theta_5 c\theta_{1+3} & c\theta_4 c\theta_{1+3} & s\theta_5 s\theta_{1+3} + c\theta_5 s\theta_4 c\theta_{1+3} \\ -c\theta_4 s\theta_5 & -s\theta_4 & c\theta_4 c\theta_5 \end{bmatrix} \\
{}^{E}_{B}P &= \begin{bmatrix} L_5(s\theta_5 c\theta_{1+3} - c\theta_5 s\theta_4 s\theta_{1+3}) - L_1 c\theta_2 s\theta_1 - L_4 s\theta_4 s\theta_{1+3} \\ L_5(s\theta_5 s\theta_{1+3} + c\theta_5 s\theta_4 c\theta_{1+3}) + L_1 c\theta_1 c\theta_2 + L_4 s\theta_4 c\theta_{1+3} \\ L_2 + L_3 + L_1 s\theta_2 + L_4 c\theta_4 + L_5 c\theta_4 c\theta_5 \end{bmatrix}
\end{aligned}
\tag{2.18}
$$

where $\theta_{1+3} = \theta_1 + \theta_3$.

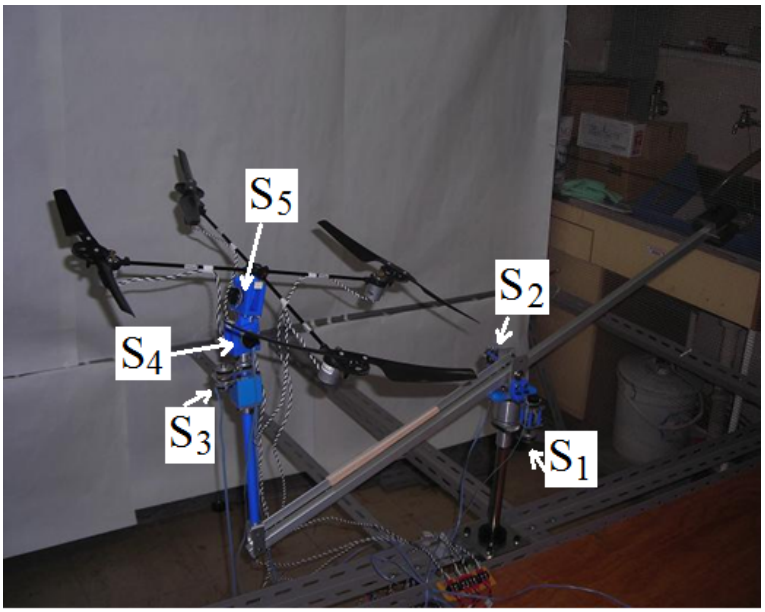

(a)

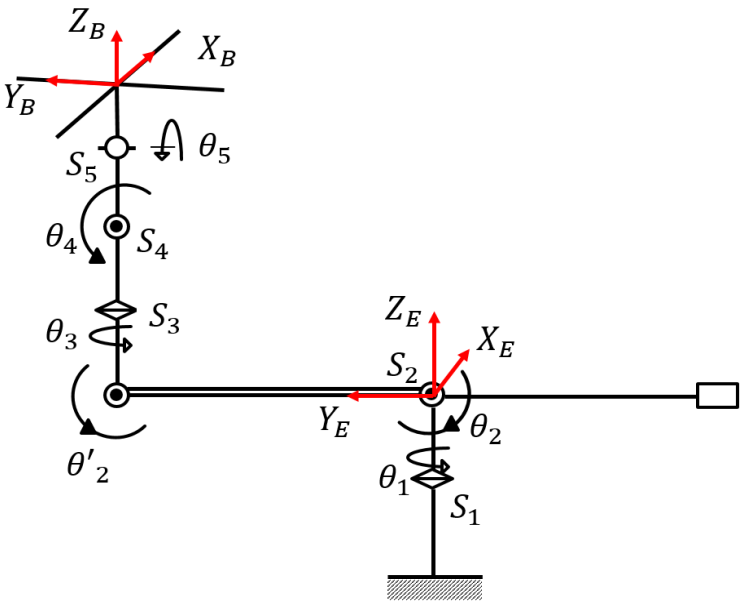

(b)

FIGURE 2.3: Sensors placement on the experimental quadcopter testbed: (a) actual configuration, (b) schematic

From Eq. (2.18) and considering Eq. (2.1), position and attitude of the quadcopter with respect to frame {E} are defined as follows:

$$
\begin{aligned}
X &= [x, y, z]^T = {}^E_B P, \\
\phi &= -\theta_4, \\
\theta &= \theta_5, \\
\psi &= \theta_1 + \theta_3.
\end{aligned}
\tag{2.19}
$$

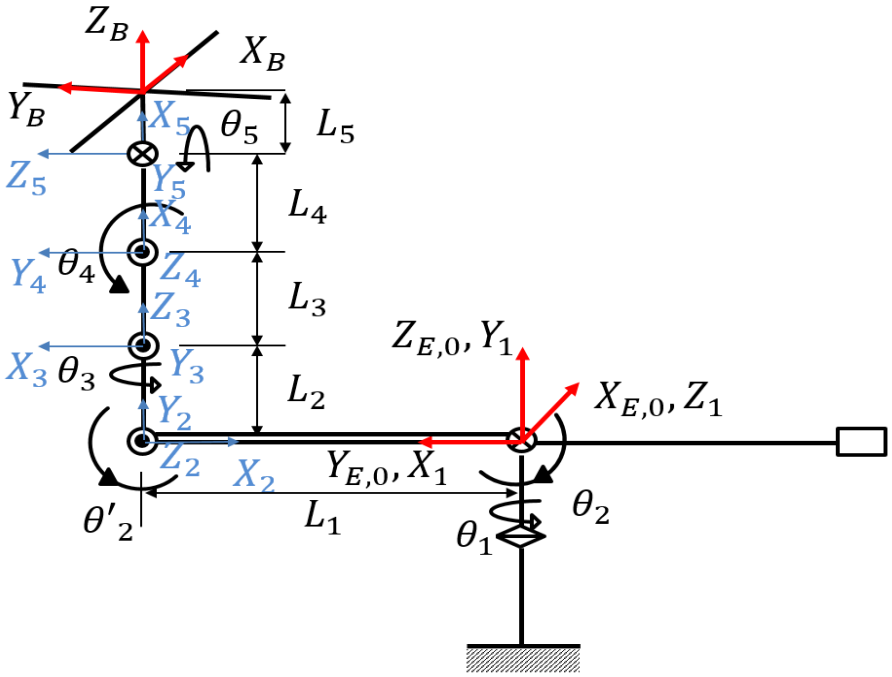

FIGURE 2.4: Frame transformation on the experimental quadcopter testbed

2.2.2 Actuator Dynamics

2.2.2.1 Thrust Force

The thrust force of the experimental quadcopter testbed is generated by four motors as actuators with gears and blades. Since it is difficult to obtain an analytical model of the thrust force generator, we develop an empirical formula to describe a relationship between voltage and resulting thrust for each actuator experimentally by applying different voltages and measuring the resulting thrust. The voltage versus thrust data follow a smooth curve as shown in Fig. 2.5, and the thrust model is obtained by using the least-squares approximation of a second-order polynomial function as follows:

$$f_j = 0.0321V_j^2 + 0.0579V_j - 0.0462 \tag{2.20}$$

where V_j (volt) is the voltage applied to the j-th motor ($j = 1, \ldots, 4$). Assuming that all actuators are identical, we apply Eq. (2.20) to estimate each thrust force f_j (N).

2.2.2.2 Electric Power Consumption

It is essential to evaluate the power consumed by each actuator during the flight to know how much energy is required to complete a mission. Each actuator of the experimental quadcopter testbed which is utilized in this study is driven by a DC motor. If we regard the DC motor as a

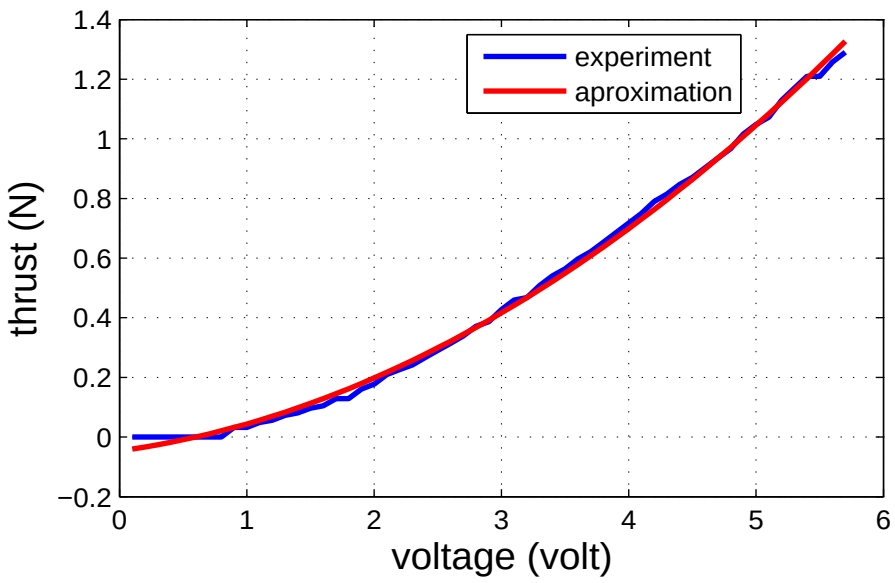

FIGURE 2.5: Applied voltages versus thrust force of a rotor.

resistance load, the power consumed by each DC motor can be evaluated by

$$P_j = \frac{V_j^2}{R_j} \tag{2.21}$$

where P_j and R_j are the power and resistance of the j-th motor, respectively. By applying V_j and the measurement of P_j to Eq. (2.21), the value of R_j can be estimated. In this study, the value of R_j is estimated by conducting several experiments and measuring P_j for one motor. The average resistance of the motor is obtained as $R_j = 2.975$ ohm.

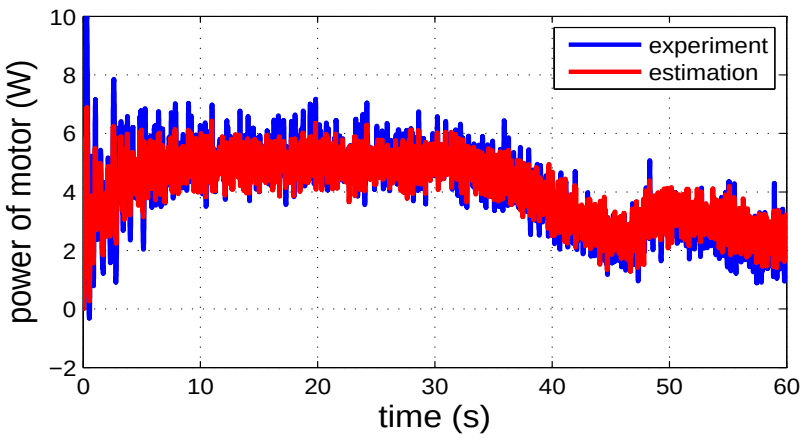

FIGURE 2.6: Electric power of a motor during the hovering motion.

To validate the value of the estimated resistance R_j, we perform an experiment on the quadcopter testbed in hovering mode and measure the power consumed by the motor. A comparative result with the estimation one using Eq. (2.21) is given in Fig. 2.6. It is seen that the measured power

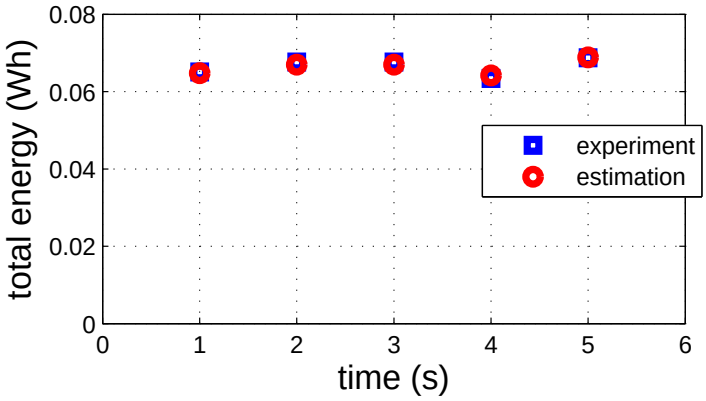

FIGURE 2.7: Total energy consumed by a motor during the hovering motion.

is similar to the estimated one and therefore the resistance R_j above can be used to estimate the power consumption for each motor of the quadcopter testbed. In addition, by integrating the power consumption during the flight, we obtain the total energy consumed by the motor. By conducting several experiments in hovering mode, the total energy consumed by the motor is obtained as shown in Fig. 2.7. Since all motors are assumed to be identical, the same resistance R_j is employed to estimate the power and total energy consumption during the control of the quadcopter.

2.2.3 Experimental Testbed Parameters

The experimental components of the quadcopter testbed which is utilized in this study are given in Table 2.1. The parameters of the experimental quadcopter testbed and its value are shown in Table 2.2.

TABLE 2.1: Components of experimental testbed.

Components	Type	Manufacturer
4 rotor helicopter	DRAGANFLYER IV	RCTOYS
AD converter board	ADA16-8/2(CB)L	Contec
DA converter board	DAI16-4(USB)	Contec
Potentiometer	JC22E 1k	Copal Electronics
DC motor	RC-280SA-2485	Mabuchi Motor Co., Ltd.
Motor driver	ADS 50-5	Maxon Motor
Power supply	PUP5-2	Takasago
Power supply	HWS100-12/A	Densei-λ
PC(OS)	Centrino Dual-Core (Windows-7 32 bit)	Panasonic(Microsoft)

TABLE 2.2: Parameters of quadcopter experimental testbed.

Symbol	Parameters	Value (unit)
m	mass of quadcopter testbed	0.285 (kg)
L	distance of rotor to the quadcopter center of gravity	0.212 (m)
g	gravitational acceleration	9.807 (m/s^2)
d	force to moment scaling factor	1 (m)
I_x	moment of inertia about x axis in body frame	5.136×10^{-3} (kg.m^2)
I_y	moment of inertia about y axis in body frame	5.136×10^{-3} (kg.m^2)
I_z	moment of inertia about z axis in body frame	1.016×10^{-2} (kg.m^2)

Chapter 3

Closed-Loop Controller Configuration and Velocity States Estimation

3.1 Introduction

The dynamics of quadcopter derived in the previous chapter shows that the quadcopter has four independent inputs with 6-DOF. Therefore, a quadcopter is categorized as an underactuated system, and it is relatively difficult to design the control strategy to control all motions independently through its original inputs. For simplicity, we transform the original dynamics of the quadcopter into a simple decoupled form by introducing the synthetic input. Furthermore, a general closed-loop controller configuration is designed. Therefore, any control strategy can be applied simply to the synthetic input. In order to calculate the original inputs, we employ a method presented in [43, 83]. A least-squares algorithm is utilized to solve the overdetermined problem of the quadcopter dynamics in the translational motion. In addition, the rotational inputs are solved by a simple dynamics inversion.

The previous chapter describes that the experimental quadcopter testbed only provides absolute position and attitude states of the quadcopter those are measured from the sensors. In this chapter, the velocity states are estimated for the controller by applying a reduced-order observer strategy presented in [84]. The effectiveness of this closed-loop configuration and reduced-order observer design are experimentally evaluated by applying a simple PID controller for the synthetic input.

3.2 Dynamics Decoupling

In order to simplify the controller design of a quadcopter, which is categorized as an underactuated system, we transform the original underactuated dynamics of the quadcopter described in Eq. (2.16) into a decoupled form. Recalling the original dynamics of a quadcopter as follows:

$$\ddot{\xi} = f_1(\Theta, \dot{\Theta}) + f_2(\Theta, u) \tag{3.1}$$

By considering the synthetic input $v = f_1(\Theta, \dot{\Theta}) + f_2(\Theta, u)$, the decoupled form of Eq. (3.1) is written in a simple linear form as follows:

$$\begin{aligned} \dot{\xi}_1 &= \xi_2 \\ \dot{\xi}_2 &= v \end{aligned} \tag{3.2}$$

where $\xi_1 = \xi = [x, y, z, \phi, \theta, \psi]^T$ and $\xi_2 = \dot{\xi}$. By considering $v = [v_x, v_y, v_z, v_\phi, v_\theta, v_\psi]^T$ as a new input vector in controller design then we have a such as fully-actuated system. Furthermore, general controller strategy can be applied to design this new control input v, simply.

3.3 Closed-Loop Configuration

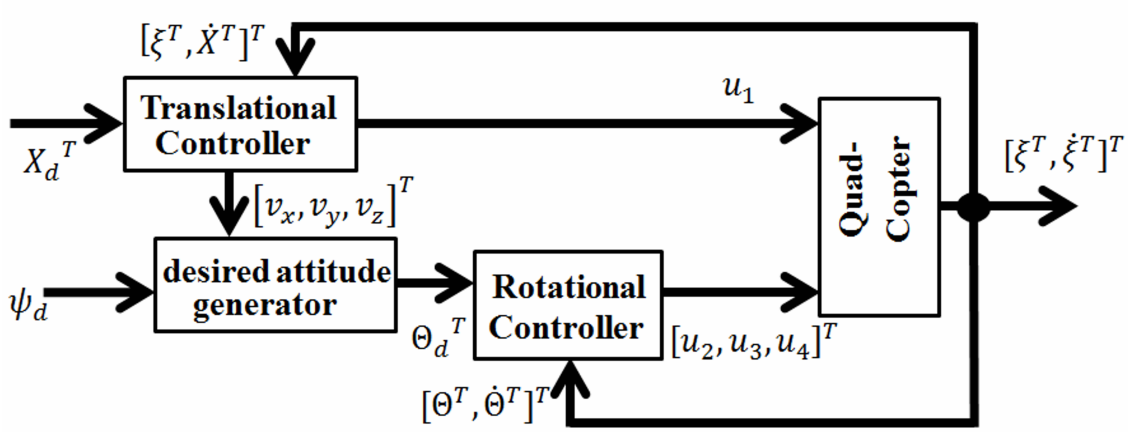

FIGURE 3.1: Closed-loop controller configuration for a quadcopter.

In order to make the quadcopter fly autonomously, we choose the desired output as the absolute position $X_d = [x_d, y_d, z_d]^T$ and yaw angle ψ_d of the quadcopter. In this work, we adopt the control structure presented in [18] by adding the least-squares method to solve the overdetermined problem in translational motion of the quadcopter as shown in Fig. 3.1. In this configuration, we divide the control structure into two parts mainly. The first one is a translational controller with a desired attitude generator. The translational controller is for absolute position tracking control. This part generates synthetic inputs v_x, v_y, and v_z. By using the least-squares method

in [43, 83], the original input u_1 is calculated. The second part is a rotational controller that handles the attitude tracking control. This part generates synthetic inputs v_ϕ, v_θ, and v_ψ, and converts into original inputs u_2, u_3, and u_4 by considering rotational dynamics of Eq. (2.16). Derivation of these control inputs is given in Subsection 3.3.1.

In the desired attitude generator block, the desired attitude of the quadcopter, roll angle (ϕ_d) and pitch angle (θ_d), are generated , while ψ_d is remained as assigned. (ϕ_d) and (θ_d) are calculated from the translational motion dynamics of Eq. (2.16) by considering the synthetic inputs in Eq. (3.2) as follows. Equating the synthetic inputs for the translational motion in Eq. (3.2) with those in Eq. (2.16), we have

$$\begin{aligned} v_x =& (s\theta c\psi + s\phi c\theta s\psi)\frac{u_1}{m} \\ v_y =& (s\theta s\psi - s\phi c\theta c\psi)\frac{u_1}{m} \\ v_z =& c\phi c\theta \frac{u_1}{m} - g \end{aligned} \tag{3.3}$$

Solving Eq. (3.3) with respect to the attitude variables and replacing them with the desired attitude of the quadcopter, we have

$$\begin{aligned} \phi_d =& \arctan\left(\frac{v_x \sin\psi_d - v_y \cos\psi_d}{v_z + g}\right) \\ \theta_d =& \arctan\left(\frac{v_x \cos\psi_d + v_y \sin\psi_d}{\sqrt{(v_x \sin\psi_d - v_y \cos\psi_d)^2 + (v_z+g)^2}}\right) \end{aligned} \tag{3.4}$$

3.3.1 Control Input Calculation

3.3.1.1 Translational Motion

Rewriting the translational motion of the quadcopter in Eq. (3.3) in a matrix form, we have

$$\begin{bmatrix} (s\phi c\theta s\psi + s\theta c\psi) \\ (s\theta s\psi - s\phi c\theta c\psi) \\ c\phi c\theta \end{bmatrix} u_1 = \begin{bmatrix} v_x \\ v_y \\ v_z + g \end{bmatrix} m \tag{3.5}$$

Equation (3.5) shows that we have an overdetermined problem because there are three equations to solve one unknown variable, u_1. To solve this problem, the least-squares algorithm is utilized. We represent Eq. (3.5) in the following form:

$$ABu_1 = C \tag{3.6}$$

where $A = \begin{bmatrix} c\psi & s\psi & 0 \\ s\psi & -c\psi & 0 \\ 0 & 0 & 1 \end{bmatrix}$; $B = \begin{bmatrix} s\theta \\ s\phi c\theta \\ c\phi c\theta \end{bmatrix}$; and $C = \begin{bmatrix} v_x \\ v_y \\ v_z + g \end{bmatrix} m$.

Applying the least-squares algorithm, we have

$$Bu_1 = A^T C \tag{3.7}$$

because of $A^T A = AA^T = I_{3\times 3}$, where $I_{3\times 3}$ is an 3×3 identity matrix. Squaring both side of Eq. (3.7), we have

$$B^T B u_1^2 = (A^T C)^T A^T C \tag{3.8}$$

From Eq. (3.8), because $B^T B = 1$ then we have

$$u_1 = m\sqrt{v_x^2 + v_y^2 + (v_z + g)^2} \tag{3.9}$$

3.3.1.2 Rotational Motion

Inputs for rotational motion, u_2, u_3, and u_4, are straightforward generated by equating the rotational dynamics in Eq. (2.15) and those in Eq. (3.1), and hence we have

$$\begin{bmatrix} u_2 \\ u_3 \\ u_4 \end{bmatrix} = J \begin{bmatrix} v_\phi \\ v_\theta \\ v_\psi \end{bmatrix} - \begin{bmatrix} K_1(\Theta, \dot{\Theta}) \\ K_2(\Theta, \dot{\Theta}) \\ K_3(\Theta, \dot{\Theta}) \end{bmatrix} \tag{3.10}$$

3.4 Design of Reduced-Order Observer

The quadcopter is a second-order system which has position and velocity states as in Eq. (3.1). In this work, the quadcopter testbed only provides position states (absolute position and attitude) at each sampling time those are measured from the sensors. The velocity states are estimated by using the reduced-order observer in [84] (see Appendix). We utilize this method because this observer estimates the velocity states from a continuous-time dynamics model by considering a discrete-time control system. Therefore, it is practically applicable for our experimental testbed.

By considering Eqs. (3.1) and (A.1), we have $f_1(\xi_1) = 0$, $g_1(\xi_1) = 1$, $f_2(\xi_1, \xi_2, u) = f_1(\Theta, \dot{\Theta}) + f_2(\Theta, u)$. Because the input vector $u = [u_1, u_2, u_3, u_4]^T$ does not satisfy assumption **A1**, we consider new inputs v_x, v_y, and v_z, and the control input $u = [v_x, v_y, v_z, u_2, u_3, u_4]^T$. Applying these new inputs to dynamics in Eq. (3.1), we meet all the assumptions in Appendix that are required to design the observer. Hence, the reduced-order observer can be designed as follows:

$$\hat{\xi}_2(k) = (I - TH)\hat{\xi}_2(k-1) + TN_T \tag{3.11}$$

where T is a sampling period, I is a 6×6 identity matrix, H is a 6×6 diagonal matrix which is explained in Appendix, and

$$\begin{aligned} N_T &= H\Psi_T + f_2(y_1(k-1), \Psi_T, u(k-1)), \\ \Psi_T &= \frac{y_1(k) - y_1(k-1)}{T}. \end{aligned} \tag{3.12}$$

Furthermore, to apply this reduced-order observer to the quadcopter testbed, the closed-loop controller configuration in Fig. 3.1 is modified into a new one given in Fig. 3.2.

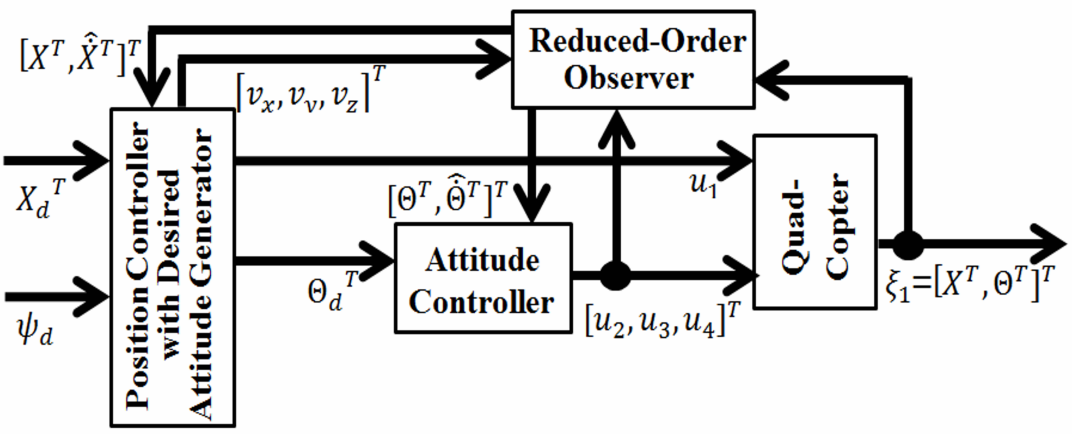

FIGURE 3.2: Closed-loop controller configuration with observer for the experimental quadcopter testbed.

3.5 Experiment

3.5.1 PID Controller Design

In order to check the effectiveness of the closed-loop controller configuration and the velocity observer, we conduct the experiment by designing a simple proportional-integral-differential (PID) controller for the synthetics input v.

Considering the dynamics of the quadcopter in Eq. (3.2) and the output captured from the sensor as follows:

$$y_1(k) = \xi_1(k) \tag{3.13}$$

We assume that the control input v in Eq. (3.2) is realized through a zero order-hold with sampling time $T = 5$ ms, and only the position and attitude $\xi_1(k)$ at each sampling period

(*i.e.*, $y_1(k) = \xi_1(kT)$) is available for control. A PID controller strategy for tracking and stabilizing the system in Eq. (3.2) is designed as follows:

$$v = \dot{\xi}_{2d} + K_p e + K_d \dot{e} + K_i \int e dt \tag{3.14}$$

where $e = \xi_{1d} - \xi_1$, $\dot{e} = \xi_{2d} - \hat{\xi}_2$, and $\hat{\xi}_2$ is obtained from the reduced-order observer in Eq. (3.11). ξ_{1d} and ξ_{2d} are desired trajectories for ξ_1 and ξ_2, respectively. In order to guarantee the control system stability based on the Routh-Hurwitz criterion, we choose K_p, K_d, and K_i as positive constant and $K_p K_d > K_i$ [85]. The original input u_1, u_2, u_3, and u_4 are calculated from the synthetic input vector v using Eqs. (3.9) and (3.10).

The effectiveness of the reduced-order observer in Eq. (3.11) to estimate the velocity states is verified by comparing those with the backward-difference method. For calculating the velocity based on the backward-difference method, a second-order low-pass filter with 15 Hz cut-off frequency is applied to reduce the high frequency noise. These estimated velocity states are employed in a PID controller in Eq. (3.14). The control parameters for both methods were tuned to achieve the best experimental results and were obtained as follows (units are omitted):

PID control with a reduced-order observer:

$$\begin{aligned}
K_p &= \mathrm{diag}(30, 30, 50, 130, 100, 400), \\
K_i &= \mathrm{diag}(2, 2, 30, 30, 10, 160), \\
K_d &= \mathrm{diag}(20, 20, 20, 40, 30, 90), \\
H &= \mathrm{diag}(100, 100, 100, 50, 60, 50).
\end{aligned}$$

PID control with a backward-difference method:

$$\begin{aligned}
K_p &= \mathrm{diag}(12, 14, 50, 80, 60, 200), \\
K_i &= \mathrm{diag}(4, 4, 30, 15, 10, 20), \\
K_d &= \mathrm{diag}(10, 10, 20, 20, 15, 30).
\end{aligned}$$

Because the noise increases in the backward-difference method, controller gains are set smaller than those for the reduced-order observer.

3.5.2 Experimental Results

In this experiment, we design a desired trajectory to be tracked in the experiment consisting of four different motions within 60 s as follows: A: take-off motion (0-10 s), B: maneuver in the

$x-y$ plane at the same height (10-15 s), C: hovering by performing yaw motion (15-45 s), and D: landing motion (45-60 s) as shown in Fig. 3.3.

Figure 3.4 shows the effectiveness of the reduced-order observer to estimate the velocity states of a quadcopter for all motions from its corresponding position states. It is seen that the reduced-order observer reduces the high frequency signals effectively than the backward-difference with a low-pass filter. This observer estimates the velocity states within 25 ms from its initial value, and reduces the variance of the velocity signal from the backward-difference method about 81.08% on average. Since this observer can estimate the states in relatively fast time, it is useful from a real-time application point of view.

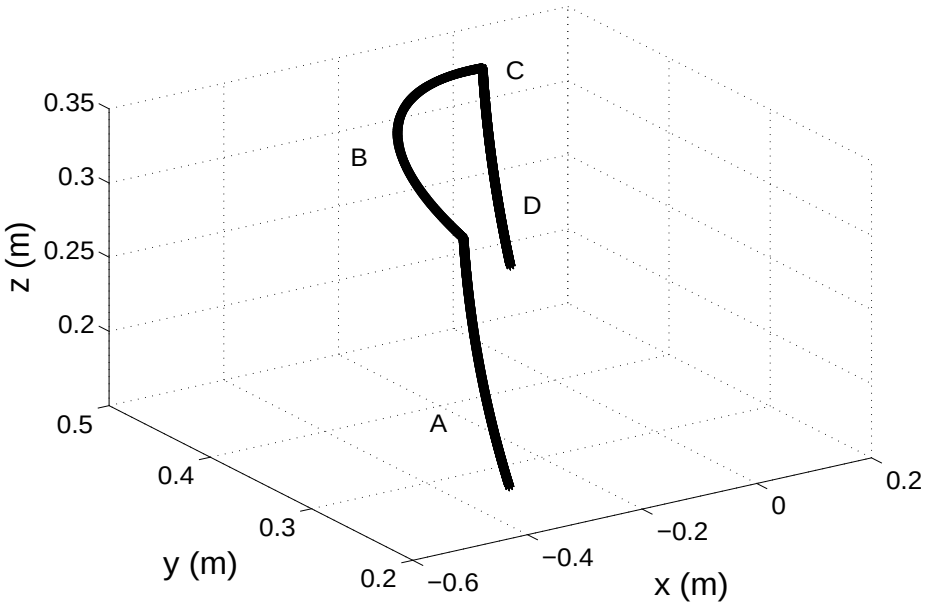

FIGURE 3.3: 3-dimensional desired trajectory.

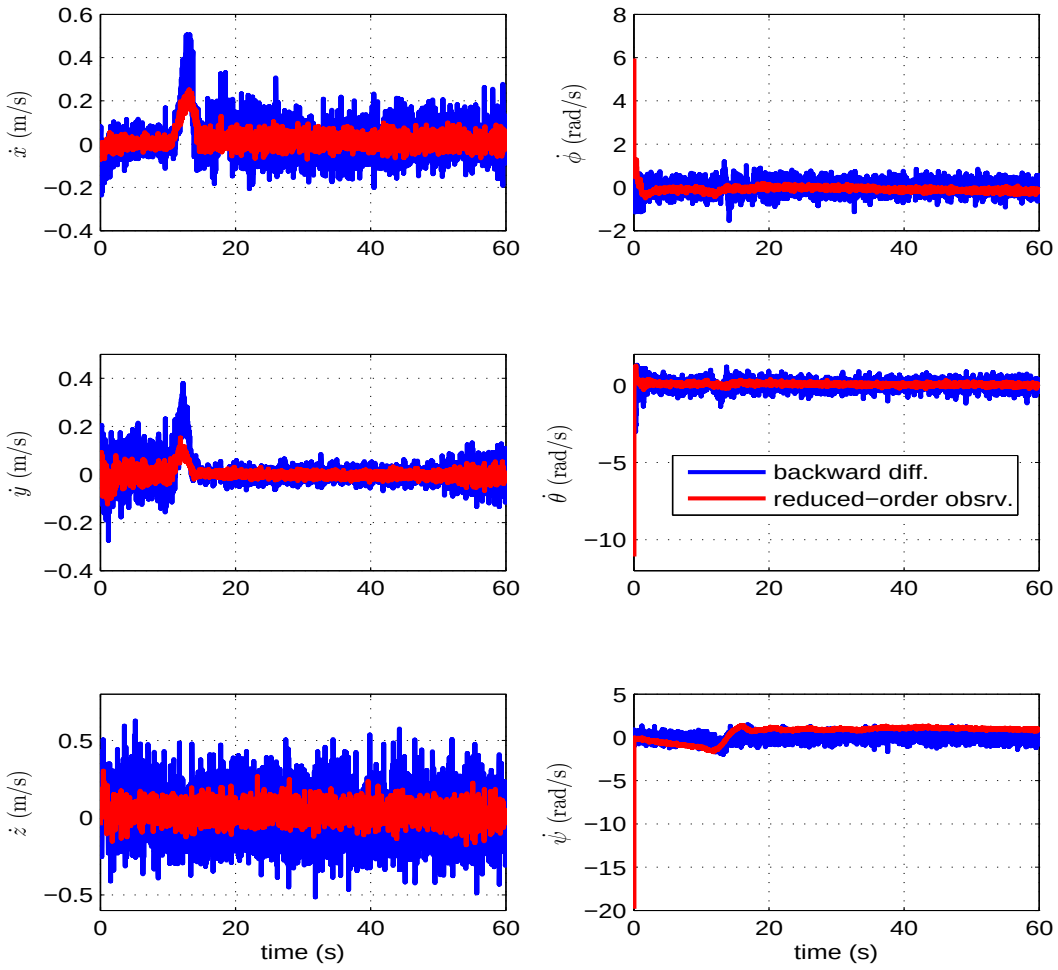

FIGURE 3.4: Velocity profiles obtained from a reduced-order observer and a backward-difference method.

In addition, the reduced-order observer allows us to choose PID controller gains relatively higher compared to those in the backward-difference method. Therefore, we can improve the tracking performance of the closed-loop control system as shown in Figs. 3.5 and 3.6. The PID controller utilizing the reduced-order observer produces smaller tracking error as shown in Fig. 3.7. To evaluate the reliability of this method, we conduct the same experiments seven times and the results are shown in Fig. 3.8. The averages of all trials are given in Table 3.1. The PID controller with a reduced-order observer produces better performance by resulting in smaller root-mean squared error (RMSE) and error variance in almost all trials. In z position, it is seen that the reduced-order observer does not improve the performance, because we set the PID gain same as the backward-difference method. The reduced-order observer reduces the RMSE by about 35.15% on average.

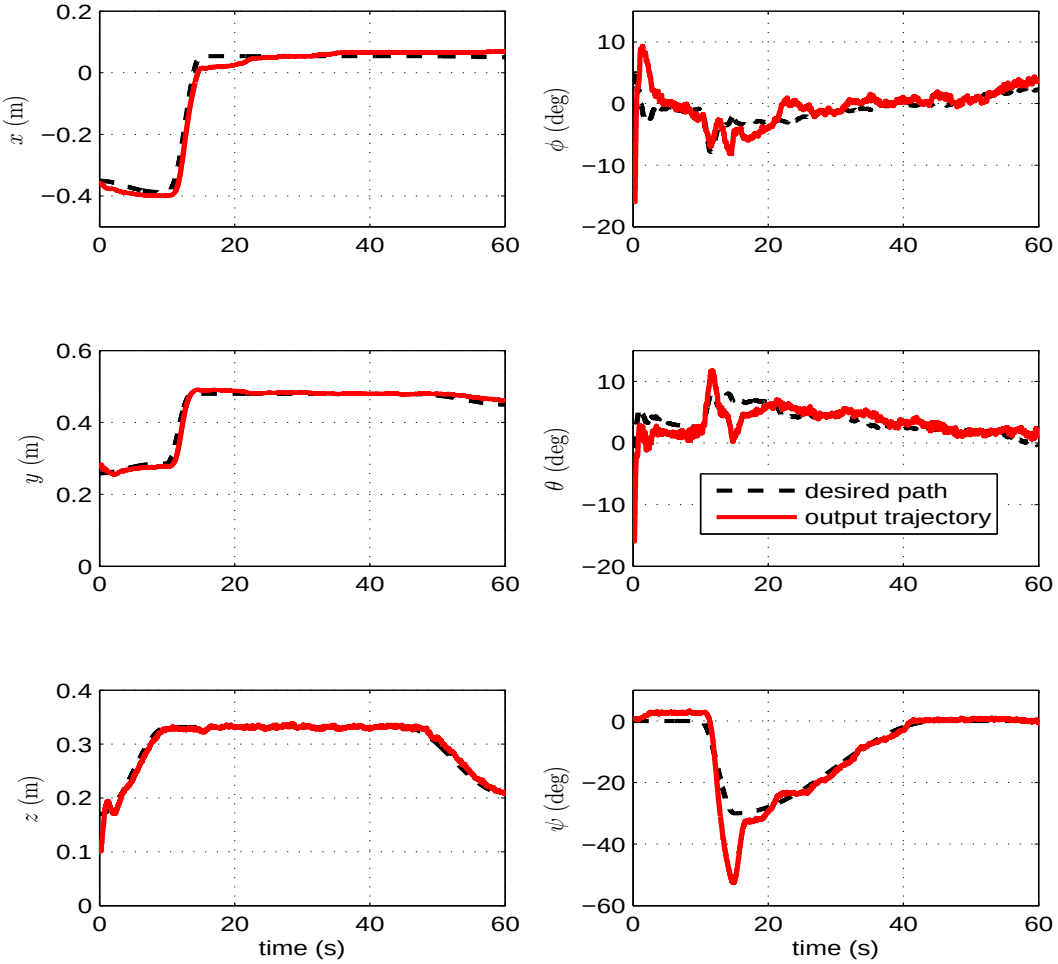

FIGURE 3.5: Tracking control results by PID control with a reduced-order observer.

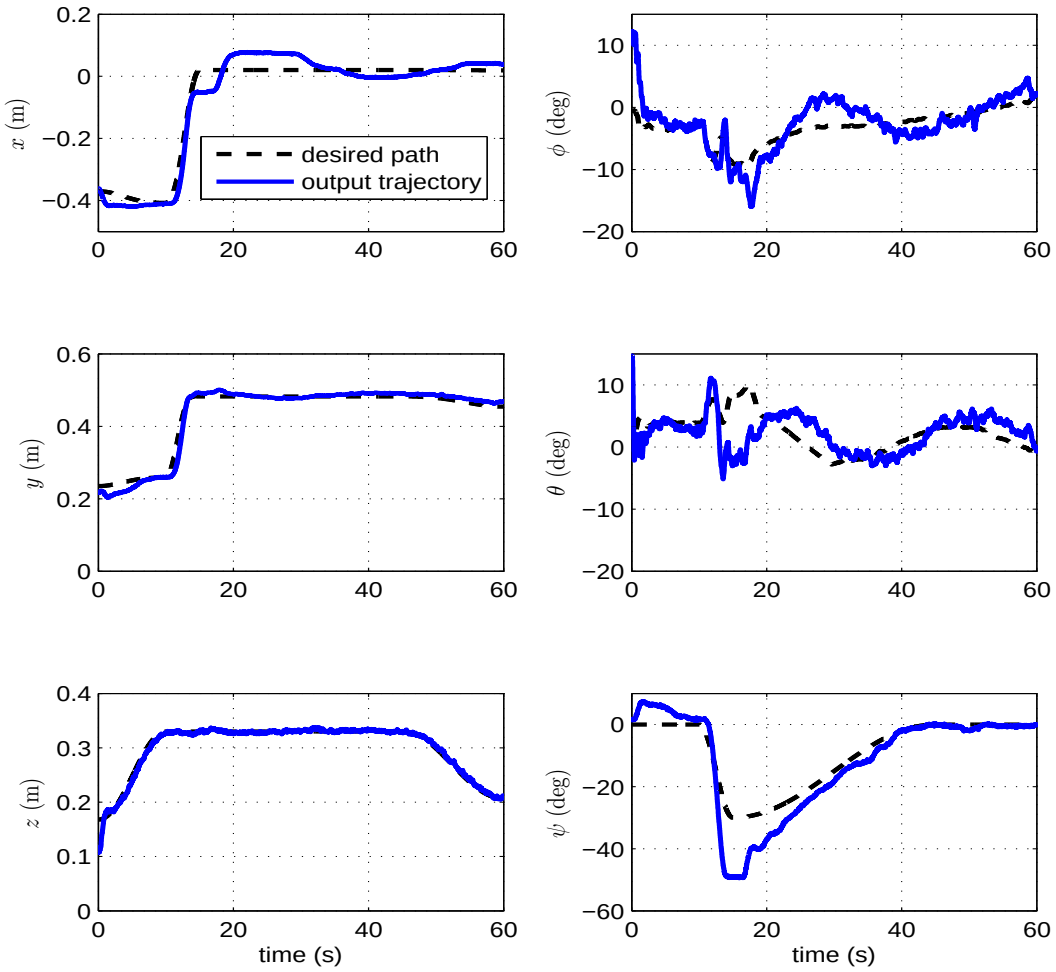

FIGURE 3.6: Tracking control results by PID control with a backward-difference method.

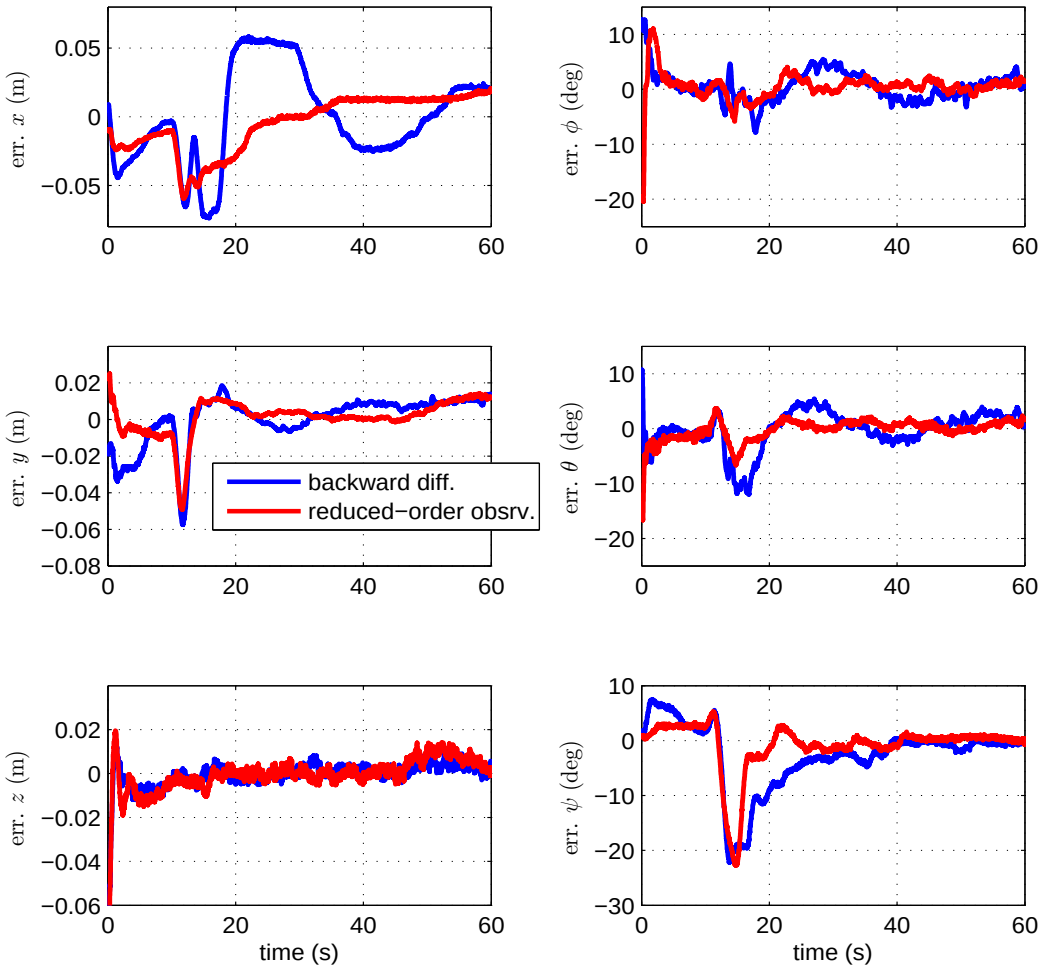

FIGURE 3.7: Tracking error with a reduced-order observer and a backward-difference method.

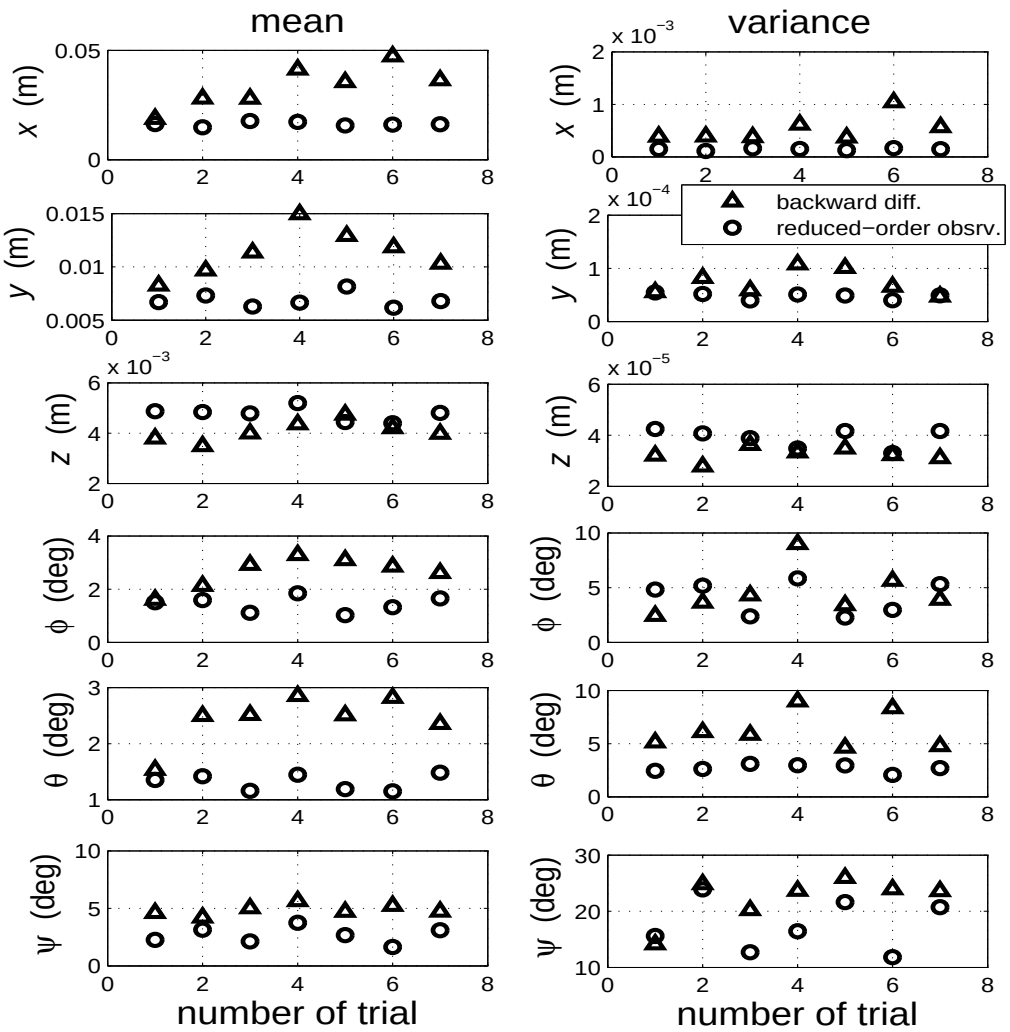

FIGURE 3.8: RMSE and error variance with a reduced-order observer and a backward-difference method.

TABLE 3.1: Average of RSME and error variance (Var) for all trials in Fig. 3.8.

	Backward-diff.		Reduced-order		Ratio $\frac{\text{A-B}}{\text{A}}$ (%)
	Average of RMSE (A)	Average of Var	Average of RMSE (B)	Average of Var	
x (mm)	33.57	0.534	16.299	0.145	51.45
y (mm)	11.325	0.074	6.865	0.048	39.38
z (mm)	4.076	0.032	4.761	0.039	-16.81
ϕ (deg)	2.638	4.609	1.435	4.111	45.59
θ (deg)	2.438	6.252	1.313	2.69	46.12
ψ (deg)	4.872	22.318	2.672	17.54	45.16

3.6 Conclusion

In this chapter, the overdetermined problem in the translational motion dynamics of the quadcopter is solved by applying the least-squares method to determine the input in this motion. The original dynamics of the quadcopter which is categorized as an underactuated system is transformed into a simple decoupled linear form by introducing the synthetic input for simplifying the controller design. Furthermore, a general closed-loop controller configuration for a quadcopter is presented. Therefore, any control strategy can be applied for the quadcopter.

A velocity state estimator for the experimental quadcopter testbed based on the sampled-data of position measurements is presented. The effectiveness of this estimator based on the reduced-order observer is confirmed experimentally. A PID tracking controller is designed for stabilizing and tracking a desired trajectory. We have also shown comparison results with a backward-difference method combined with a low-pass filter. In experiments, the reduced-order observer estimates the velocity states of a quadcopter from its initial value within 25 ms (after 5-th sampling). Therefore, it is useful from a practical application point of view. The reduced-order observer allows us to choose the gains of closed-loop controller relatively higher. Hence, the tracking error can be largely reduced. This method reduces the RMSE of tracking error and variance of velocity signal from the backward-difference method by 35.15% and 81.08% on average, respectively. Reliability of the proposed method was also confirmed through multiple times experiments.

Chapter 4

Chatter Reduction in Sliding Mode Control for Energy Saving Controller of a Quad-Rotor Helicopter

4.1 Introduction

A quadcopter has highly nonlinear and time-varying behavior because it is always influenced by unpredictable disturbances, such as wind gusts. Therefore, an advanced control strategy is required to achieve good performance during autonomous flight. SMC strategy is a well known robust controller against disturbance, uncertainty, and unmodeled dynamics, because it has invariant characteristics in the sliding mode condition, and has been applied to a quadcopter [4, 7, 8, 14, 21, 24, 43, 44, 48–51, 53, 54, 60, 86]. The invariant characteristics of SMC strategy is generated by the switching function in the controller design which produces chattering phenomenon. Practically, this chatter should be avoided or at least reduced because it can harms the actuator. In addition, this chatter leads the actuator consuming more energy in its application. Designing a boundary layer near the sliding surface becomes a common method to reduce the chattering phenomenon [46, 49, 58, 59, 62, 87, 88]. Inside this boundary layer, the discontinuous function is replaced with a continuous one.

In this chapter, SMC strategy is applied for a robust controller of a quadcopter with the control structure presented in the previous chapter. An energy saving through the controller design is addressed by chatter reduction with the boundary layer method in [59]. An integral sliding surface is utilized to improve the tracking performance. The reaching rate is increased by using a constant plus proportional reaching law. To show the effectiveness of the proposed approach, a trajectory tracking control experiment under a significant wind gust is performed. Energy

consumption is evaluated to verify the effectiveness of the proposed approach. This chapter is related to the works presented in [83].

4.2 Controller Design

In Chapter 2, the dynamics of a quadcopter is derived by neglecting aerodynamics and gyroscopic effects, and it is represented in a simple decoupled form in Chapter 3. Considering the aerodynamics and gyroscopic effects together with the wind effect as disturbances, the decoupled dynamics of the quadcopter is rewritten as follows:

$$\ddot{\xi} = v + \rho_d \tag{4.1}$$

where ρ_d is the disturbance vector. A stabilizer and tracking controller based on SMC strategy is designed for the dynamics given in Eq. (4.1). In SMC design, firstly, a stable sliding surface is determined. Secondly, a robust control strategy is designed to force the system into the sliding surface.

4.2.1 Design of Sliding Surface

Let us consider a vector of tracking error in the translational and rotational motions of the quadcopter as follows:

$$\varepsilon = \xi_d - \xi \tag{4.2}$$

where $\xi_d = [x_d, y_d, z_d, \phi_d, \theta_d, \psi_d]^T$ is a vector of desired position and attitude of the quadcopter for $\xi = [x, y, z, \phi, \theta, \psi]$. Because the dynamics of quadcopter is a second-order system as shown in Eq. (4.1), the sliding surface for each motion s_i can be designed as follows [59]:

$$s_i = \dot{\varepsilon}_i + \lambda_i \varepsilon_i; \qquad i = 1, 2, \ldots, 6. \tag{4.3}$$

where ε_i is the element of ε, $\dot{\varepsilon}_i$ is the first derivative of ε_i, λ_i is a positive gain, and s_i is a sliding surface for each motion.

To improve the tracking performance, an integral part is added to Eq. (4.3), and we have the sliding surface equation as follows [62]:

$$s_i = \dot{\varepsilon}_i + \lambda_i \varepsilon_i + \alpha_i \int_0^t \varepsilon_i(\tau) \mathrm{d}\tau, \tag{4.4}$$

where α_i is a positive gain.

4.2.2 Sliding Mode Control

The control objective is to force the system into the sliding mode, where

$$s = 0; \qquad s = [s_1, s_2, \cdots, s_6]^T \tag{4.5}$$

Once the system reach the sliding surface, the controller maintains this sliding mode condition and the robustness is provided. Furthermore, the tracking error converges to zero exponentially. Therefore it is important to force the system into the sliding mode condition immediately.

Considering the sliding surface in Eq. (4.3), the control system dynamics is written as

$$\dot{s} = \ddot{\varepsilon} + \lambda \dot{\varepsilon} \tag{4.6}$$

where $\lambda = \text{diag}\{\lambda_i\}$. Taking the second derivative of Eq. (4.2) and substituting it into Eq. (4.6) along with the dynamics in Eq. (4.1), we have

$$\dot{s} = \dddot{\xi}_d - v - \rho_d + \lambda \dot{\varepsilon} \tag{4.7}$$

To achieve the condition in Eq. (4.5), we consider the synthetic control input v with a constant plus proportional rate reaching law as follows:

$$v = \hat{u} + ks + q\,\text{sign}(s) \tag{4.8}$$

where $k = \text{diag}\{k_i\}$ and $q = \text{diag}\{q_i\}$ with positive elements, and sign(.) is a signum function defined as follows:

$$\text{sign}(s) = \begin{cases} 1 & \text{if } s > 0 \\ 0 & \text{if } s = 0 \\ -1 & \text{if } s < 0 \end{cases}$$

$\hat{u}$ is an equivalent control input for dynamics in Eq. (4.7) as follows:

$$\hat{u} = \dddot{\xi}_d + \lambda \dot{\varepsilon} \tag{4.9}$$

If we consider the integral sliding surface equation in Eq. (4.4), then the equivalent control input $\hat{u}$ is as follows:

$$\hat{u} = \dddot{\xi}_d + \lambda \dot{\varepsilon} + \alpha \varepsilon \tag{4.10}$$

where $\alpha = \text{diag}\{\alpha_i\}$. The sign(.) function in Eq. (4.8) causes discontinuity in the control signal and produces chatter that should be avoided. This chattering phenomenon can be eliminated by

smoothing the control discontinuity in a thin boundary layer, β_i, neighboring the sliding surface [58, 59]. The sign(.) function is replaced by a saturation function, sat(.), as follows:

$$\text{sat}(s_i) = \begin{cases} \text{sign}(s_i) & \text{if}|s_i| > \beta_i \\ \dfrac{s_i}{\beta_i} & \text{if}|s_i| \leq \beta_i \end{cases} \tag{4.11}$$

where $\beta_i > 0$.

Substituting Eq. (4.8) into Eq. (4.1), we have the closed-loop dynamics for the sliding surface in Eq. (4.3) as follows:

$$\ddot{\varepsilon} + \lambda\dot{\varepsilon} + ks + q\,\text{sign}(s) + \rho_d = 0 \tag{4.12}$$

and for the integral sliding surface in Eq. (4.4) is as follows:

$$\ddot{\varepsilon} + \lambda\dot{\varepsilon} + \alpha\varepsilon + ks + q\,\text{sign}(s) + \rho_d = 0 \tag{4.13}$$

By applying the sat(.) function in Eq. (4.11), the closed-loop dynamics inside the boundary layer behaves as the PD-based control system in Eq. (4.12) in which "$k_i\lambda_i + \frac{q_i\lambda_i}{\beta_i}$" is a proportional gain and "$k_i + \lambda_i + \frac{q_i}{\beta_i}$" is a differential gain, and the PID-based control system in Eq. (4.13) in which "$k_i\lambda_i + \alpha_i + \frac{q_i\lambda_i}{\beta_i}$" is a proportional gain, "$k_i\alpha_i + \frac{q_i\alpha_i}{\beta_i}$" is an integral gain, and "$k_i + \lambda_i + \frac{q_i}{\beta_i}$" is a differential gain. We later compare the performance of SMC strategy with these PD and PID controllers experimentally to verify the net effectiveness of the sign(.) and sat(.) terms.

4.3 Stability Analysis

The control inputs designed in SMC strategy must guarantee the existence of the sliding mode condition in Eq. (4.5). Once the sliding mode condition is achieved, the stability of the system is guaranteed by the stability of the sliding surface.

4.3.1 Existence of Sliding Mode

The control input in Eq. (4.8) is designed independently for each DOF. To ensure the stability of the control input in Eq. (4.8), let us consider the Lyapunov function candidate for each DOF as follows:

$$V_i = \frac{1}{2}s_i^2 \tag{4.14}$$

Taking the first derivative of Eq. (4.14) by considering Eqs. (4.7) and (4.8) in each DOF, we have

$$\dot{V}_i = s_i(-k_i s_i - q_i\text{sign}(s_i) - \rho_{di}) \tag{4.15}$$

where k_i, q_i are component of diagonal matrices k and q respectively, and ρ_{di} is component of vector ρ_d. Suppose there exists a positive constant γ_i where

$$|\rho_{di}| < \gamma_i \tag{4.16}$$

we have

$$\dot{V}_i < s_i(-k_i s_i - q_i \text{sign}(s_i) - \gamma_i) \tag{4.17}$$

Choosing $k_i > 0$ and $q_i > \gamma_i$, $\dot{V}_i$ is negative definite, and therefore the stability of the control input in Eq. (4.8) for each DOF is guaranteed, and overall system is stable. Hence, the sliding mode condition in Eq. (4.5) is achieved.

If the function in Eq. (4.15) is replaced by the sat(.) function in Eq. (4.11), then the stability beyond the boundary layer is also guaranteed. Hence, once entering the boundary layer, the control law in Eq. (4.8) ensures that the trajectory remains inside the boundary layer.

4.3.2 Stability of Sliding Surface

In this works, we utilize two types of sliding function as given in Eqs. (4.3) and (4.4) which are named as PD-based sliding surface and PID-based sliding surface, respectively. In the sliding mode condition, the stability of the system is guaranteed by the stability of the sliding function as follows.

4.3.2.1 PD-based Sliding Surface

Considering the sliding surface in Eq. (4.3), the dynamics of the sliding mode condition in Eq. (4.5) is as follows:

$$\dot{\varepsilon}_i = -\lambda_i \varepsilon_i \tag{4.18}$$

To guarantee the stability of this dynamics, let us consider the Lyapunov function candidate as follows:

$$V_i = \frac{1}{2}\varepsilon_i^2 \tag{4.19}$$

Taking the first derivative of Eq. (4.19) by considering Eq. (4.18), we have

$$\dot{V}_i = -\lambda_i \varepsilon_i^2 \tag{4.20}$$

Because $\lambda_i > 0$ then $\dot{V}_i$ is negative definite and therefore the sliding surface in Eq. (4.3) is stable. Hence ε_i converges to zero exponentially.

4.3.2.2 PID-based Sliding Surface

Considering PID-based sliding surface in Eq. (4.4), the dynamics in the sliding mode condition is as follows:

$$\dot{\varepsilon}_i = -\lambda_i \varepsilon_i - \alpha_i \int_0^t \varepsilon_i(\tau) \mathrm{d}\tau, \tag{4.21}$$

The stability of the sliding mode dynamics in Eq. (4.21) is evaluated by using Routh-Hurwitz criterion. By choosing $\lambda_i > 0$ and $\alpha_i > 0$ the dynamics in Eq. (4.21) has negative poles and therefore its stability is guaranteed. Hence ε_i converges to zero exponentially.

4.4 Experiments

The effectiveness of the proposed methods are experimentally evaluated in terms of robustness and energy efficiency using the experimental quadcopter testbed shown in Fig. 2.2.

4.4.1 Robustness Evaluation

This section shows experimental results of the proposed control strategies in hovering stabilization and trajectory tracking using a quadcopter testbed. We evaluate the performance of SMC strategy with sign(.) and sat(.) functions. The contribution of integral sliding surface to improve tracking performance is also evaluated. In these experiments, the quadcopter performs six types of motions during 60 seconds as follows: 1: take-off motion from A to B (0-10 s), 2: maneuver in the $x-y$ plane from B to C (10-15 s), 3: hovering by performing yaw motion at C (15-30 s), 4: maneuver from C to B (30-34 s), 5: hovering by performing yaw motion at B (35-50 s) and 6: landing motion from B to A (50-60 s). This desired trajectory is given in Fig. 4.1.

The control parameters are tuned to provide the best experimental results and are obtained as follows (units are omitted):

$$\begin{aligned}
k &= \mathrm{diag}\{6.5, 6, 16, 22, 20, 70\}, \\
\lambda &= \mathrm{diag}\{3, 4, 9, 8, 7, 40\}, \\
q &= \mathrm{diag}\{0.6, 0.6, 1, 0.8, 0.8, 1\}, \\
\alpha &= \mathrm{diag}\{0.5, 0.5, 0.6, 0.4, 0.2, 0.6\}.
\end{aligned}$$

For the sat(.) function, the boundary layer is designed with $\beta = \mathrm{diag}\{0.2, 0.2, 0.2, 0.38, 0.3, 0.2\}$. The values of $\beta = \mathrm{diag}\{\beta_i\}$ should be designed properly, because if we choose a relatively small value, the chatter still occurs, while a relatively large β will reduce the robustness. By using the

profile of sliding surface s for each motion as shown in Fig. 4.2, we can choose proper values of β.

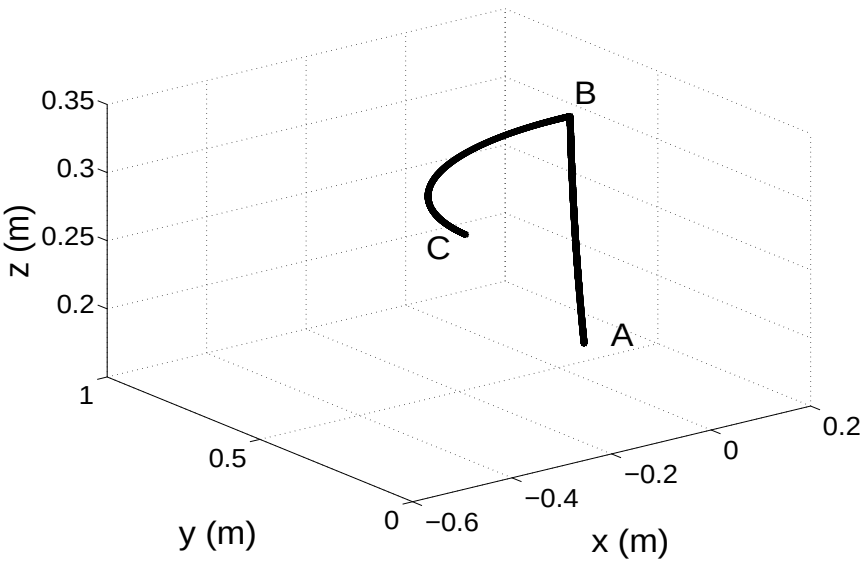

FIGURE 4.1: Desired trajectory in $x-y-z$ coordinate system.

In the experiments, we compared the following controllers:

- C1: Sliding mode control with sign(.) function by using sliding surface in Eq. (4.3),
- C2: Sliding mode control with sat(.) function by using sliding surface in Eq. (4.3),
- C3: PD-based controller,
- C4: Sliding mode control with sign(.) function by using integral sliding surface in Eq. (4.4),
- C5: Sliding mode control with sat(.) function by using integral sliding surface in Eq. (4.4), and
- C6: PID-based controller

in condition without and under wind disturbance. All controllers use the same gains value for fair comparison. The wind disturbance applied in the experiment is produced by an electric fan (power: 57 W).

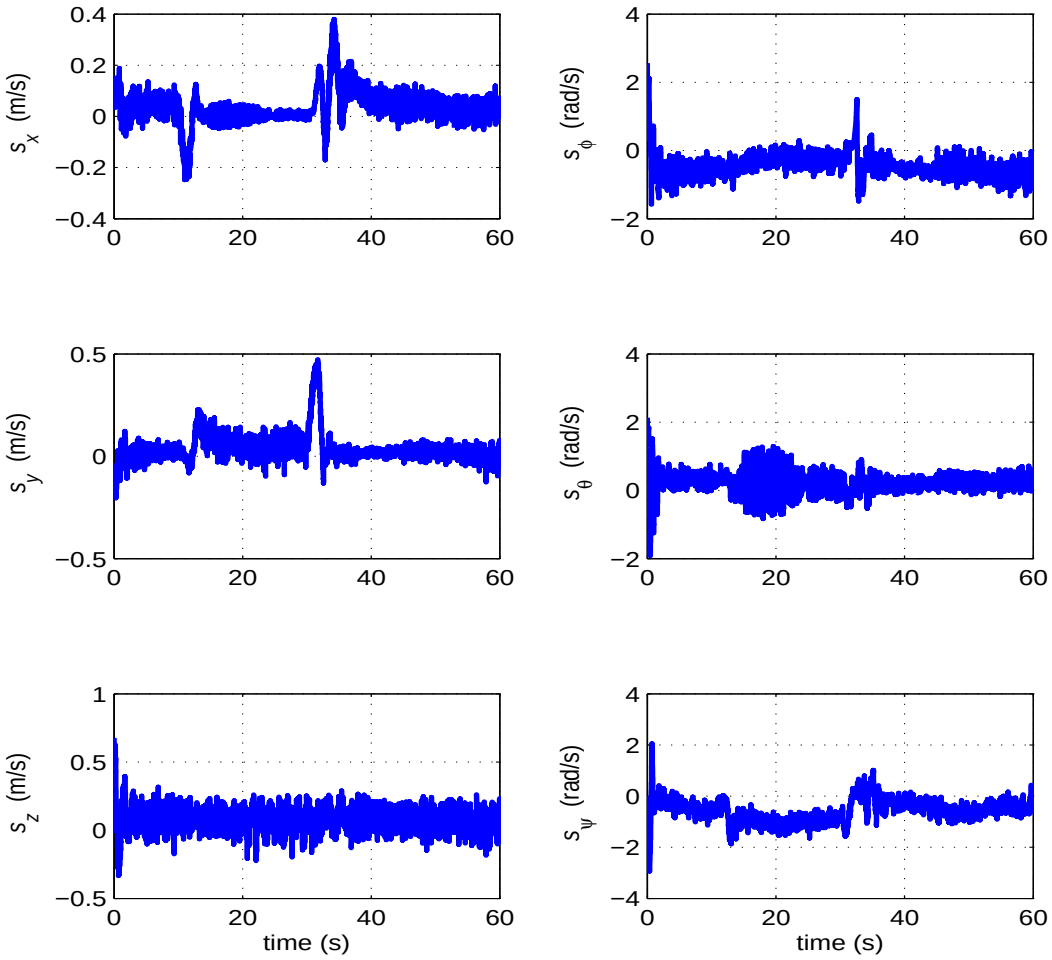

FIGURE 4.2: Profiles of sliding surface for each DOF.

Figures 4.3, 4.4, and 4.5 show the effectiveness of controller C2 to reduce the chattering phenomenon. Controller C3 that uses the same gain with C2 provides smaller tracking error than C2, although it still produces higher chatter than C2, as shown in Figs. 4.4 and 4.5. From the results of controllers C1, C2, and C3, which use the PD-based sliding surface function in Eq. (4.3), relatively high tracking errors are obtained. In order to reduce the tracking error, we design an PID-based sliding surface in Eq. (4.4) for both sign(.) and sat(.) functions, and thus the previous PD controller C3 is changed into a PID controller (C6). The effectiveness of integral part in the PID-based sliding surface design for improving tracking performance is shown in Figs. 4.6 and 4.7. It is seen that the sat(.) function reduces the chattering phenomenon effectively, especially when the quadcopter performs hovering. This chatter reduction is also confirmed in the profiles of control input in Figs. 4.8 and 4.9. The repeatability of this strategy is evaluated by conducting several times experiments in the same condition, and the results are given in Figs. 4.10 and 4.11

for PD-based sliding surface, Figs. 4.12 and 4.13 for PID-based sliding surface. It is seen that on average, the sat(.) function provides relatively small mean and/or variance for both sliding surface function and it is confirmed in Tables 4.1 and 4.2.

TABLE 4.1: Mean and variance of control input for experiment without disturbance.

Contr.	Mean				Variance (10^{-3})			
	u_1 (N)	u_2 (Nm) (10^{-3})	u_3 (Nm) (10^{-3})	u_4 (Nm) (10^{-3})	u_1 (N)	u_2 (Nm)	u_3 (Nm)	u_4 (Nm)
C1	2.206	-45.11	24.009	-240.37	115.982	1.95	1.411	39.578
C2	2.183	-41.94	20.361	-311.9	85.586	1.435	0.811	61.259
C3	2.219	-44.15	21.428	-296.22	121.204	1.419	0.777	76.34
C4	2.222	-30.94	24.505	-240.14	134.679	2.399	2.261	42.378
C5	2.223	-27.81	26.031	-280.66	96.24	1.413	0.838	64.259
C6	2.256	-36.24	20.868	-236.58	130.022	1.414	0.665	68.683

TABLE 4.2: Mean and variance of control input for experiment under wind disturbance.

Contr.	Mean				Variance (10^{-3})			
	u_1 (N)	u_2 (Nm) (10^{-3})	u_3 (Nm) (10^{-3})	u_4 (Nm) (10^{-3})	u_1 (N)	u_2 (Nm)	u_3 (Nm)	u_4 (Nm)
C1	2.219	-47.57	15.837	-245.71	107.979	2.788	1.479	54.871
C2	2.218	-53.19	12.766	-268.86	93.08	2.741	0.913	71.285
C3	2.25	-53.92	12.517	-262.05	122.483	2.972	1.007	80.859
C4	2.213	-27.53	11.54	-175.47	109.374	2.45	1.127	54.486
C5	2.197	-26.05	13.565	-188.6	88.04	2.508	1.156	61.697
C6	2.274	-36.89	10.009	-186.15	120.328	2.258	0.991	78.694

The application of chattering reduction on the sliding mode control by using sat(.) function has negative effect. It reduces the robustness of the system, as confirmed in Figs. 4.14 and 4.15 for the experiments without disturbance, Figs. 4.16 and 4.17 for the experiments under wind disturbance. On average, the sat(.) function provides larger root-squared mean error (RSME) and/or error variance compared to the sign(.) function and PD/PID controller which is confirmed in Tables 4.3 and 4.4. Tables 4.3 and 4.4 also confirm that the original SMC which uses sign(.) function is more robust compared to the conventional controller PD/PID. Controller C1 provides smaller RSME and error variance than controller C3, and controller C4 provides smaller RSME and error variance than controller C6, especially in the experiments under wind disturbance.

TABLE 4.3: Root-squared of mean error (RSME) and error variance (Var) for experiment without disturbance.

	Translational motion		Rotational motion	
	RSME (mm)	Var (mm)	RSME (deg)	Var (deg)
Controller C1	11.698	0.265	2.861	5.301
Controller C2	21.048	0.529	2.841	6.056
Controller C3	16.11	0.334	2.838	5.517
Controller C4	1.096	0.208	1.014	6.062
Controller C5	2.885	0.375	1.052	5.903
Controller C6	1.823	0.264	0.968	5.354

TABLE 4.4: Root-squared of mean error (RSME) and error variance (Var) for experiment under wind disturbance.

	Translational motion		Rotational motion	
	RSME (mm)	Var (mm)	RSME (deg)	Var (deg)
Controller C1	23.946	0.598	2.681	8.206
Controller C2	33.345	0.962	3.018	11.304
Controller C3	27.535	0.686	2.879	10.016
Controller C4	1.777	0.38	0.616	7.367
Controller C5	3.785	0.481	0.648	7.473
Controller C6	2.729	0.406	0.745	7.714

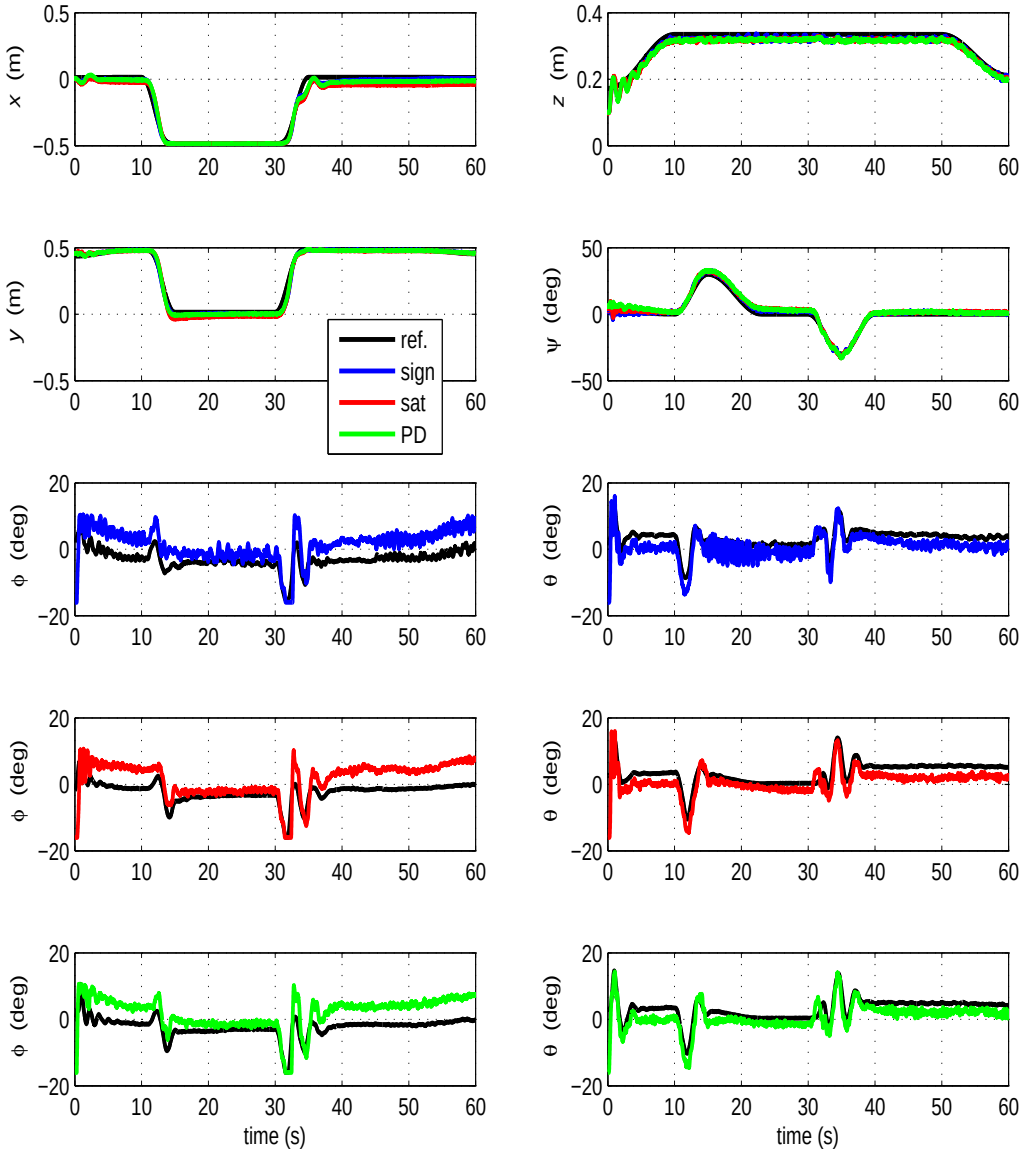

FIGURE 4.3: Trajectory tracking results in all motion for controllers C1, C2, and C3 without disturbance.

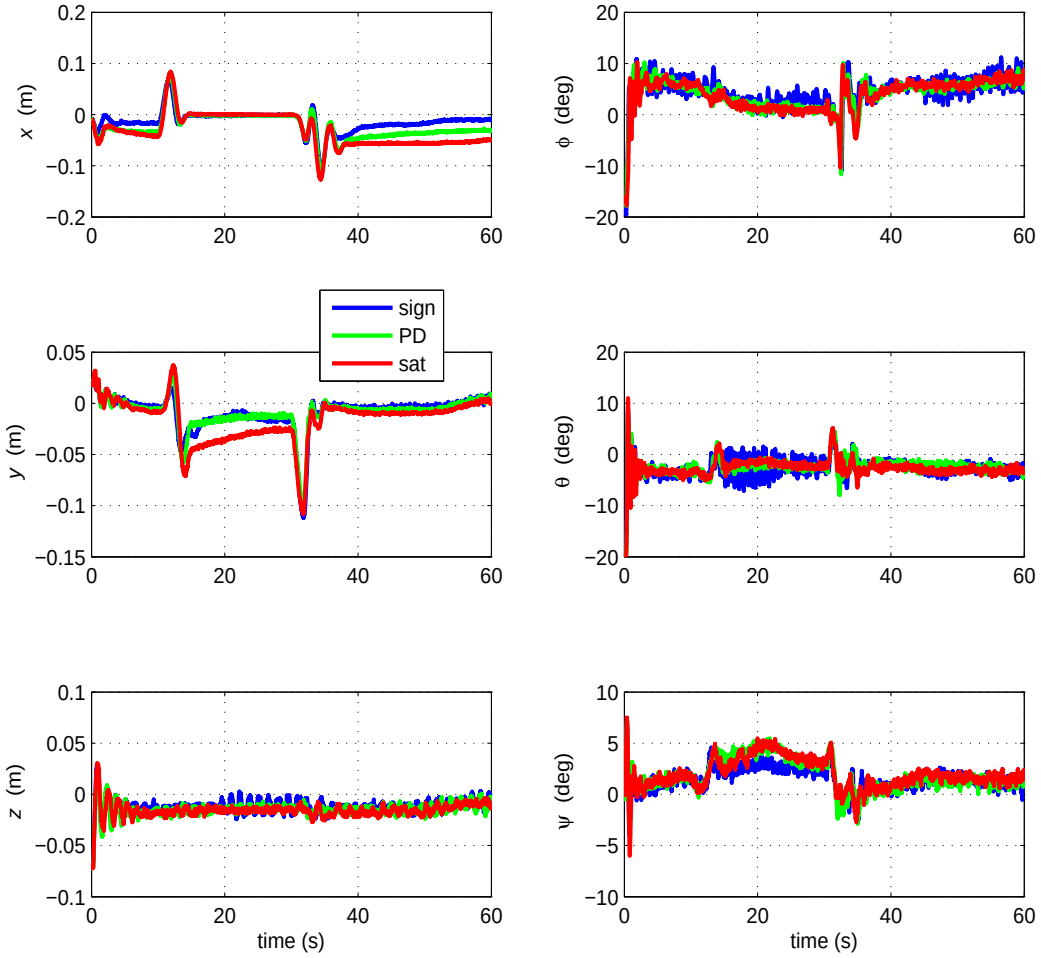

FIGURE 4.4: Tracking error for controllers C1, C2, and C3 without wind disturbance.

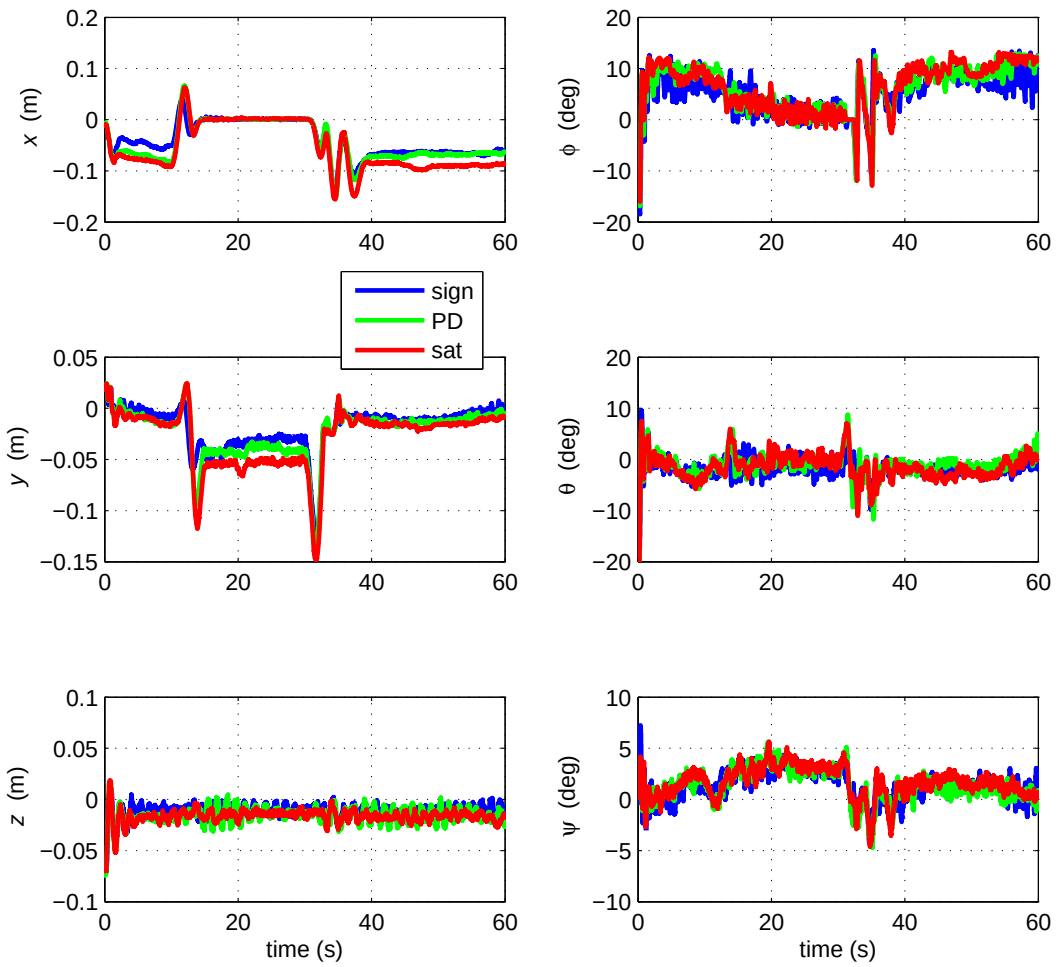

FIGURE 4.5: Tracking error for controllers C1, C2, and C3 under wind disturbance.

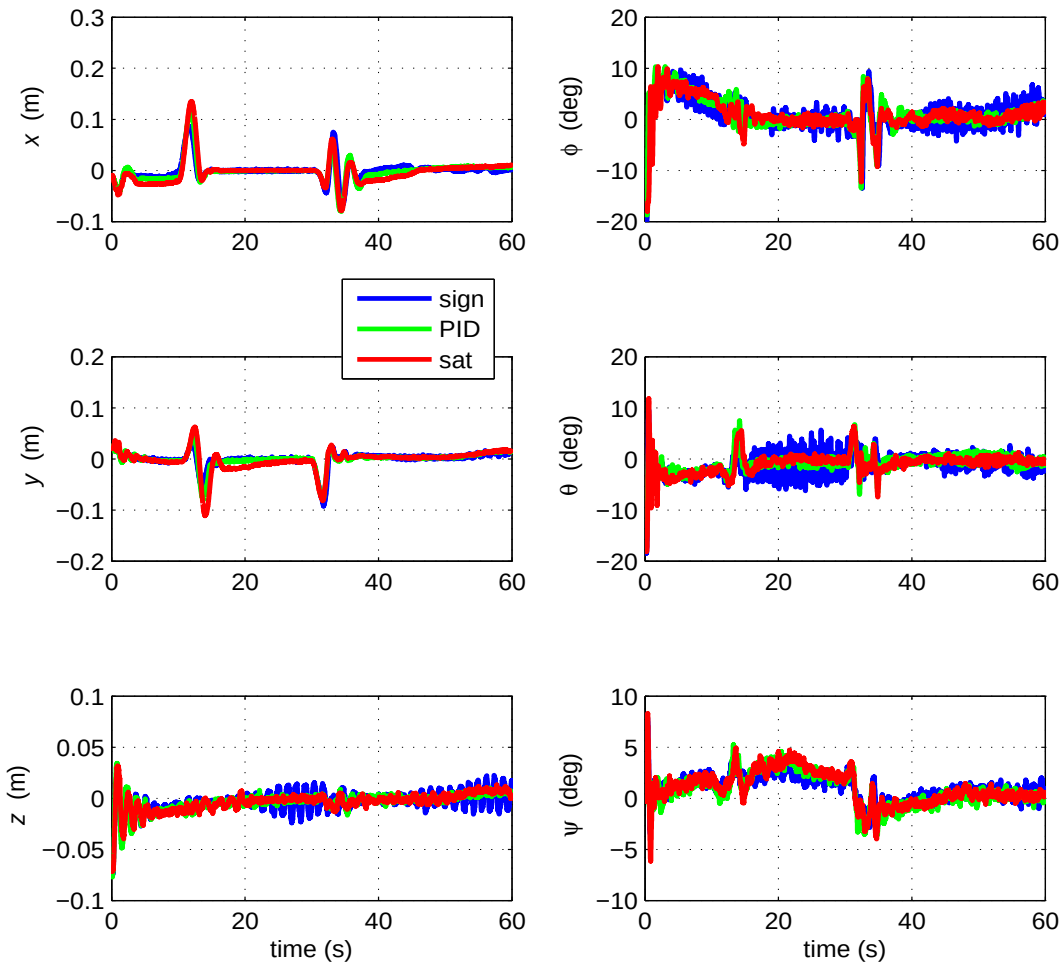

FIGURE 4.6: Tracking error for controllers C4, C5, and C6 without disturbance.

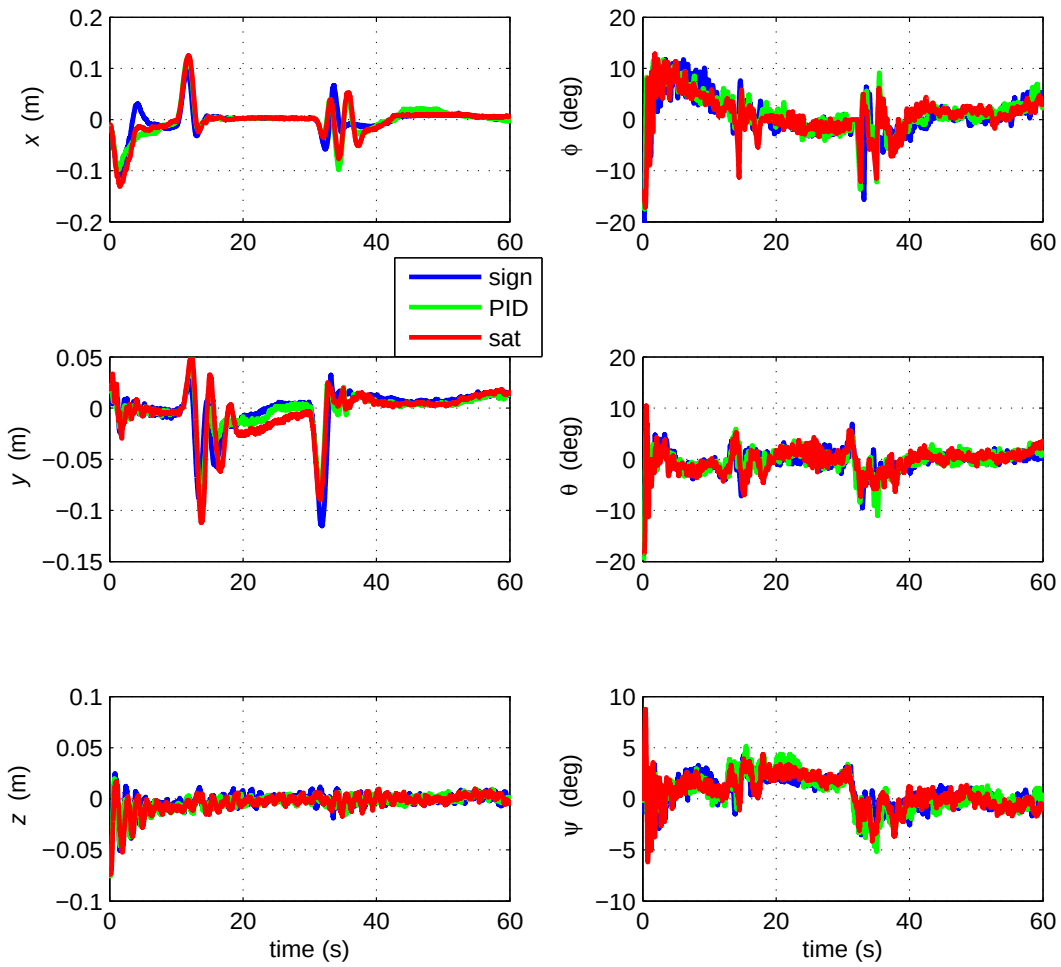

FIGURE 4.7: Tracking error for controllers C4, C5, and C6 under wind disturbance.

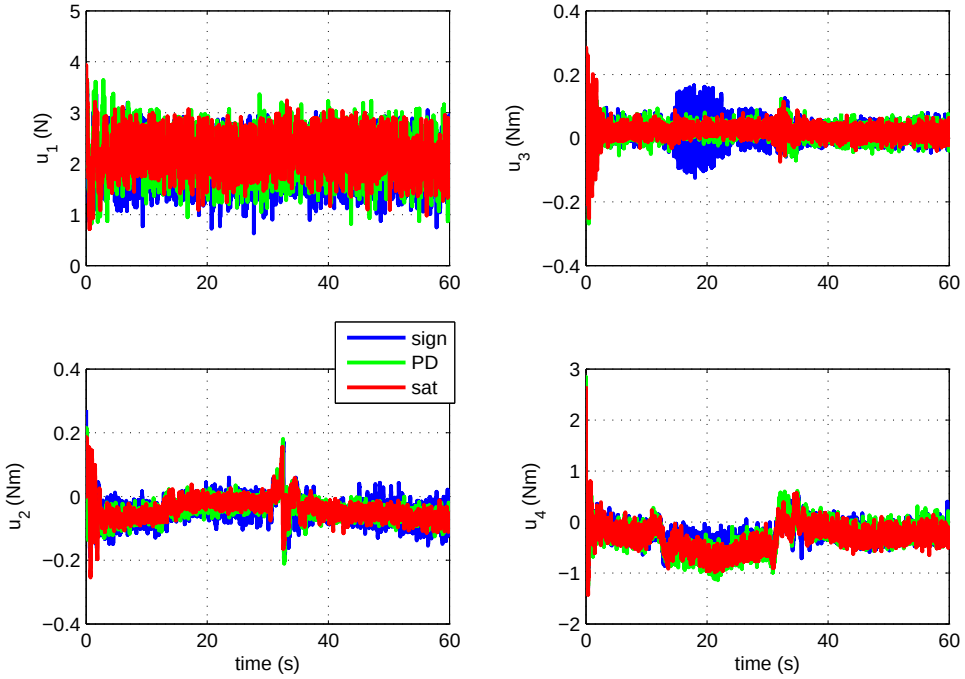

(a)

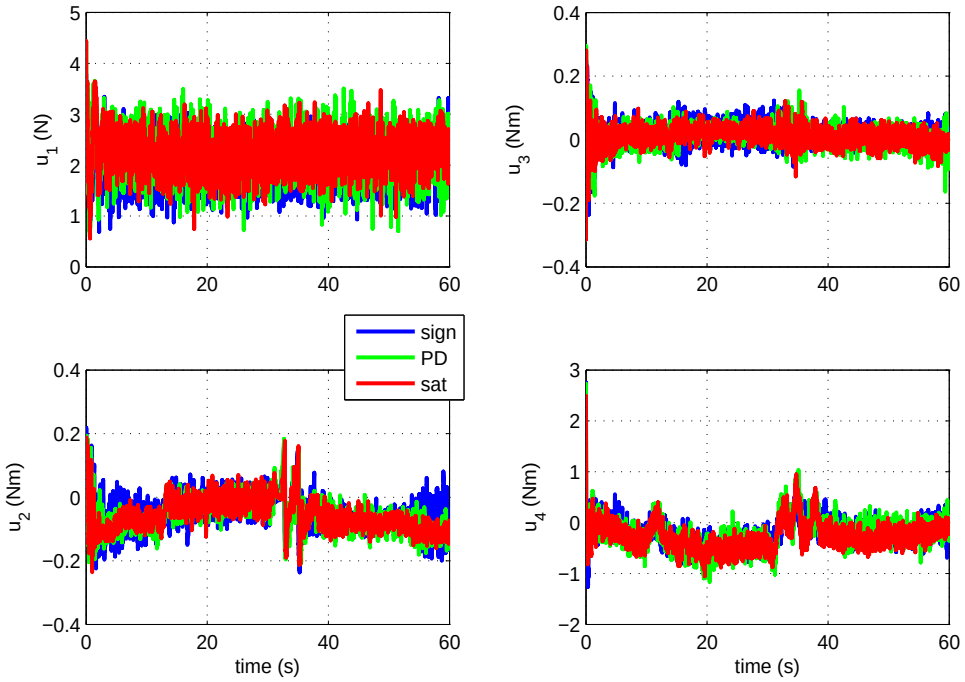

(b)

FIGURE 4.8: Profiles of control input for controllers C1, C2, and C3 (a) without disturbance, (b) under wind disturbance.

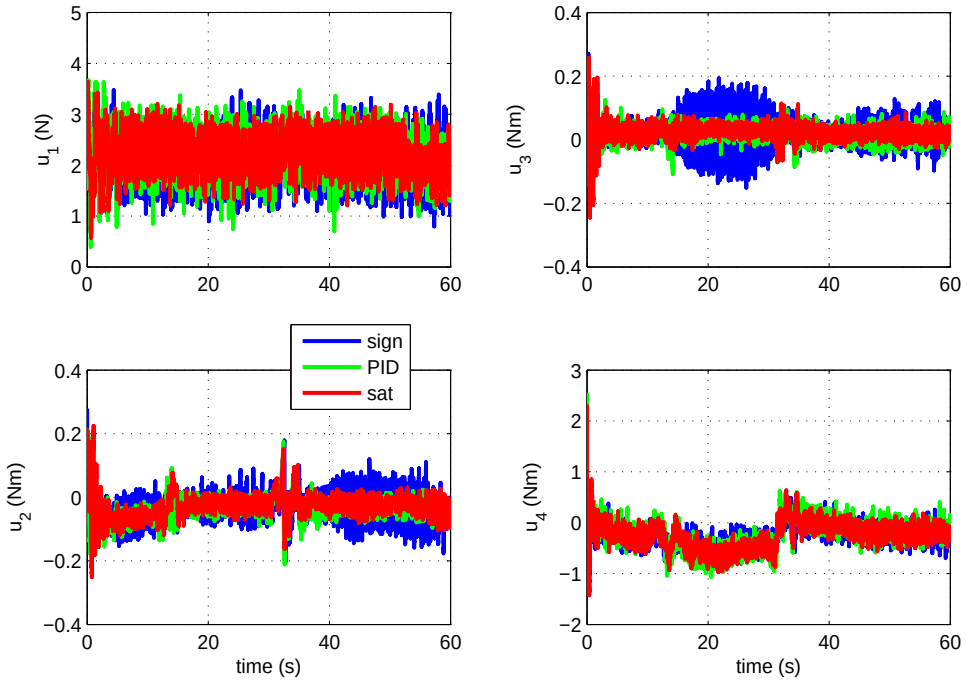

(a)

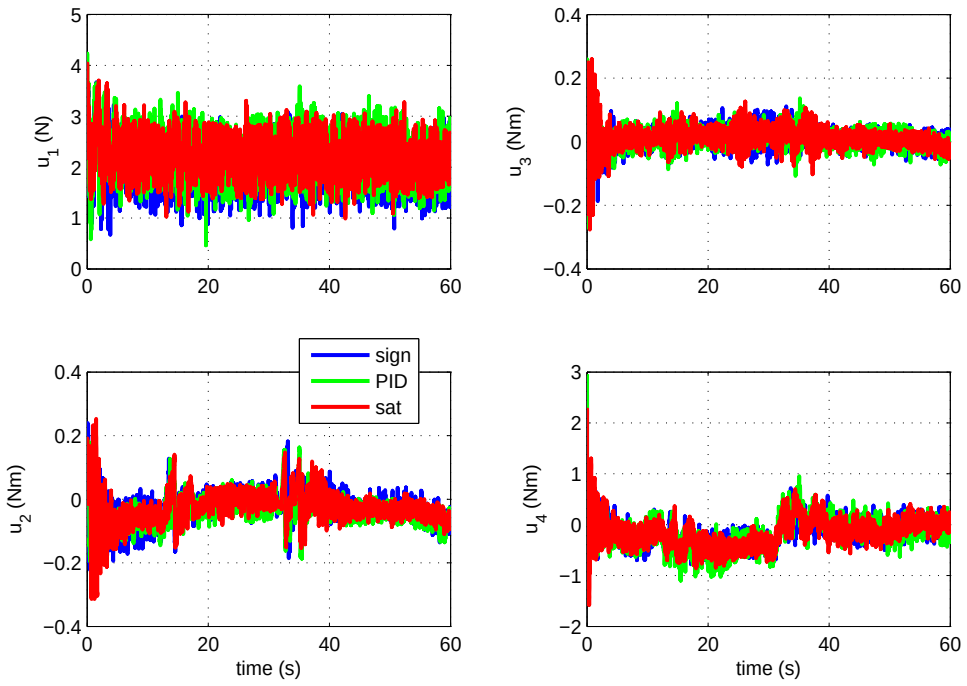

(b)

FIGURE 4.9: Profiles of control input for controllers C4, C5, and C6 (a) without disturbance, (b) under wind disturbance.

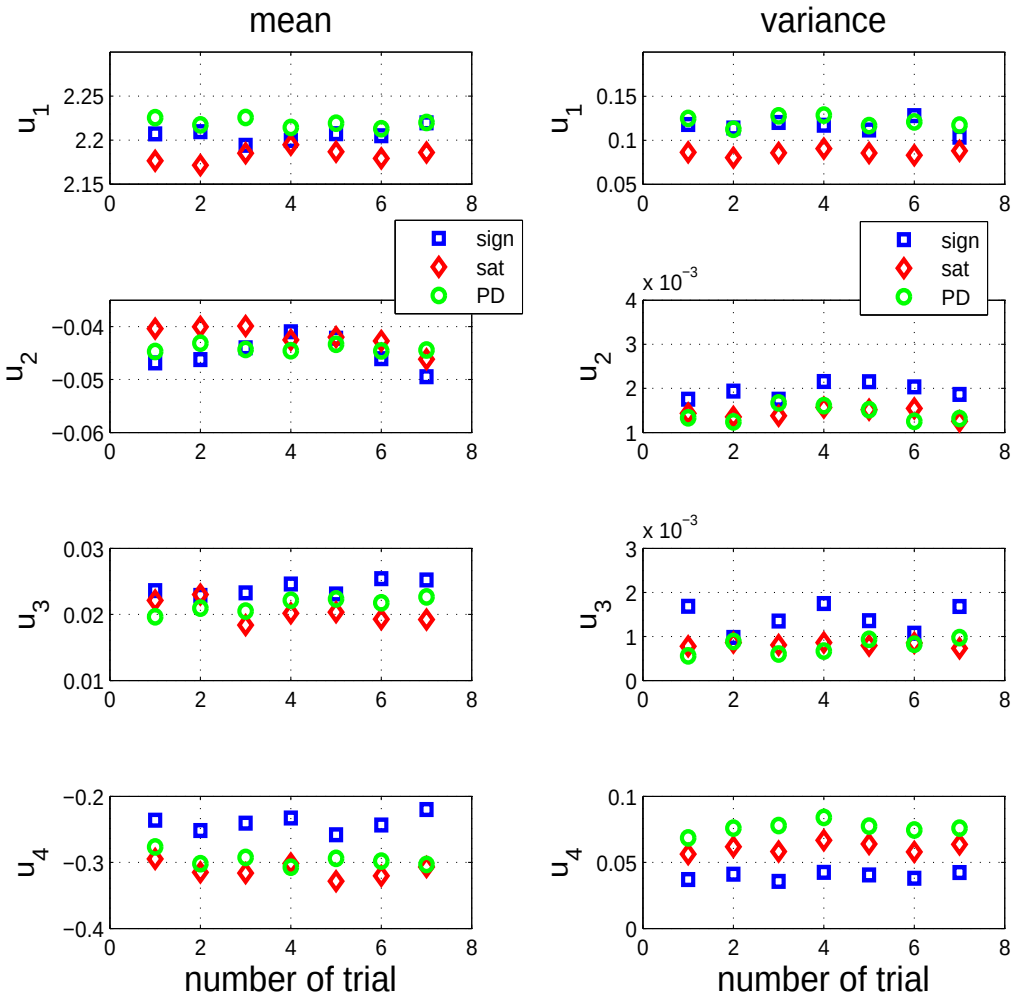

FIGURE 4.10: Mean and variance of control input for multiple times experiments for controllers C1, C2, and C3 without disturbance.

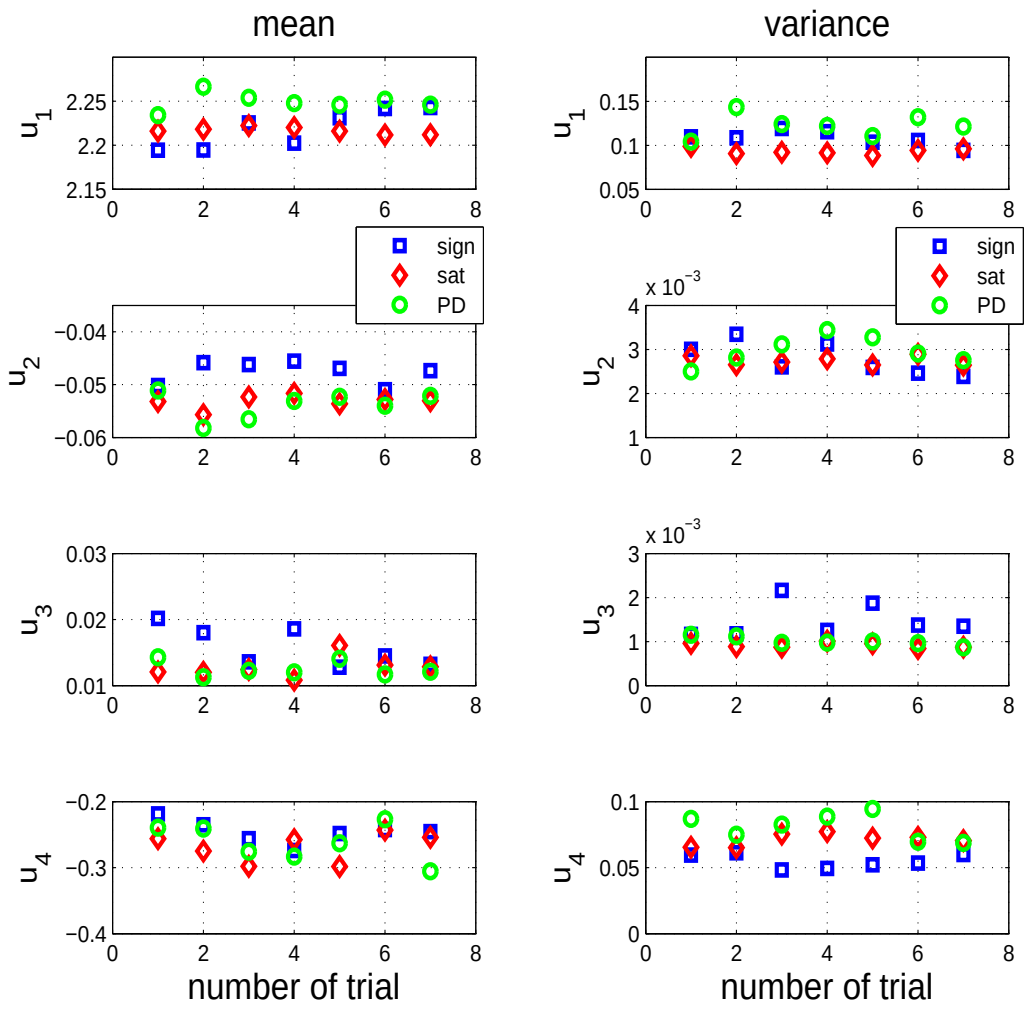

FIGURE 4.11: Mean and variance of control input for multiple times experiments for controllers C1, C2, and C3 under wind disturbance.

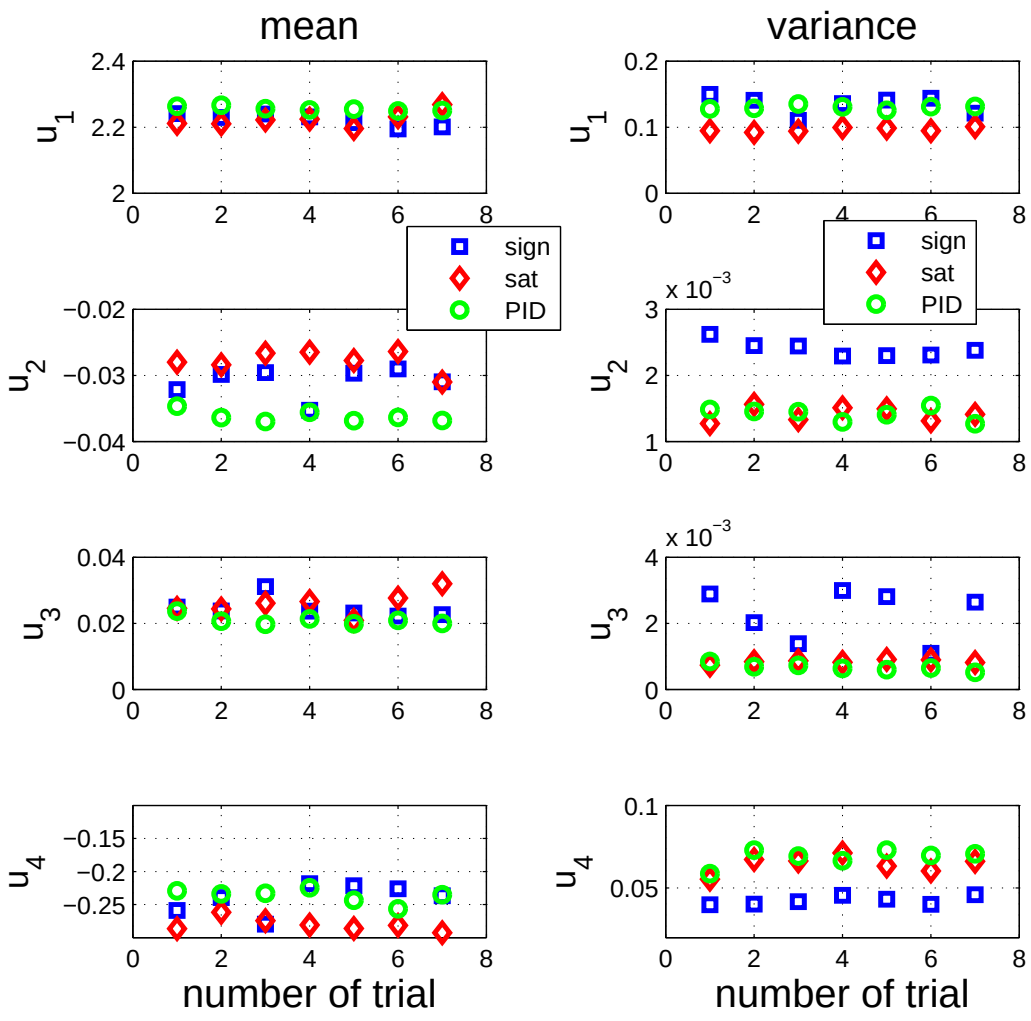

FIGURE 4.12: Mean and variance of control input for multiple times experiments for controllers C4, C5, and C6 without disturbance.

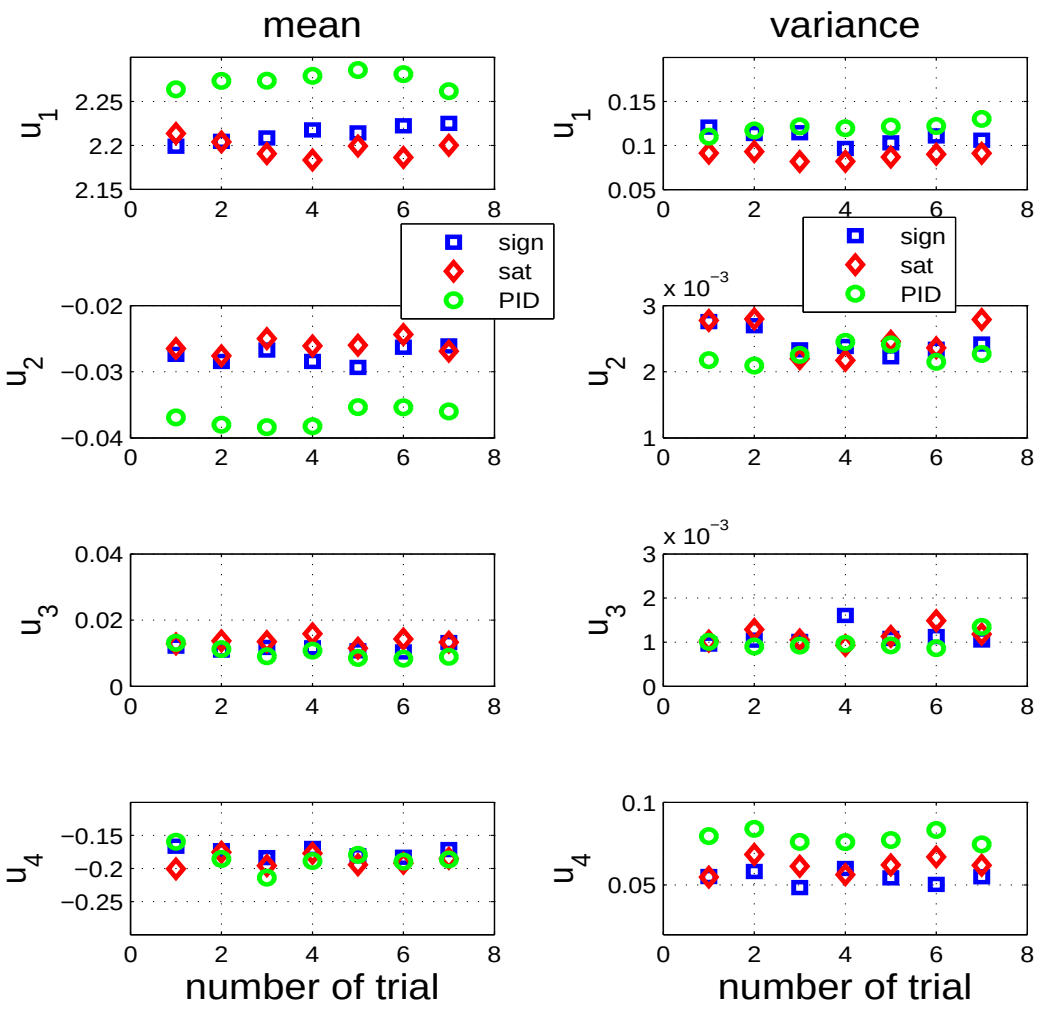

FIGURE 4.13: Mean and variance of control input for multiple times experiments for controllers C4, C5, and C6 under wind disturbance.

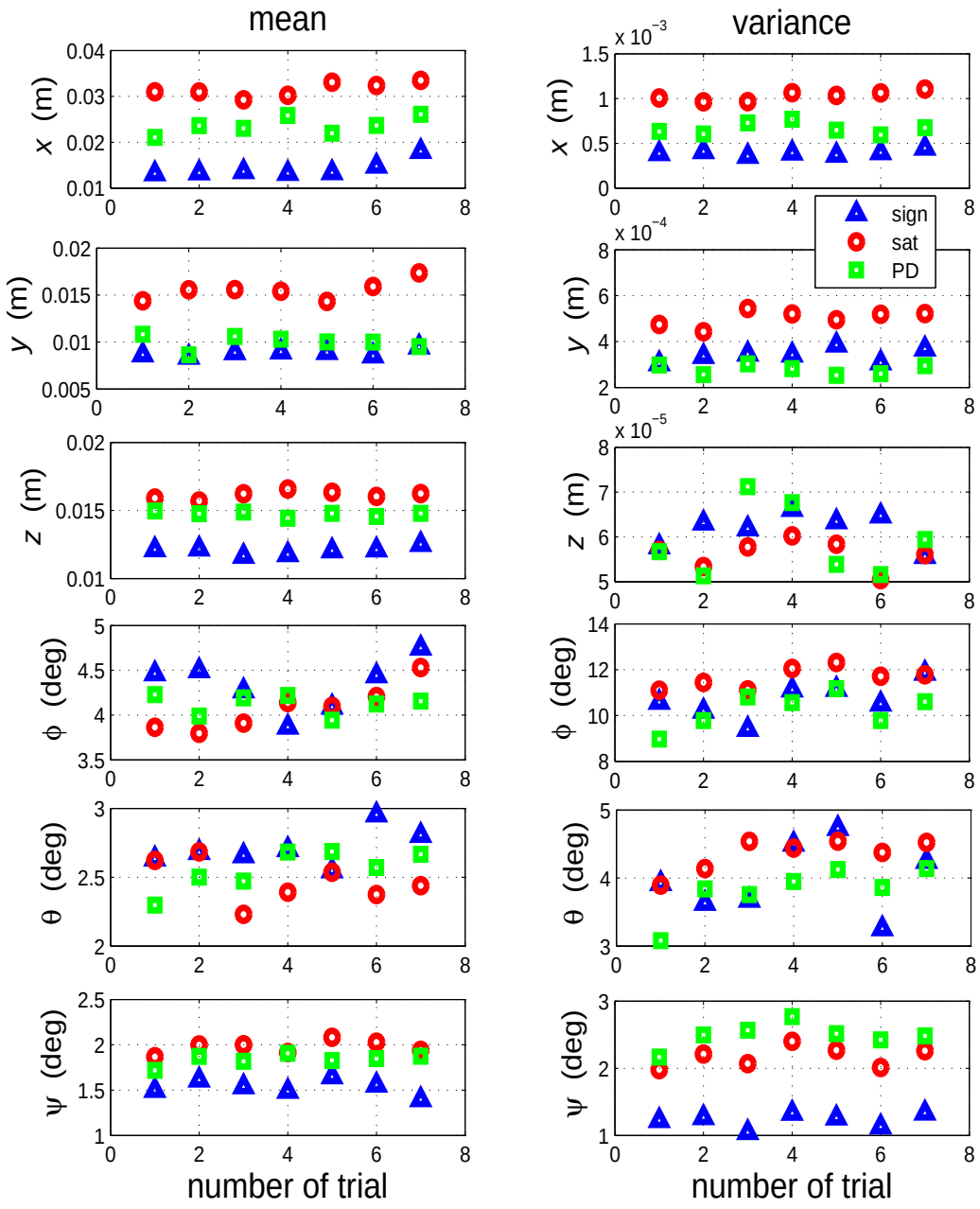

FIGURE 4.14: RSME and error variance for multiple times experiments for controllers C1, C2, and C3 without disturbance.

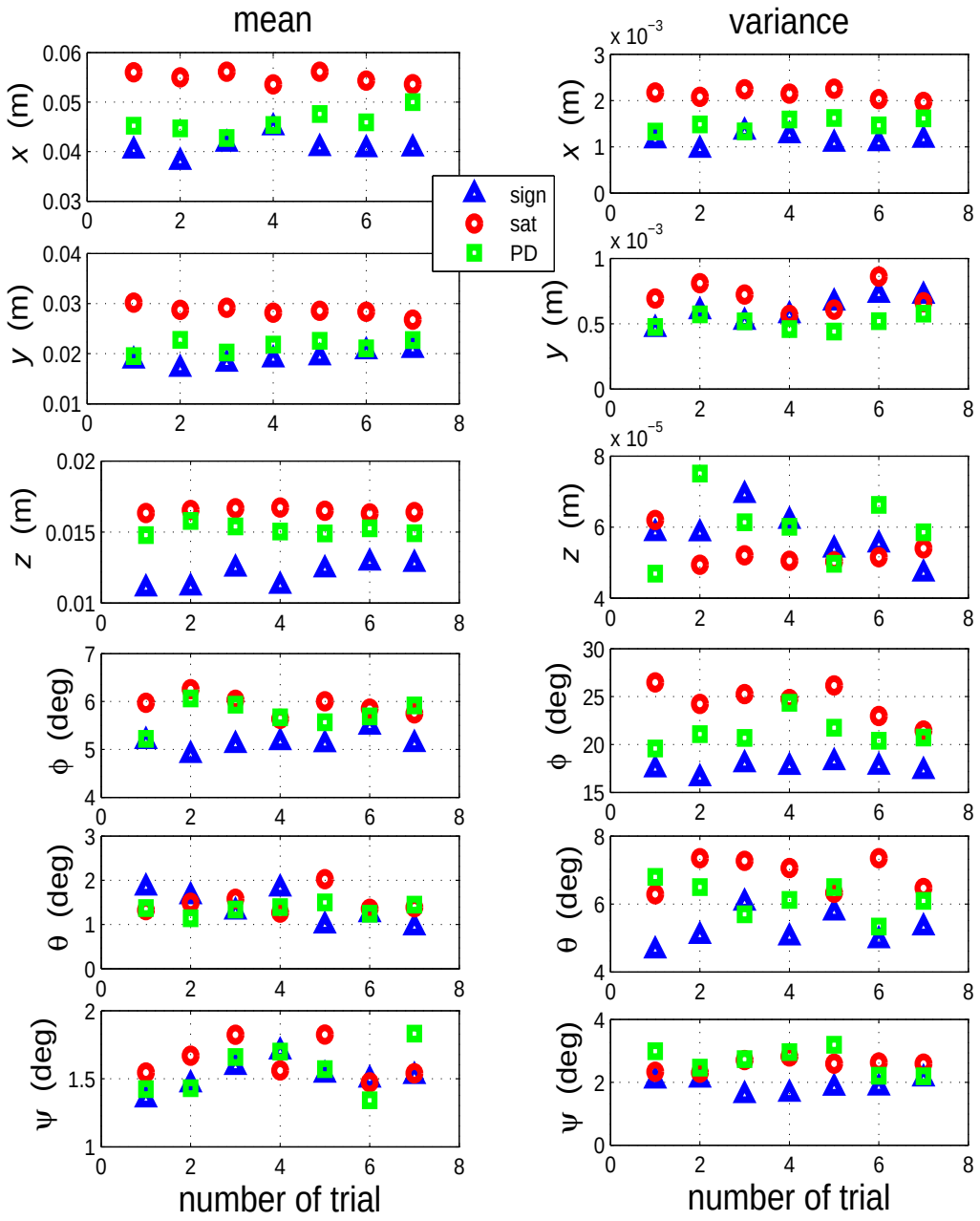

FIGURE 4.15: RSME and error variance for multiple times experiments for controllers C1, C2, and C3 under wind disturbance.

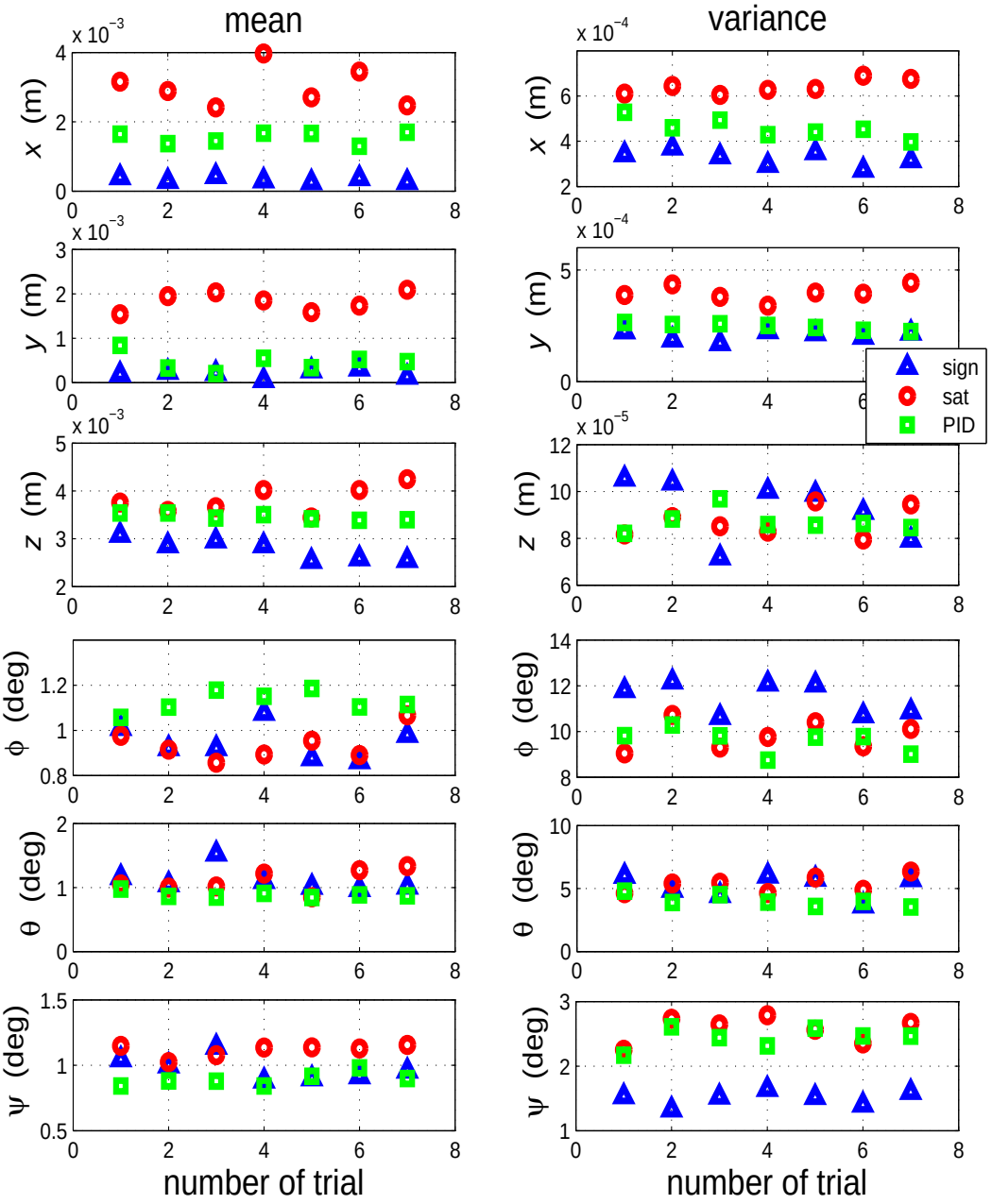

FIGURE 4.16: RSME and error variance for multiple times experiments for controllers C4, C5, and C6 without disturbance.

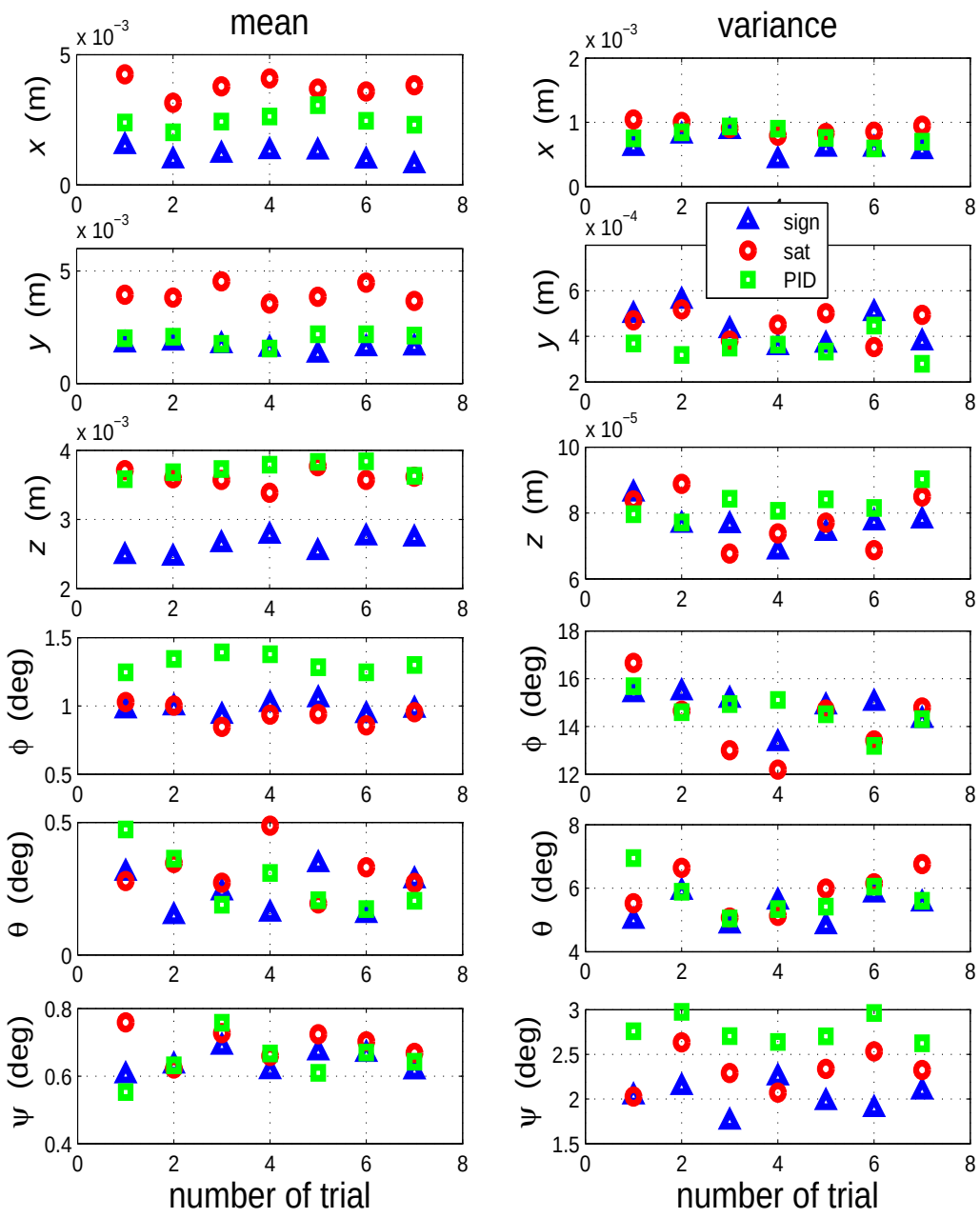

FIGURE 4.17: RSME and error variance for multiple times experiments for controllers C4, C5, and C6 under wind disturbance.

4.4.2 Power and Energy Evaluation

The electric DC motors utilized in the quadcopter experimental testbed are assumed to be identical resistance loads, therefore the power consumption of each motor during flight can be estimated by applying Eq. (2.21). The power consumption profiles for each motor during trajectory tracking are shown in Figs. 4.18 and 4.19. Power of each motor is calculated from control inputs u_1, u_2, u_3, and u_4 which are obtained in the experiments, together with their description in Chapter 2, and apply to Eqs. (2.20) and (2.21).

The chatter of control input causes corresponding chatter in the profiles of the power consumed by the motors as shown in Figs. 4.18 and 4.19. The sat(.) function reduces the chattering effect for both sliding surface functions in the conditions without/under wind disturbance. The total energy consumed in each motor is calculated by integrating the power during the flight. By conducting several times experiments, the chattering effect on the energy consumption is evaluated, and the results are given in Fig. 4.20. It is apparent that the sat(.) function contributes to reduce the energy consumption during the flight. In the experiments for the PD-based sliding surface function in Eq. (4.3) without wind disturbance, the controller C2 consumes less energy compared to the controllers C1 and C3, as shown in Fig. 4.20 (a). On average, controller C2 consumes energy approximately 2.25% less than C1 and 1.97% less than C3. While in condition under wind disturbance in Fig. 4.20 (b), on average, controller C2 consumes energy approximately 1.61% less than C1 and 1.75% less than C3. If we apply the PID-based sliding surface in Eq. (4.4), the sat(.) function is also effective to reduce the energy consumption, as shown in Fig. 4.20 (c) and (d). In condition without wind disturbance, on average, controller C5 consumes energy approximately 1.48% less than C4 and 1.59% less than C6. while in condition under wind disturbance, on average, controller C5 consumes energy approximately 2.18% less than C4 and 3.82% less than C6.

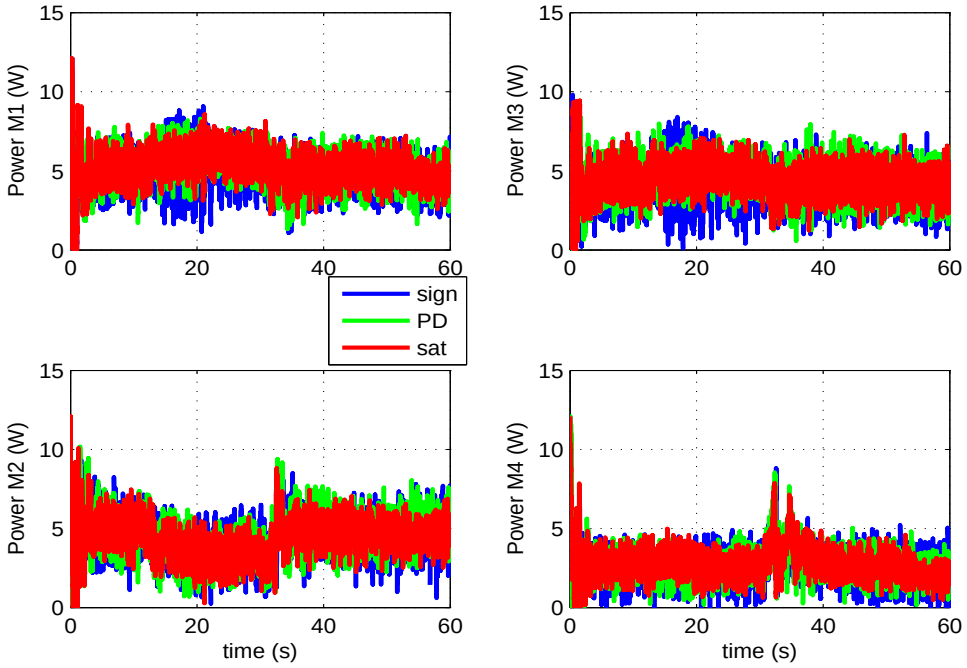

(a)

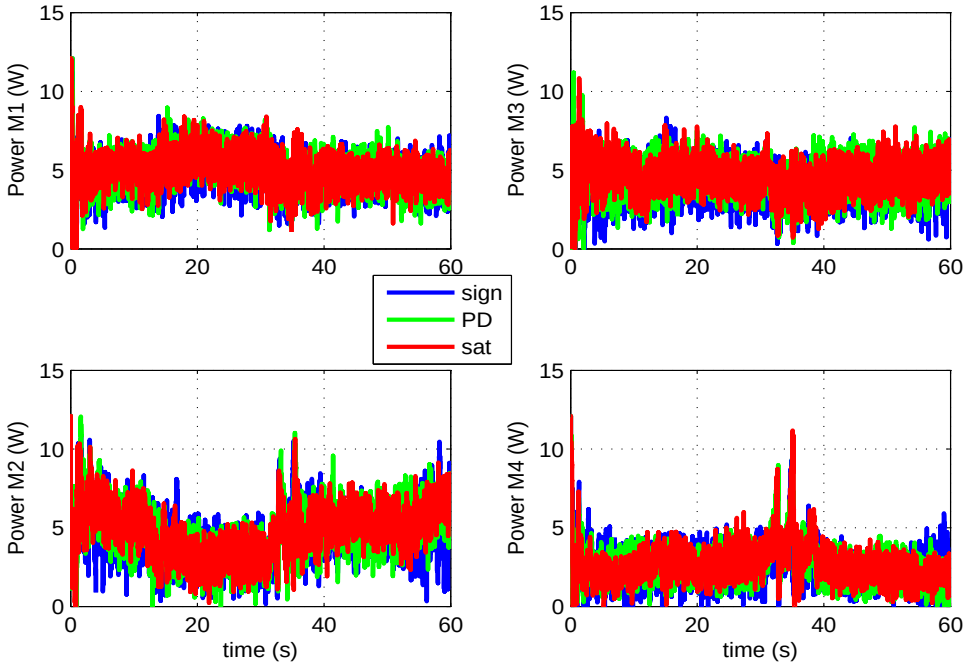

(b)

FIGURE 4.18: Profiles of power on each motor for controllers C1, C2, and C3 (a) without disturbance, (b) under wind disturbance.

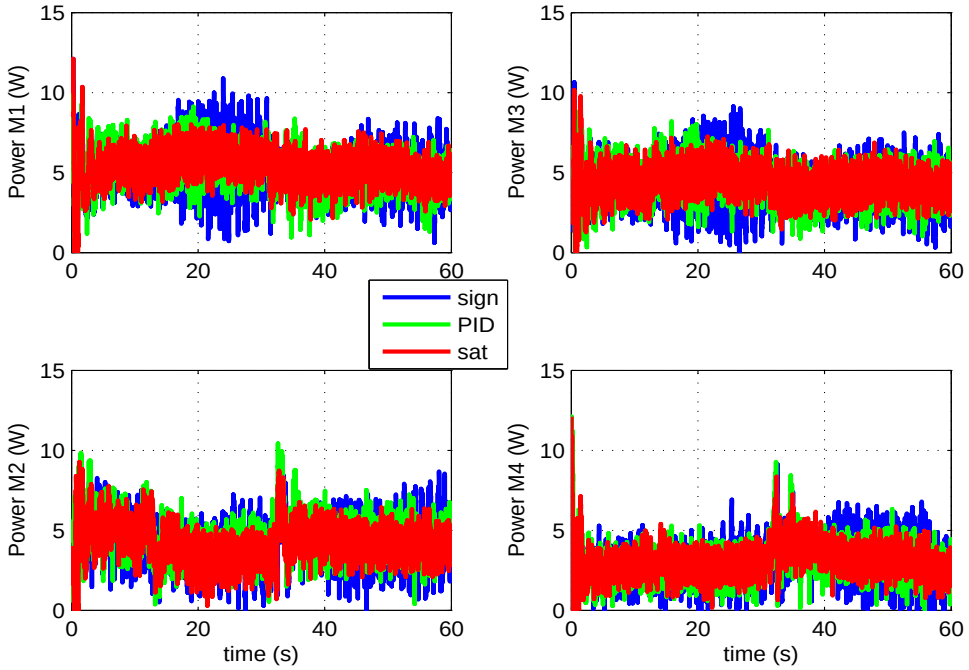

(a)

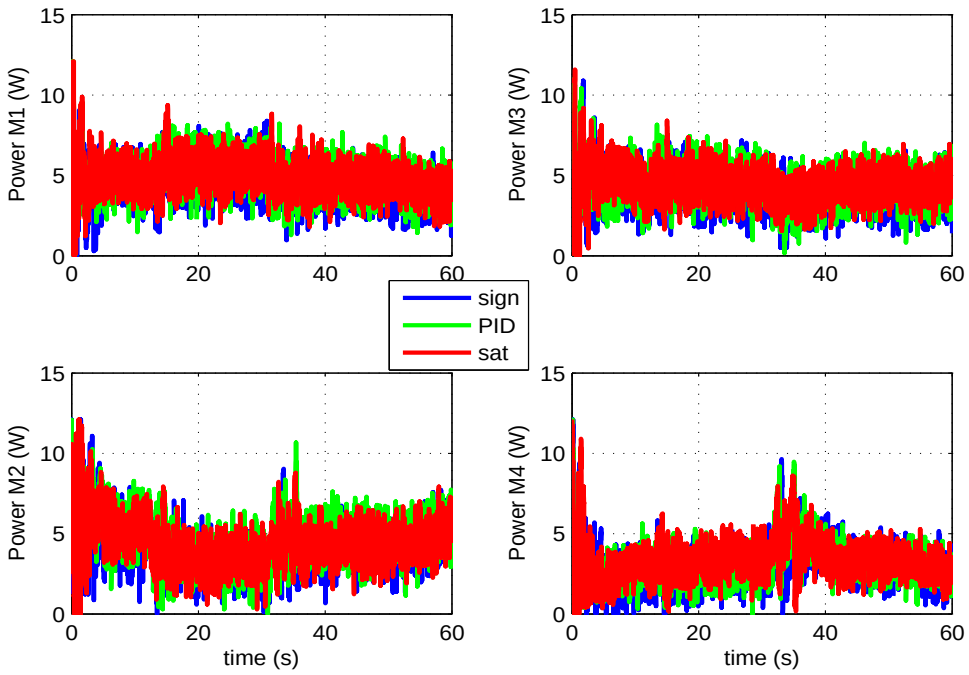

(b)

FIGURE 4.19: Profiles of power on each motor for controllers C4, C5, and C6 (a) without disturbance, (b) under wind disturbance.

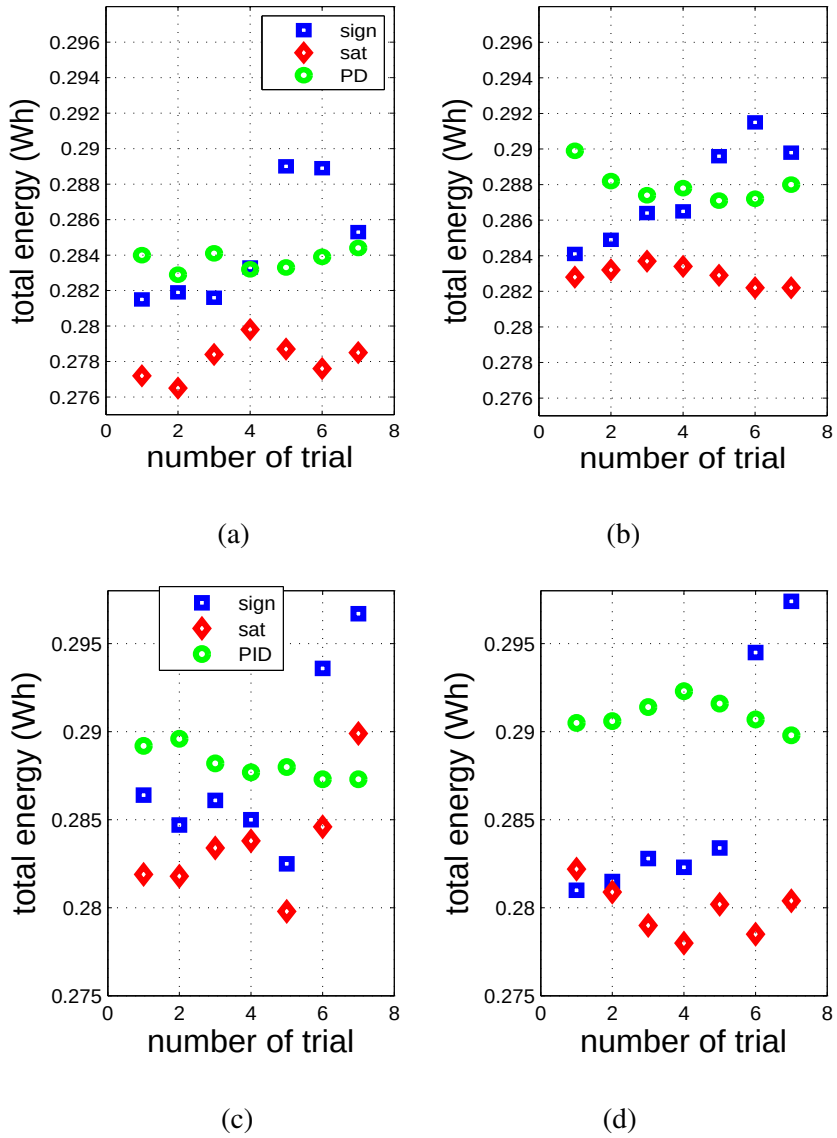

FIGURE 4.20: Total energy consumption of the motors; (a) controllers C1, C2, and C3 without disturbance; (b) controllers C1, C2, and C3 under wind disturbance; (c) controllers C4, C5, and C6 without disturbance; (d) controllers C4, C5, and C6 under wind disturbance.

4.5 Conclusion

In this chapter, SMC strategy that utilizes a PD-based sliding surface and a PID-based sliding surface are presented for stabilizing and tracking controller of a quadcopter. An energy reduction on SMC design is performed by reducing the chattering phenomenon. A boundary layer method is applied in reducing the chattering phenomenon and is effective to reduce the energy consumption of a quadcopter which is confirmed experimentally using a quadcopter testbed.

However, the boundary layer method that replaces the discontinuous control input in SMC strategy with a continuous control input reduces the robustness of the controller. Therefore, it is important to design other controller that provides both robustness and energy efficient.

Chapter 5

Robust Tracking Control of a Quad-Rotor Helicopter Utilizing Sliding Mode Control with a Nonlinear Sliding Surface

5.1 Introduction

In SMC strategy, behavior of the system in the sliding mode condition and overall closed-loop dynamics depend on the design of the sliding surface function. In this chapter, the sliding surface is proposed with the nonlinear function. We design two nonlinear functions with different characteristics. The first nonlinear sliding surface (NSS-1) is designed to improve the time-constant within the sliding mode condition as a function of error [86]. If error increases, the time-constant is reduced and if error decreases convergence to zero, the time-constant increases convergence to a constant number. The second nonlinear sliding surface (NSS-2) is designed in contrarily characteristic with NSS-1 [55]. The large error increases the time-constant convergence to a maximum value and by decreasing of error, the time-constant is reduced and converges to a minimum value. Therefore, with a minimum time-constant in the smallest error, the system responds quickly from the first time error occurs. By varying the time-constant, the tracking performance is improved. In addition, the energy consumption during the control operation is also reduced. The Lyapunov stability theory is utilized to prove the stability of these proposed strategies. The effectiveness of these strategies are experimentally evaluated using a quadcopter testbed in terms of robustness and energy efficiency by comparing with SMC strategy utilizing the linear sliding surface. This chapter is related to the works presented in [86].

5.2 Control System Design

Recalling the dynamics of the quadcopter given in Eq. (3.2) by considering the disturbance term as follows:

$$\begin{aligned} \dot{\xi}_1 &= \xi_2 \\ \dot{\xi}_2 &= v + \rho_d \end{aligned} \tag{5.1}$$

where $\xi_1 = [x, y, z, \phi, \theta, \psi]^T$ is the position, $\xi_2 = [\dot{x}, \dot{y}, \dot{z}, \dot{\phi}, \dot{\theta}, \dot{\psi}]^T$ is the velocity, $v = [v_x, v_y, v_z, v_\phi, v_\theta, v_\psi]^T$ is the synthetic input, and ρ_d is the disturbance vector. An SMC strategy with a nonlinear sliding surface is designed for the synthetic input v.

5.2.1 Nonlinear Sliding Surface Design

In order to improve the performance of the system during the sliding mode condition, we design a nonlinear sliding surface (NSS) as follows:

$$s = [F - \Psi \qquad I][e_1 \qquad e_2]^T \tag{5.2}$$

where s is the sliding surface vector, $F = \text{diag}\{F_i\} \in \Re^{6\times 6}$ is a positive diagonal matrix, I is a 6×6 identity matrix, e_1 and e_2 are tracking error vectors of ξ_1 and ξ_2 to the desired trajectories $\xi_{1d} = [x_d, y_d, z_d, \phi_d, \theta_d, \psi_d]^T$ and $\xi_{2d} = [\dot{x}_d, \dot{y}_d, \dot{z}_d, \dot{\phi}_d, \dot{\theta}_d, \dot{\psi}_d]^T$, respectively. $\Psi = \text{diag}\{\Psi_i\}$, $i = 1, 2, \ldots, 6$, consists of two different nonlinear function for NSS-1 and NSS-2. The NSS-1 is designed with the following nonlinear function:

$$\Psi_i = -\beta_i \frac{\exp(c|\varepsilon_i|) - 1}{\exp(|\varepsilon_i|)}, \qquad \varepsilon_i \in e_1, \tag{5.3}$$

and NSS-2 is designed with the following nonlinear function:

$$\Psi_i = -\beta_i \left(\frac{1 - \exp(-1)}{\exp(\varepsilon_i^2) - \exp(-1)} \right), \qquad \varepsilon_i \in e_1, \tag{5.4}$$

where $\beta_i > 0$ and $c > 1$. The nonlinear function in Eq. (5.3) increases "$-\Psi_i$" if error is increased, and therefore the time-constant of sliding function in Eq. (5.2) is decreased. If error decreases convergence to zero then "$-\Psi_i$" is decreased convergence to zero. Hence, the time-constant of sliding function in Eq. (5.2) increases convergence to a constant value, F_i^{-1}.

Conversely, the NSS-2 provides a contrarily characteristic on the sliding surface function. If $\varepsilon_i \to \infty$, $\Psi_i \to 0$ therefore the time-constant of sliding function in Eq. (5.2) converges to F_i^{-1}, which is the maximum value. If $\varepsilon_i \to 0$, $\Psi_i \to -\beta_i$, and hence the time-constant of sliding function in Eq. (5.2) goes to the minimum value, $(F_i + \beta_i)^{-1}$. Characteristic of these nonlinear sliding surface functions and the linear sliding surface function (LSS) are illustrated in Fig. 5.1.

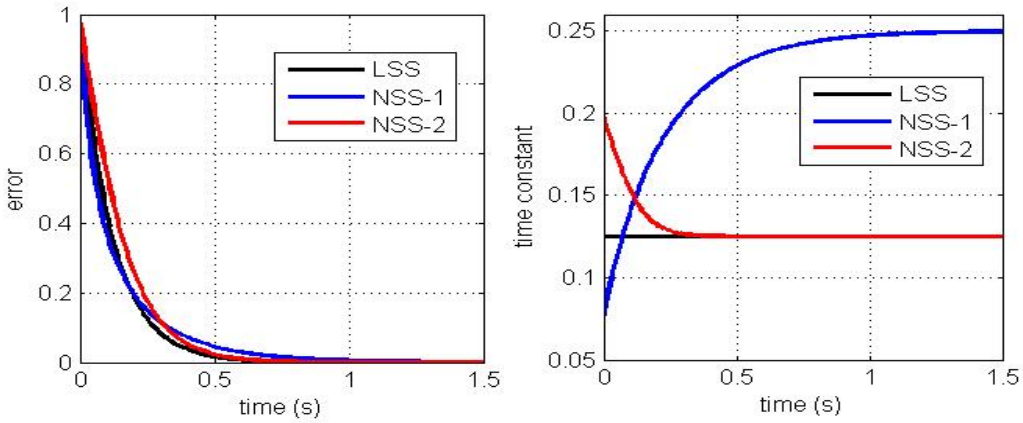

FIGURE 5.1: Characteristic of LSS, NSS-1, and NSS-2.

These two nonlinear functions also provide different profiles of the sliding surface as function of tracking error as shown in Fig. 5.2. It is seen that the NSS-1 and NSS-2 provide a nonlinear behaviour while the LSS provides a linear one.

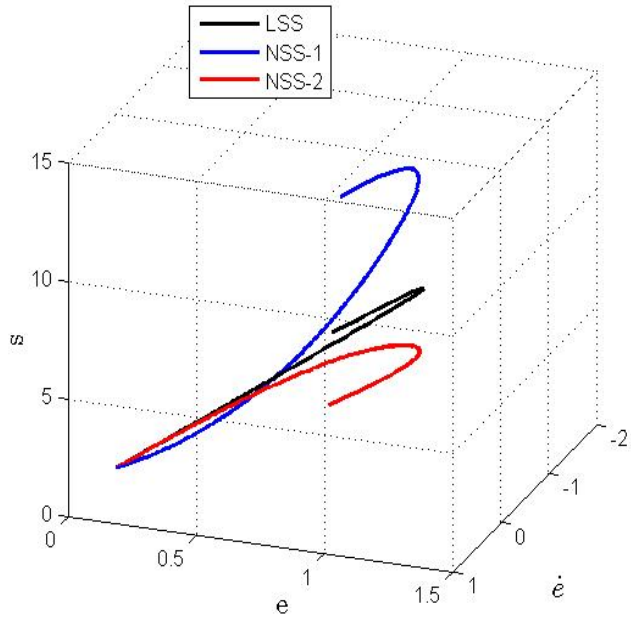

FIGURE 5.2: Profiles of sliding surface functions for LSS, NSS-1, and NSS-2.

These two nonlinear functions provide $\Psi_i \leq 0$ therefore the sliding surface function in Eq. (5.2) is a stable function. Stability of this sliding surface function is described as follows.

The sliding mode condition is achieved when $s = 0$, and therefore we have the following dynamics:

$$e_2 = -(F - \Psi)e_1 \tag{5.5}$$

where $e_2 = \dot{e_1}$. Let us consider candidate of the Lyapunov function for dynamics in Eq. (5.5) as follows:

$$V = \frac{1}{2} e_1^T e_1 \tag{5.6}$$

Taking the first derivative of Lyapunov function in Eq. (5.6) by considering Eq. (5.5), we have

$$\dot{V} = -e_1^T (F - \Psi) e_1 \tag{5.7}$$

Because $(F - \Psi) > 0$ then $\dot{V}$ is negative definite and hence the sliding surface in Eq. (5.2) is stable.

5.2.2 Controller Design Via Lyapunov Stability Analysis

The sliding mode condition is achieved by designing a control law for the dynamics in Eq. (5.1). Let us consider a candidate of the Lyapunov function for the system in Eq. (5.1) as follows:

$$V = \frac{1}{2} s^T s \tag{5.8}$$

Differentiating Eq. (5.8), we have

$$\dot{V} = s^T \dot{s} \tag{5.9}$$

Considering the differentiation of Eq. (5.2) and substituting it into Eq. (5.9), we have

$$\dot{V} = s^T (\dot{e}_2 + (F - \Psi)\dot{e}_1 - \dot{\Psi} e_1) \tag{5.10}$$

$\dot{\Psi} = \text{diag}\{\dot{\Psi}_i\}$ is the time derivative of Ψ which consists of

$$\dot{\Psi}_i = -\dot{\varepsilon}_i \text{sign}(\varepsilon_i) \left(\beta_i c \frac{\exp(c|\varepsilon_i|)}{\exp(|\varepsilon_i|)} + \Psi_i \right), \qquad \dot{\varepsilon}_i \in e_2 \tag{5.11}$$

for NSS-1, and for NSS-2 is as follows:

$$\begin{aligned} \dot{\Psi}_i =& \Psi_i' \dot{\varepsilon}_i, \ \dot{\varepsilon}_i \in e_2 \\ \Psi_i' =& -2\Psi_i \frac{\varepsilon_i \exp(\varepsilon_i^2)}{\exp(\varepsilon_i^2) - \exp(-1)} \end{aligned} \tag{5.12}$$

The tracking errors of the system in Eq. (5.1) to the desired trajectories ξ_{1d} and ξ_{2d} are defined as follows:

$$\begin{aligned} e_1 =& \xi_1 - \xi_{1d} \\ e_2 =& \xi_2 - \xi_{2d} \end{aligned} \tag{5.13}$$

Differentiating Eq. (5.13) and substituting it into Eq. (5.10) together with the dynamics in Eq. (5.1), the time derivative of the Lyapunov function candidate can be written as

$$\dot{V} = s^T((F-\Psi)\dot{e}_1 - \dot{\Psi}e_1 + v + \rho_d - \dot{\xi}_{2d}) \tag{5.14}$$

We consider the control input v as follows:

$$v = -(F-\Psi)\dot{e}_1 + \dot{\Psi}e_1 - Ks - Q\,\mathrm{sign}(s) + \dot{\xi}_{2d}) \tag{5.15}$$

where $K = \mathrm{diag}\{K_i\} \in \Re^{6\times 6}$ and $Q = \mathrm{diag}\{Q_i\} \in \Re^{6\times 6}$ are positive definite matrices. Substituting Eq. (5.15) into Eq. (5.14), we obtain

$$\dot{V} = s^T(-Ks - Q\,\mathrm{sign}(s) + \rho_d) \tag{5.16}$$

If $Q_i > |\rho_{di}|$, $\rho_{di} \in \rho_d$, then $\dot{V}$ is negative definite, and hence the system in Eq. (5.1) is stabilized by the control input in Eq. (5.15). If $|\rho_{di}|$ is known, the control designers can assign the value of Q_i in advance in controller design. If knowing $|\rho_{di}|$ is difficult, the control designers have to assign the value of Q_i conservatively.

Considering the control input v in Eq. (5.15) with the sliding surface in Eq. (5.2), and substituting to the dynamics in Eq. (5.1), we have the closed loop dynamic of the control system as follows:

$$\ddot{e}_1 + (K+F-\Psi)\dot{e}_1 + (K(F-\Psi) - \dot{\Psi})e_1 + Q\,\mathrm{sign}(s) - \rho_d = 0 \tag{5.17}$$

Considering the linear terms of Eq. (5.17), the varying of Ψ and $\dot{\Psi}$ cause the closed loop properties of the system, damping ratio and natural frequency, to be varying depend on the tracking error. Profile of damping ratio and natural frequency for the NSS-1 and NSS-2 together compared with the linear sliding surface (LSS) are illustrated in Fig. 5.3. It is seen that the NSS-1 and NSS-2 have varying damping ratio (ζ_r) and natural frequency (ω_n) while LSS provides fix value, and hence converging characteristic of errors position and velocity are different. The system with high ω_n or low ζ_r provides faster response but consume more energy than the system with low ω_n or high ζ_r. Therefore by varying the ω_n and ζ_r, the advantages of having low and high ω_n and ζ_r can be obtained.

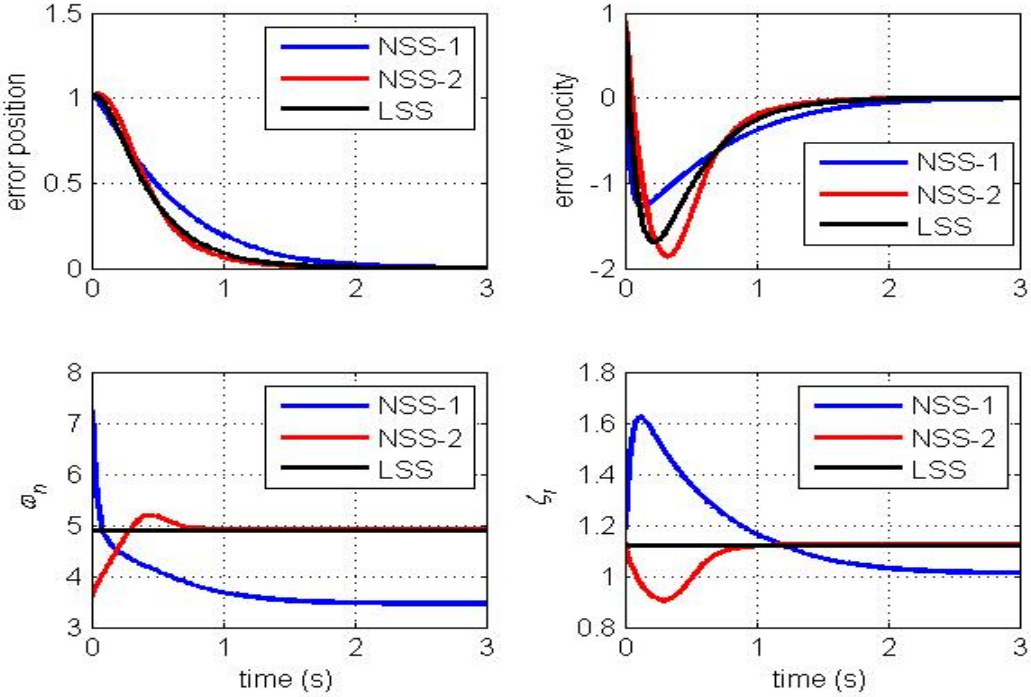

FIGURE 5.3: Profiles of damping ratio and natural frequency for SMC with NSS-1, NSS-2, and LSS.

5.3 Experimental Results

In order to evaluate the effectiveness of the proposed control strategies, we perform experiments using the experimental quadcopter testbed shown in Fig. 2.2. The desired trajectory is designed similar to the trajectory given in the previous chapter in Fig. 4.1. The gain parameters of control input in Eq. (5.15) are tuned to achieve the best experimental results, and are obtained as follows (unit are omitted):

- For NSS-1:

$$
\begin{aligned}
c &= 2 \\
K &= \mathrm{diag}\{3,3,12,12,12,80\} \\
Q &= \mathrm{diag}\{0.1,0.1,0.3,0.2,0.3,0.5\} \\
F &= \mathrm{diag}\{8,9,9,13,14,90\} \\
\beta &= [14,13,30,20,20,200]^T
\end{aligned}
$$

- For NSS-2:

$$\begin{aligned} K =& \text{diag}\{3,3,8,10,9,80\} \\ Q =& \text{diag}\{0.1,0.1,0.3,0.2,0.3,0.5\} \\ F =& \text{diag}\{3,3,8,9,10,50\} \\ \beta =& [5,6,10,12,12,60]^T \end{aligned}$$

where $\beta = [\beta_1, \ldots, \beta_6]^T$. For the comparison purpose, we utilize the linear sliding surface (LSS) equation given in Eq. (4.3) together with the control input in Eq. (4.8). To provide fair comparison, we chose $q = Q$ and tune the other parameters to achieve the best experimental results, and are given as follows:

$$\begin{aligned} k =& \text{diag}\{4.5,4,12,18,20,100\} \\ q =& \text{diag}\{0.1,0.1,0.3,0.2,0.3,0.5\} \\ \lambda =& \text{diag}\{6,7,10,10,10,70\} \end{aligned}$$

Trough the experiments, we evaluate the effectiveness of the proposed strategies in terms of robustness and energy saving.

5.3.1 Robustness Evaluation

By applying the gain parameters given in the previous subsection to track the desired trajectory in Fig. 4.1 in condition without disturbance, we obtain a tracking trajectory results for both sliding mode controllers with nonlinear sliding surface (NSS-1 and NSS-2) and LSS as shown in Fig. 5.4. The tracking error in Fig. 5.5 shows that the SMC strategy with NSS provides better performance compared to that with LSS, especially in maneuver motion, while in stabilization (constant position) both control strategies provide similar error tracking. Furthermore, in maneuver motion, the sliding mode control with NSS-1 provides better performance compared to those with NSS-2 and LSS. It can also be confirmed by performing several times experiments as shown in Fig. 5.8 that on average the NSS-1 produces relatively smaller variance of error. Robustness of the proposed strategies is evaluated by applying a wind disturbance, and the results are shown in Figs. 5.6 and 5.7. It is seen that the SMC strategy with NSS provides more robustness by producing smaller chatter in the tracking error as shown in Fig. 5.7. The NSS-1 performs better in maneuver motion compared to those with NSS-2 and LSS as shown in Fig. 5.7. However, on average the NSS-2 provides better performance in condition under disturbance by producing relatively smaller root-squared mean error (RSME) and/or error variance as shown in Fig. 5.9. Results of these multiple times experiments are summarized in Tables 5.1 and 5.2

TABLE 5.1: Average of root-squared of mean error (RSME) and error variance (Var) for experiments without disturbance.

	Translational motion		Rotational motion	
	RSME (mm)	Var (mm)	RSME (deg)	Var (deg)
SMC with LSS	10.191	1.232	0.281	2.546
SMC with NSS-1	11.249	1.395	0.241	2.341
SMC with NSS-2	11.211	1.167	0.282	3.142

TABLE 5.2: Average of root-squared of mean error (RSME) and error variance (Var) for experiments under wind disturbance.

	Translational motion		Rotational motion	
	RSME (mm)	Var (mm)	RSME (deg)	Var (deg)
SMC with LSS	17.853	1.436	0.509	5.859
SMC with NSS-1	15.247	1.380	0.347	4.691
SMC with NSS-2	14.877	1.071	0.444	3.893

Profiles of the control inputs in both experiment's conditions without and under wind disturbance are shown in Figs. 5.10 and 5.11. It is seen that the SMC strategy with LSS produces higher oscillation especially for inputs u_2 and u_3 in the experiment under wind disturbance for maneuver motion as shown in Fig. 5.11.

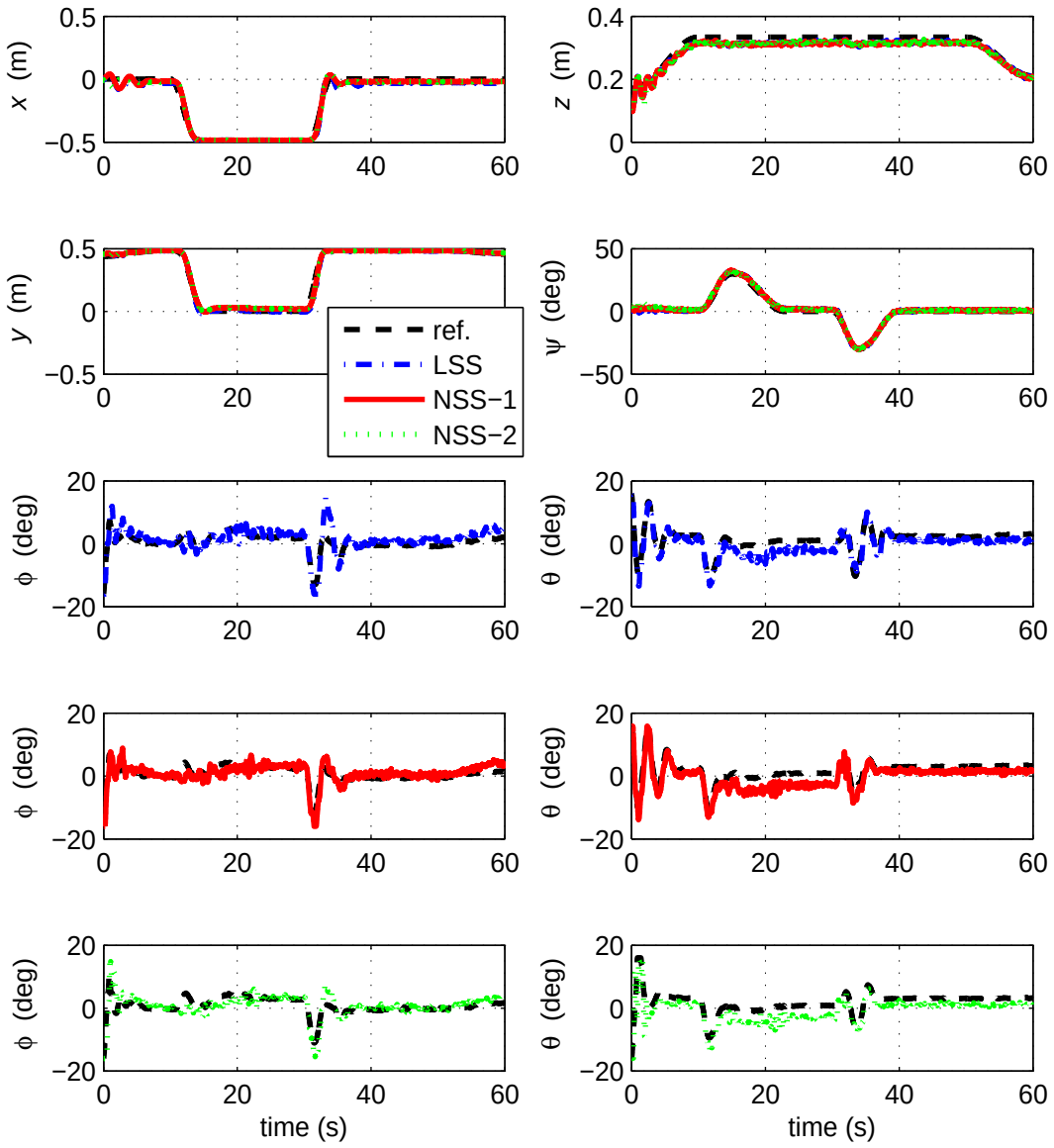

FIGURE 5.4: Trajectory tracking without disturbance

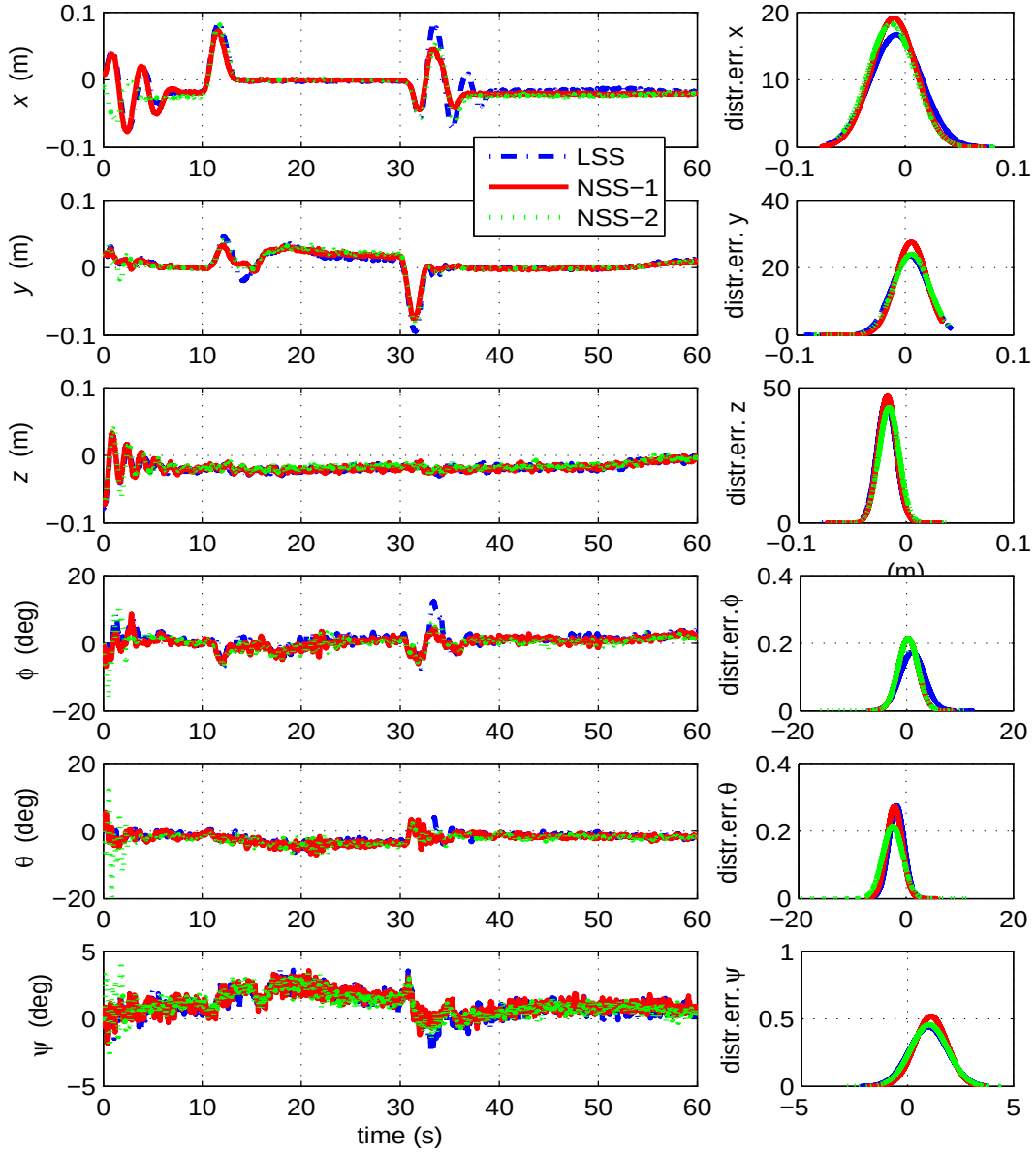

FIGURE 5.5: Tracking error without disturbance

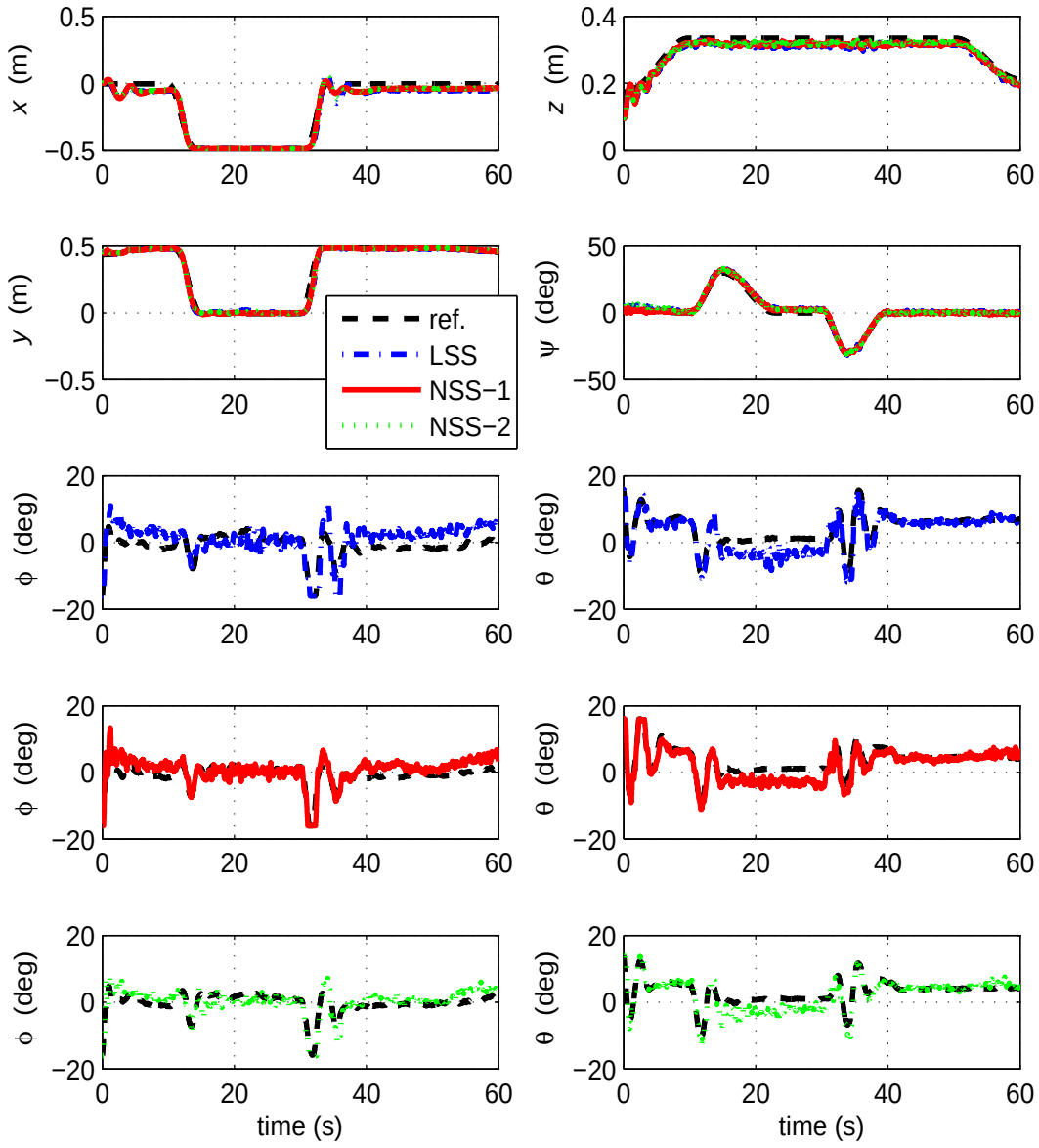

FIGURE 5.6: Trajectory tracking under wind disturbance

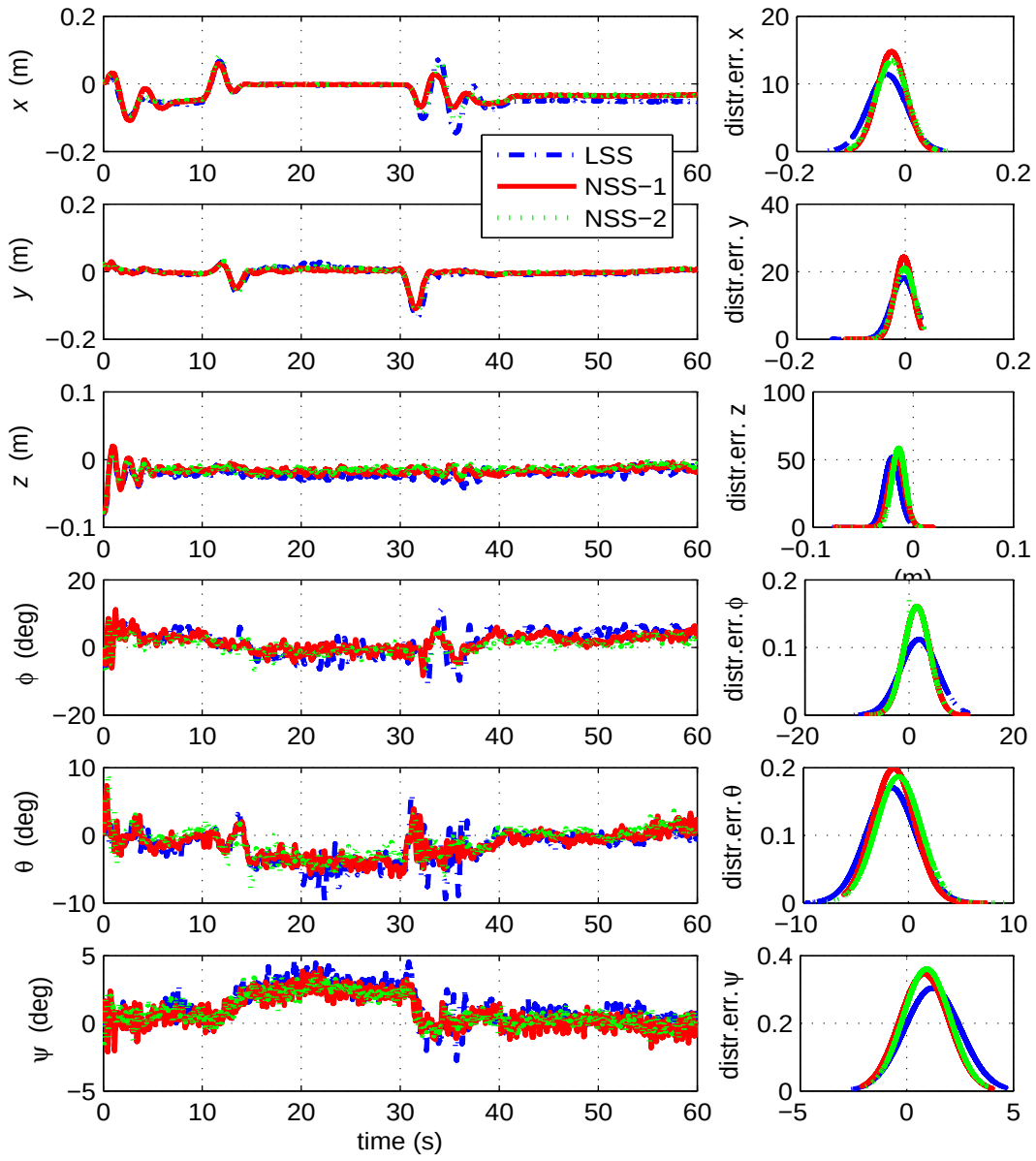

FIGURE 5.7: Tracking error under wind disturbance

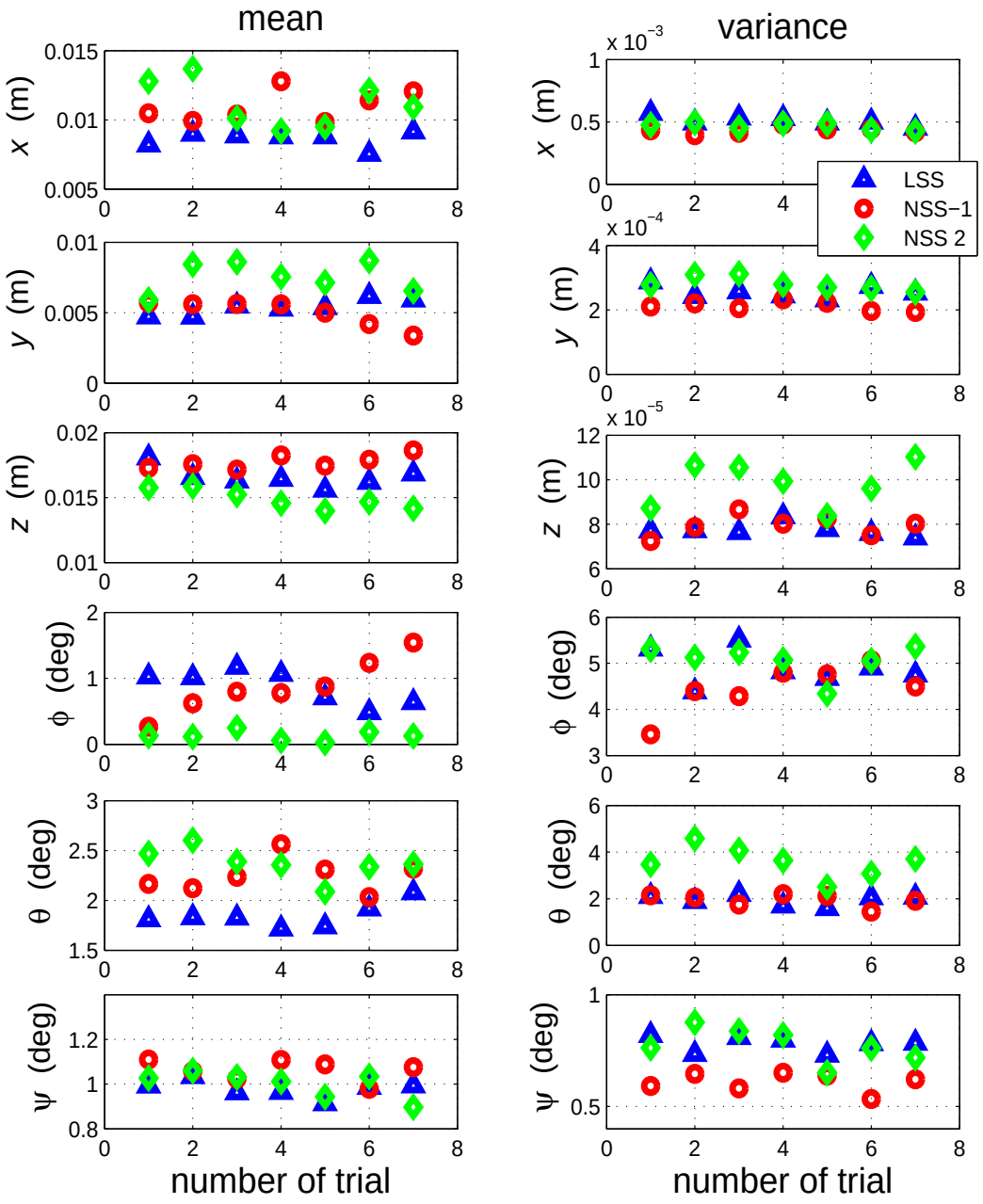

FIGURE 5.8: RSME and error variance in several times experiments without disturbance

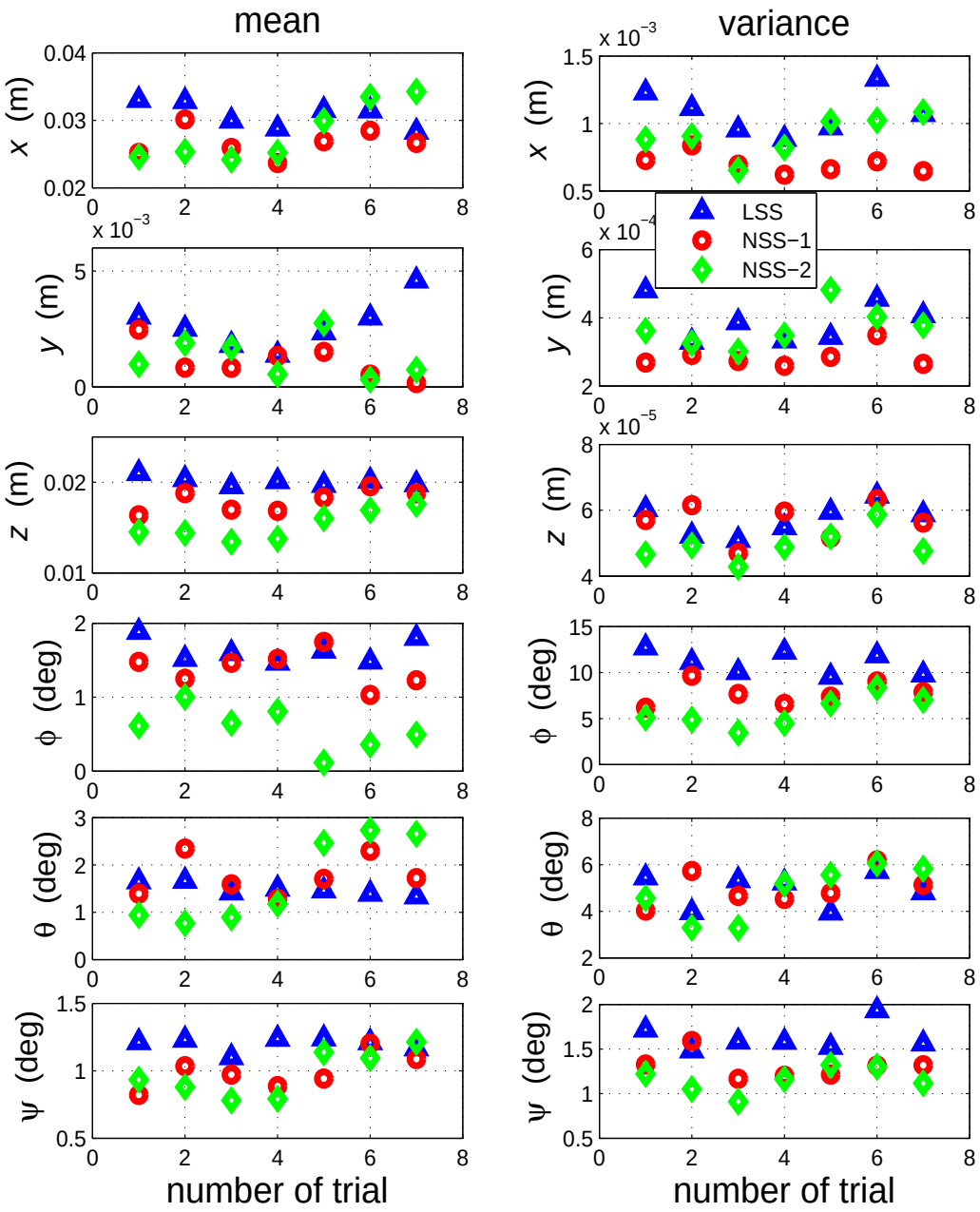

FIGURE 5.9: RSME and error variance in several times experiments under wind disturbance

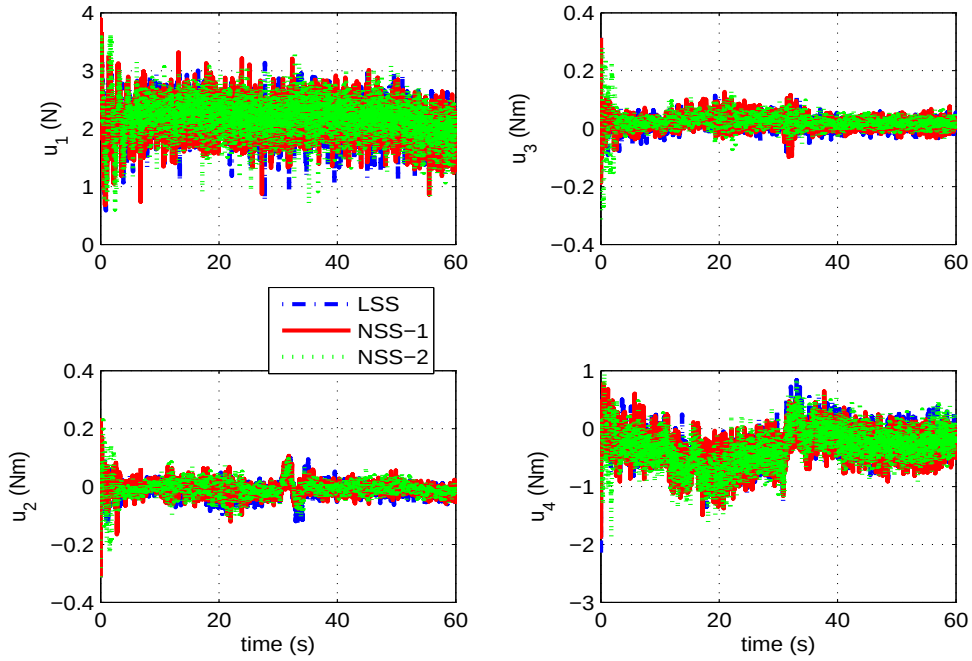

FIGURE 5.10: Profiles of control inputs in the experiment without disturbance

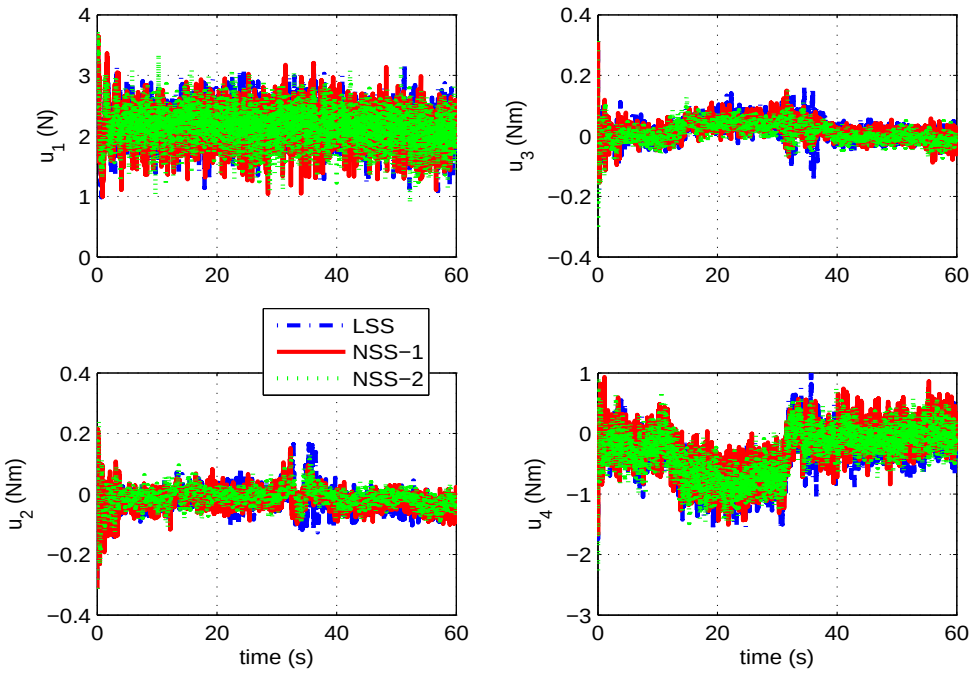

FIGURE 5.11: Profiles of control inputs in the experiment under wind disturbance

5.3.2 Power and Energy Evaluation

The electric power consumed on each actuator in the experiments without and under wind disturbance are shown in Figs. 5.12 and 5.13. The total energy consumed on each actuator is calculated by integrating the power during the control operation. Total energy consumed by all actuators for several times experiments in the conditions without and under wind disturbance are shown in Fig. 5.14. It is seen that the SMC strategy with NSS consumes less energy in condition under disturbance while that with LSS is efficient in condition without disturbance. In experiments without disturbance, the average energy consumption for the SMC strategy with LSS is about 274.78 mWh, NSS-1 is bout 278.455 mWh, and NSS-2 is about 277.261 mWh. While in experiments under wind disturbance, on average, the energy consumption for LSS is about 285.57 mWh, NSS-1 is about 280.071 mWh, and NSS-2 is about 278.718 mWh.

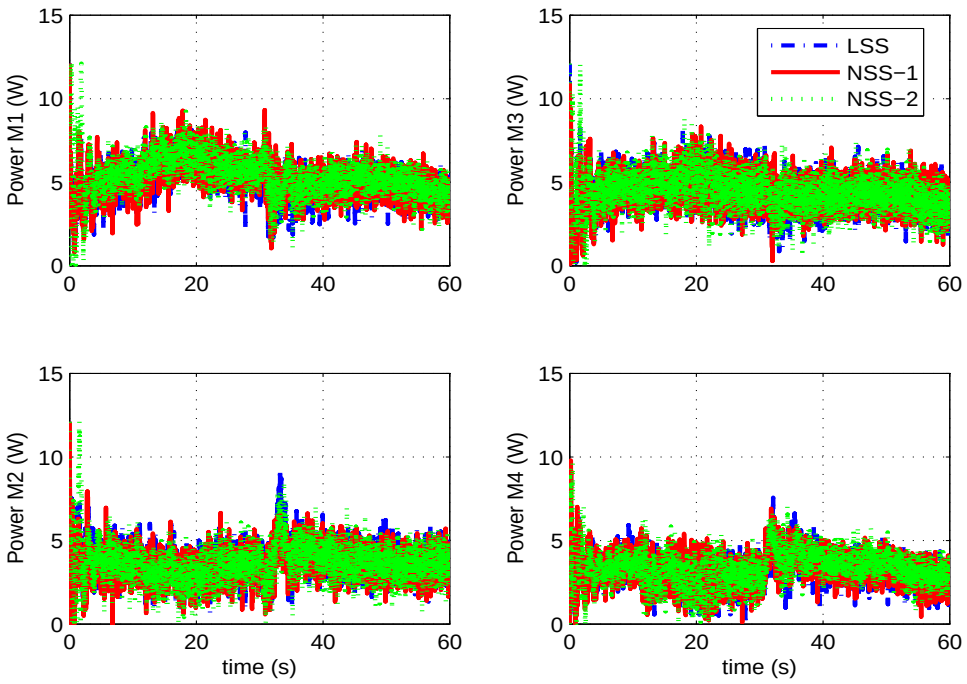

FIGURE 5.12: Profiles of power on each motor in the experiment without disturbance

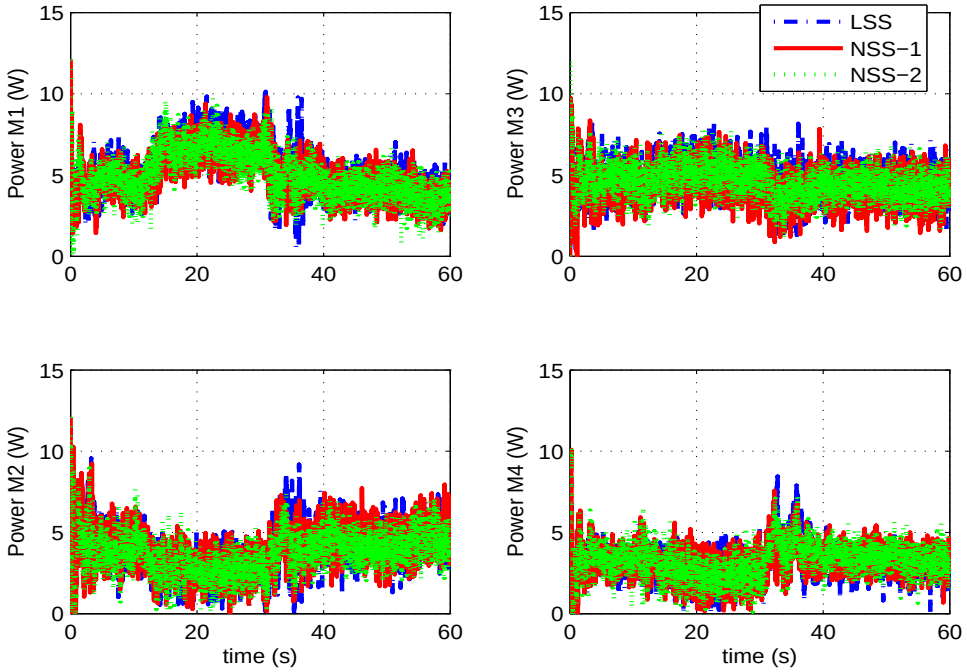

FIGURE 5.13: Profile of power on each motor in the experiment under wind disturbance

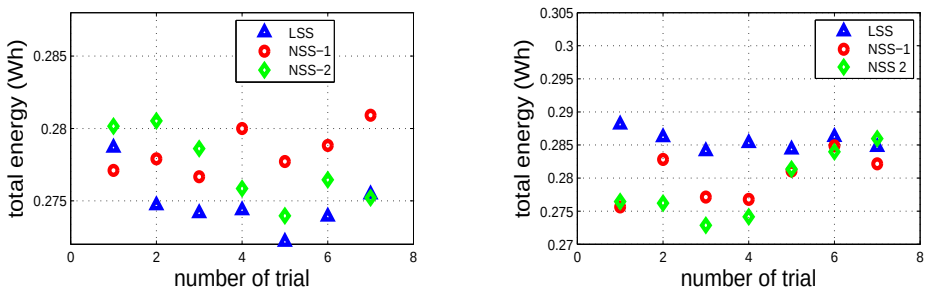

(a) (b)

FIGURE 5.14: Total energy consumed by the actuators in several times experiments: (a) without disturbance; (b) under wind disturbance.

5.4 Conclusion

In this chapter, we design two nonlinear sliding surfaces to make a varying time-constant in sliding mode condition for an SMC strategy of a quadcopter. These nonlinear sliding functions have different characteristics and both are designed as a function of tracking error. The first sliding function (NSS-1) reduces the time-constant if error increases, and therefore the system responds faster to reduce the error. If error is reduced going to zero then the time-constant is increased goes to a constant value. The second sliding function (NSS-2) is designed in a

contrarily characteristic with NSS-1. The NSS-2 increases the time-constant goes to a maximum value if error is increased goes to infinity. If error is reduced convergence to zero, the time-constant reduces convergence to a minimum value. Therefore, the NSS-2 responds faster in a small tracking error. The stability of these strategies are guaranteed in the sense of Lyapunov stability theory. Effectiveness of the proposed strategies are experimentally evaluated using an experimental quadcopter testbed. From the characteristic of the two sliding functions, the SMC strategy with NSS-1 is effective for a maneuver motion and that with NSS-2 is effective in stabilization. This is also confirmed by experimental results. The nonlinear sliding surface is also effective to reduce the energy consumption especially in the experiments condition under wind disturbance. Therefore, it is appropriate for an outdoor application where the quadcopter is influenced by unknown disturbance.

Chapter 6

A Nonlinear Sliding Surface for the Second-Order Sliding Mode Control

6.1 Introduction

In some applications of a quadcopter, robust tracking performance is needed against dynamics uncertainty and unpredictable disturbance such as wind gust. SMC strategy is a well known robust controller which has invariant characteristics in the sliding mode condition, and has been applied in the quadcopter [4, 7, 8, 14, 21, 24, 43, 44, 48–51, 53, 54, 60, 86]. The invariant characteristics of SMC strategy is generated by the switching function in the control design which produces chattering phenomenon.

Practically, this chatter should be avoided or at least reduced because it can harms the actuator. In Chapter 4, the chatter reduction is addressed by designing a boundary layer near the sliding surface. Unfortunately, this method does not guarantee the invariant property. The second-order sliding mode control becomes a good alternative solution to reduce the chatter because it ensures the invariant property of the SMC strategy [78, 89, 90]. This method shifts the switching function which is the source of chatter into the second-order time-derivative of the sliding surface while in the standard SMC the switching function is in the first-order. Among the designs of the second-order SMC, the super-twisting algorithm (STA) is a reasonable choice because it needs only the information of sliding surface [78], and has been applied in a quadcopter [10, 53, 54]. In practical, it is arduous to choose appropriate control parameters of STA to obtain a good performance because the classical STA has a strong behavior only against the disturbance around the origin (zero state) but it is weak at states far from the origin [80]. Moreno and Osorio proposed a generalized-STA (GSTA) to improve this weakness [79]. The GSTA includes a linear stabilizing term which has a strong behavior when the state is far from the origin, and provides robustness in both conditions, far and around the origin.

In the SMC strategy, the closed-loop dynamics depends on the design of the sliding surface. In order to improve the performance of the SMC, a time-varying sliding surface is considered previously in Chapter 5. Two nonlinear sliding surfaces, NSS-1 and NSS-2, those provide different characteristics in the sliding mode condition are presented. On average, in condition under disturbance, the NSS-2 provides better performance then NSS-1 by resulting smaller root-squared mean error and consuming less energy. In this chapter, the time-varying sliding surface with NSS-2 is applied for the second-order SMC [55, 91]. The GSTA-SMC is utilized for the robust tracking control of a quadcopter. The new nonlinear sliding surface equation as a function of tracking error is introduced to reduced the energy consumption through designing a time varying properties of the closed-loop dynamics (damping ratio and natural frequency). The GSTA-SMC method is utilized to provide a robustness before and during the sliding mode. Stability of the proposed method in and out of sliding mode is proved by the Lyapunov stability theory. The effectiveness and reliability of the proposed method are evaluated in several times experiments with a quadcopter experimental testbed. This chapter is related to the works presented in [91]

6.2 Development of Control System

Recalling the dynamics of a quadcopter in Eq. (3.2) by including a disturbance vector γ_d, and rewrite in a simple form as follows:

$$\begin{aligned} \dot{\eta}_1 &= \eta_2 \\ \dot{\eta}_2 &= v + \gamma_d \end{aligned} \tag{6.1}$$

where $\eta_1 = \xi = [x, y, z, \phi, \theta, \psi]^T$ and $\eta_2 = \dot{\xi}$. $v = [v_x, v_y, v_z, v_\phi, v_\theta, v_\psi]^T$ is the synthetic input which is designed by using the second-order sliding mode control strategy. In the second-order SMC strategy, the sliding mode condition is characterized as follows in [92]

$$s = \dot{s} = 0 \tag{6.2}$$

where s and $\dot{s}$ are the sliding surface and its first derivative, respectively. Furthermore, the robustness which is provided by invariant characteristic occurs in this condition. The switching function as the source of invariance appears in the second derivative of s. A nonlinear sliding surface is utilized to improve the performance of the closed-loop control system.

6.2.1 Sliding Surface Equation

By letting $e = \eta_1 - \eta_{1d}$ be the tracking error, where η_{1d} is the desired trajectory for ξ, in the standard SMC, the sliding surface of a second-order system in Eq. (6.1) is designed as a linear

differential equation as follows [59]:

$$s = \text{diag}\left\{\left(\frac{d}{dt}+\lambda_1\right),\ldots,\left(\frac{d}{dt}+\lambda_6\right)\right\}e \tag{6.3}$$

where s is a vector of sliding surface in all DOF, and λ_i $(i = 1,\ldots,6)$ is a positive constant to guarantee the stability in the sliding mode. By denoting $\lambda = \text{diag}\{\lambda_1,\ldots,\lambda_6\}$, Eq. (6.3) can be rewritten as

$$s = \lambda e + \dot{e} \tag{6.4}$$

In this work, we change the positive constant matrix λ into a positive nonlinear function matrix such that the closed-loop properties of the system are changed from its original value as the output approaches the desired trajectory, named as a nonlinear sliding surface (NSS). The NSS for dynamics in Eq. (6.1) is designed as follows:

$$s = (F+\Psi)e + \dot{e} \tag{6.5}$$

where $F = \text{diag}(F_1,\ldots,F_6) \in \Re^{6\times 6}$ is a positive definite diagonal matrix and the matrix $\Psi = \text{diag}(\Psi_1,\ldots,\Psi_6) \in \Re^{6\times 6}$ consists of the following nonlinear functions:

$$\Psi_i = \beta_i\left(\frac{1-\exp(-1)}{\exp(\varepsilon_i^2)-\exp(-1)}\right),\ \varepsilon_i \in e \tag{6.6}$$

We choose $\beta_i > 0$ to guarantee $\Psi_i > 0$. Designing β_i is discussed later in the next section.

6.2.2 Stability of Sliding Surface

The switching function, which contributes to the invariant property, is shifted into the second-order. $\dot{s}$ is obtained by taking the first derivative of s in Eq. (6.5) as follows:

$$\dot{s} = (F+\Psi)\dot{e} + \dot{\Psi}e + \ddot{e}, \tag{6.7}$$

where $\ddot{e} = \dot{\eta}_2 - \dot{\eta}_{2d}$, $\dot{\eta}_{2d}$ is the desired acceleration vector, and $\dot{\Psi}$ is a 6×6 diagonal matrix whose elements consist of the first derivative of Eq. (6.5) as follows:

$$\begin{aligned}\dot{\Psi}_i =& \Psi_i'\dot{\varepsilon}_i,\ \dot{\varepsilon}_i \in \dot{e}\\ \Psi_i' =& -2\Psi_i\frac{\varepsilon_i\exp(\varepsilon_i^2)}{\exp(\varepsilon_i^2)-\exp(-1)},\ \varepsilon_i \in e\end{aligned} \tag{6.8}$$

Considering the sliding mode condition in Eq. (6.2) and applying to Eqs. (6.5) and (6.7), we have the following equations

$$\begin{aligned} \dot{e} &= -(F+\Psi)e \\ \ddot{e} &= -\dot{\Psi}e - (F+\Psi)\dot{e} \end{aligned} \tag{6.9}$$

Since F, Ψ, and $\dot{\Psi}$ are diagonal matrices, the stability of dynamics in Eq. (6.9) can be confirmed in each DOF independently. The Lyapunov function candidate in each DOF is given as follows:

$$V = \frac{1}{2}\varepsilon_i^2 + \frac{1}{2}\dot{\varepsilon}_i^2 \tag{6.10}$$

Taking the first derivative of Eq. (6.10) by considering Eqs. (6.8) and (6.9), we have

$$\dot{V} = -\left\{1 + (F_i+\Psi_i)^2 - \frac{2\Psi_i(F_i+\Psi_i)\varepsilon_i^2\exp(\varepsilon_i^2)}{\exp(\varepsilon_i^2)-\exp(-1)}\right\}(F_i+\Psi_i)\varepsilon_i^2 \tag{6.11}$$

Because $F_i > 0$ and $\Psi_i > 0$, by choosing proper F_i and β_i we have $\dot{V} \leq 0$. Therefore the stability in the sliding mode condition in Eq. (6.9) is guaranteed, and good tracking performance can be achieved.

6.2.3 Controller Design

The invariant property that provides robustness in the sliding mode control strategy occurs in the sliding mode condition. Before reaching the sliding mode condition, namely in the reaching phase, the system is susceptible to the disturbance. Therefore it is important to design a control law that forces the system starting from the reaching phase into the sliding surface.

By considering dynamics in Eq. (6.1), the dynamics of sliding surface in Eq. (6.7) is rewritten as follows:

$$\dot{s} = (F+\Psi)\dot{e} + \dot{\Psi}e + v + \gamma_d - \dot{\eta}_{2d} \tag{6.12}$$

In order to design the control law with strong behavior starting from any initial states, the synthetic input v is designed as follows:

$$v = v_{eq} - C_a\left(|s|^{\frac{1}{2}}\mathrm{sign}(s) + Gs\right) - \int_0^t C_b\left(\frac{1}{2}\mathrm{sign}(s) + \frac{3G}{2}|s|^{\frac{1}{2}}\mathrm{sign}(s) + G^2 s\right)dt, \tag{6.13a}$$

$$v_{eq} = -(F+\Psi)\dot{e} - \dot{\Psi}e + \dot{\eta}_{2d}, \tag{6.13b}$$

where $G = \mathrm{diag}\{G_1,\ldots,G_6\} \in \Re^{6\times 6}$, $C_a = \mathrm{diag}\{C_{a1},\ldots,C_{a6}\} \in \Re^{6\times 6}$, and $C_b = \mathrm{diag}\{C_{b1},\ldots,C_{b6}\} \in \Re^{6\times 6}$ are all positive definite diagonal matrices. This control law forces the system in Eq. (6.1) from any initial states towards the sliding mode condition in Eq. (6.2) against the disturbance.

From the synthetic control input $v = [v_x, v_y, v_z, v_\phi, v_\theta, v_\psi]^T$ in Eq. (6.13), we define the original inputs u_1, u_2, u_3, and u_4 by using the method presented in [43, 83], and are obtained as follows:

$$u_1 = m\sqrt{v_x^2 + v_y^2 + (v_z + g)^2} \tag{6.14}$$

$$[u_2, u_3, u_4]^T = J[v_\phi, v_\theta, v_\psi]^T - [K_1(\Theta, \dot{\Theta}), K_2(\Theta, \dot{\Theta}), K_3(\Theta, \dot{\Theta})]^T \tag{6.15}$$

6.2.4 Existence of Sliding Mode

By considering control law in Eq. (6.13) and dynamics in Eqs. (6.1) and (6.7), the dynamics in Eq. (6.12) can be rewritten in each DOF as follows:

$$\dot{s}_i = -C_{ai}\Phi_{1i} + \rho_i + \gamma_{di} \tag{6.16a}$$

$$\dot{\rho}_i = -C_{bi}\Phi_{2i} \tag{6.16b}$$

where

$$\Phi_{1i} = |s_i|^{\frac{1}{2}}\text{sign}(s_i) + G_i s_i \tag{6.17a}$$

$$\Phi_{2i} = \frac{1}{2}\text{sign}(s_i) + \frac{3G_i}{2}|s_i|^{\frac{1}{2}}\text{sign}(s_i) + G_i^2 s_i \tag{6.17b}$$

The dynamics in Eq. (6.16) has the same form with the system presented in [80].

In order to guarantee the convergence of s_i and $\dot{s}_i$ to zero in which the sliding mode exists, first we prove the convergence of Φ_{1i} and ρ_i, and therefore from Eqs. (6.16a) and (6.17a) the convergence of s_i and $\dot{s}_i$ are confirmed.

Firstly, let us assume that there exists a positive constant d_{1i} such that

$$2|\gamma_{di}| \leq d_{1i}|\Phi_{1i}|, \tag{6.18}$$

To prove the convergence of Φ_{1i} and ρ_i, let us consider the Lyapunov function candidate for the system in Eq. (6.16) as follows:

$$V = \varsigma^T P \varsigma \tag{6.19}$$

where $P = P^T$ is a symmetric positive definite matrix and $\varsigma^T = [\Phi_{1i} \;\; \rho_i]$. Taking the first derivative of Eq. (6.19), we have

$$\dot{V} = \dot{\varsigma}^T P \varsigma + \varsigma^T P \dot{\varsigma} \tag{6.20}$$

where $\dot{\varsigma}$ is obtained by considering Eq. (6.16b) and the first derivative of Eq. (6.16a), and we have

$$\begin{aligned}\dot{\varsigma} =& \Phi'_{1i} A\varsigma + \Phi'_{1i} D \\ \Phi'_{1i} =& G_i + \frac{1}{2|s_i|^{\frac{1}{2}}},\ A = \begin{bmatrix} -C_{ai} & 1 \\ -C_{bi} & 0 \end{bmatrix},\ D = \begin{bmatrix} \gamma_{di} \\ 0 \end{bmatrix}.\end{aligned} \tag{6.21}$$

Hence, the first derivative of Lyapunov function candidate in Eq. (6.20) is rewritten as follows:

$$\dot{V} = \Phi'_{1i}\varsigma^T [A^T P + PA]\varsigma + 2\Phi'_{1i} D^T P\varsigma \tag{6.22}$$

By considering disturbance bound in Eq. (6.18) and $A^T P + PA = -Q$ where $Q = Q^T$ is a positive definite matrix, we have

$$\begin{aligned}\dot{V} \leq& -\Phi'_{1i}\varsigma^T [Q - \Delta P]\varsigma \\ \Delta =& \begin{bmatrix} d_{1i} & 0 \\ 0 & 0 \end{bmatrix}\end{aligned} \tag{6.23}$$

For a specific positive definite matrix $P = P^T$, $G_i > 0$, $C_{ai} > 0$, and $C_{bi} > 0$, we have $[Q - \Delta P] > 0$, and therefore $\dot{V}$ can be negative definite. Thus, dynamics in Eq. (6.16) can be a stable system, and s_i and $\dot{s}_i$ converge to zero. The stability of the dynamics in Eq. (6.16) was also proven in [80].

6.2.5 Closed Loop Configuration

The overall closed-loop dynamics of the control system is obtained by substituting the synthetic input in Eq. (6.13) into the dynamics in Eq. (6.1), and considering the sliding surface in Eq. (6.5). We have the closed-loop dynamics of the quadcopter control system as follows:

$$\begin{aligned}&\ddot{e} + (C_a G + F + \Psi)\dot{e} + \left(C_a G(F + \Psi) + \dot{\Psi} + C_b G^2\right) e + \int_0^t C_b G^2 \left((F + \Psi)e\right) dt \\ &+ C_a |s|^{\frac{1}{2}} \mathrm{sign}(s) + \int_0^t C_b \left(\frac{1}{2}\mathrm{sign}(s) + \frac{3G}{2}|s|^{\frac{1}{2}}\mathrm{sign}(s)\right) dt - \gamma_d = 0\end{aligned} \tag{6.24}$$

Considering only linear differential equation terms in Eq. (6.24), it is seen that the properties of closed-loop dynamics varies according to the nonlinear function Ψ and its derivative. For the comparison purpose, we utilize the linear sliding surface (LSS) in Eq. (6.4) to obtain the dynamics in Eq. (6.16), and then the control input v_{eq} in Eq. (6.13b) is designed as follows:

$$v_{eq} = -\lambda\dot{e} + \dot{\eta}_{2d}, \tag{6.25}$$

The closed-loop dynamics with this control input is obtained as follows:

$$\begin{aligned}&\ddot{e}+(C_aG+\lambda)\dot{e}+(C_aG\lambda+C_bG^2)e+\int_0^t C_bG^2(\lambda e)dt\\&+C_a|s|^{\frac{1}{2}}\text{sign}(s)+\int_0^t C_b\left(\frac{1}{2}\text{sign}(s)+\frac{3G}{2}|s|^{\frac{1}{2}}\text{sign}(s)\right)dt-\gamma_d=0\end{aligned} \tag{6.26}$$

The properties of closed-loop dynamics in Eq. (6.26) is unchanged in real time because C_a, C_b, G, and λ are constant. In addition, the dynamics in Eq. (6.24) has the same closed-loop properties with (6.26) when the tracking error is zero.

6.3 Experimental Results

In this section, we evaluate the effectiveness of the proposed controller design in both robustness and energy reduction aspects. A comparative result to the second-order SMC with LSS is also presented. We conduct experiments with an experimental quadcopter testbed shown in Fig. 2.2. The desired trajectory is designed similar to the trajectory given in the previous chapter in Fig. 4.1.

6.3.1 Robustness Evaluation

In order to evaluate the effectiveness of the proposed control strategy, first we perform experiments by using the second-order SMC with LSS. The control input parameters in Eqs. (6.13a) and (6.25) are tuned to achieve the best experimental results and are obtained as follows:

$$\begin{aligned}C_a &=\text{diag}\{0.2,0.13,0.5,0.35,0.3,1.3\},\\C_b &=\text{diag}\{0.01,0.01,0.01,0.01,0.01,0.01\},\\G &=\text{diag}\{6,6,12,15,15,17\},\text{ and}\\\lambda &=\text{diag}\{26,14,17,29,25,320\}.\end{aligned}$$

The difference from our proposed control strategy is the sliding surface equation. In order to have a fair comparison, we use the above control parameters and decompose λ into F and β, where $\lambda = F+\beta = (F+\Psi)_{\max}$, $\beta = \text{diag}\{\beta_1,\ldots,\beta_6\}$, and are obtained as follows:

$$\begin{aligned}F &=\text{diag}\{7,4,7,8,8,90\},\text{ and}\\\beta &=\text{diag}\{19,10,10,21,17,230\}.\end{aligned}$$

Profiles of both sliding surface equation (LSS and NSS) in experiment without and under disturbance are shown in Figs. 6.1 and 6.2. It is seen that NSS provides relatively smoother surface compared to LSS especially in rotational motions.

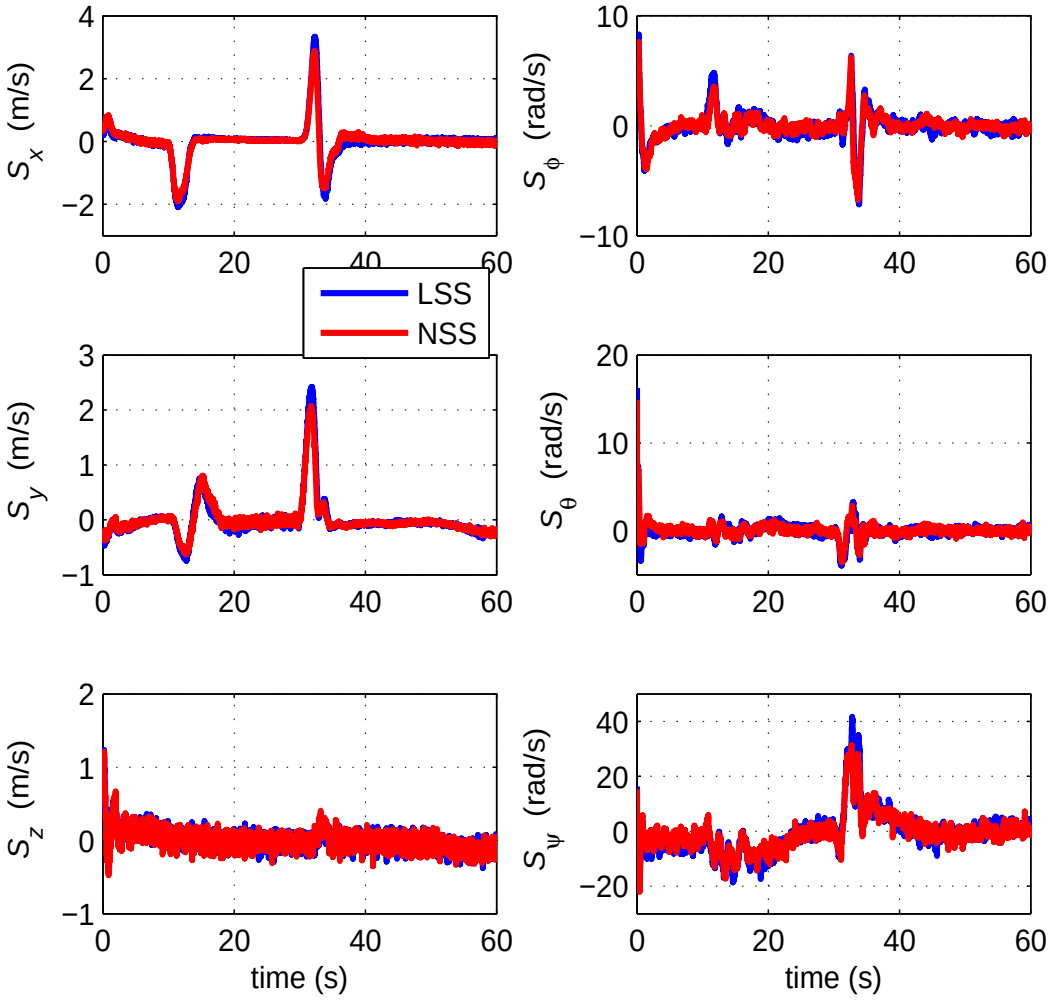

FIGURE 6.1: Profiles of sliding surface without disturbance

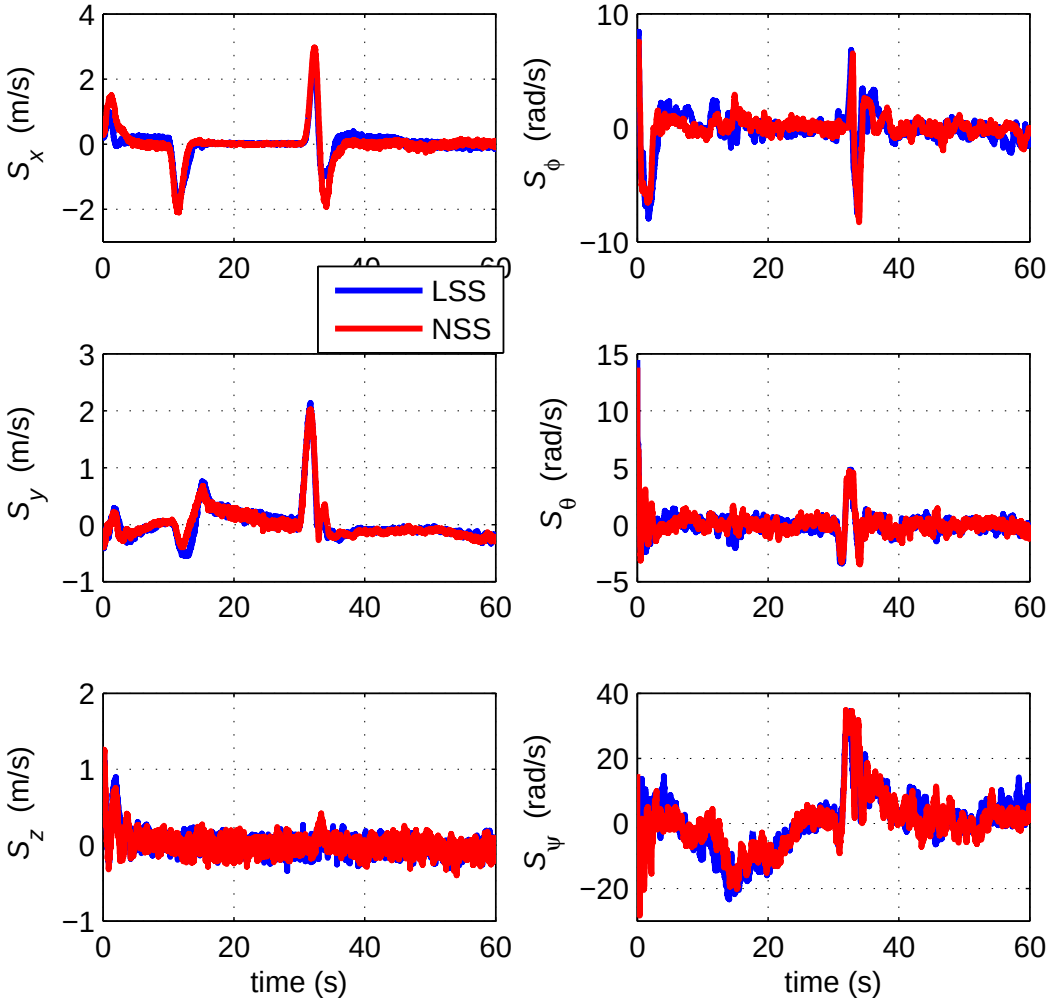

FIGURE 6.2: Profiles of sliding surface under wind disturbance

Tracking trajectory and error resulting from both control strategies in the experiments without disturbance and under wind disturbance (power: 57 W) are given in Figs. 6.3–6.6. It is seen that both control strategies provide robustness in experiments without and under wind disturbance. Robustness of these control strategies is also evaluated by applying relatively high disturbance produced by three electric fan (power: 57 W, 49 W, and 37 W), and the tracking error performances are shown in Fig. 6.7. Reliability of these methods is also evaluated by performing seven times experiments and the results are illustrated in Figs. 6.8–6.10. On average, the performances of both control strategies are relatively similar. Small differences are obtained in which the second-order SMC with NSS provides relatively smaller squared-root mean error and/or error variance, which is also confirmed in Tables 6.1–6.3 as summary of Figs. 6.8–6.10. This difference is caused by the nonlinear function Ψ and its derivative, $\dot{\Psi}$. Profile of Ψ and $\dot{\Psi}$ in conditions without disturbance and under wind disturbance are given in Figs. 6.11 and 6.12. It

is seen that Ψ and $\dot{\Psi}$ have contribution when the trajectory changes or if tracking error exists. The variation of Ψ and $\dot{\Psi}$ contribute to change the closed-loop properties of system: natural frequency (ω) and damping ratio (ζ). Considering only the dominant poles of the linear differential equation part of Eqs. 6.24 and 6.26, and all tuned control parameters above, profiles of the closed-loop properties of GSTA with LSS and NSS are given in Figs. 6.13–6.15. It is seen that the LSS provides constant closed-loop properties while NSS has varying properties.

TABLE 6.1: Average of root-squared mean error (RSME) and error variance (Var) for experiments without disturbance.

	Translational motion		Rotational motion	
	RSME (mm)	Var (mm)	RSME (deg)	Var (deg)
GSTA with LSS	1.066	0.404	0.156	4.995
GSTA with NSS	0.825	0.378	0.242	4.658

TABLE 6.2: Average of root-squared mean error (RSME) and error variance (Var) for experiments under low wind disturbance.

	Translational motion		Rotational motion	
	RSME (mm)	Var (mm)	RSME (deg)	Var (deg)
GSTA with LSS	2.077	0.336	0.173	6.746
GSTA with NSS	1.614	0.434	0.189	6.563

TABLE 6.3: Average of root-squared mean error (RSME) and error variance (Var) for experiments under high wind disturbance.

	Translational motion		Rotational motion	
	RSME (mm)	Var (mm)	RSME (deg)	Var (deg)
GSTA with LSS	3.474	2.069	0.242	11.764
GSTA with NSS	2.388	0.967	0.125	7.979

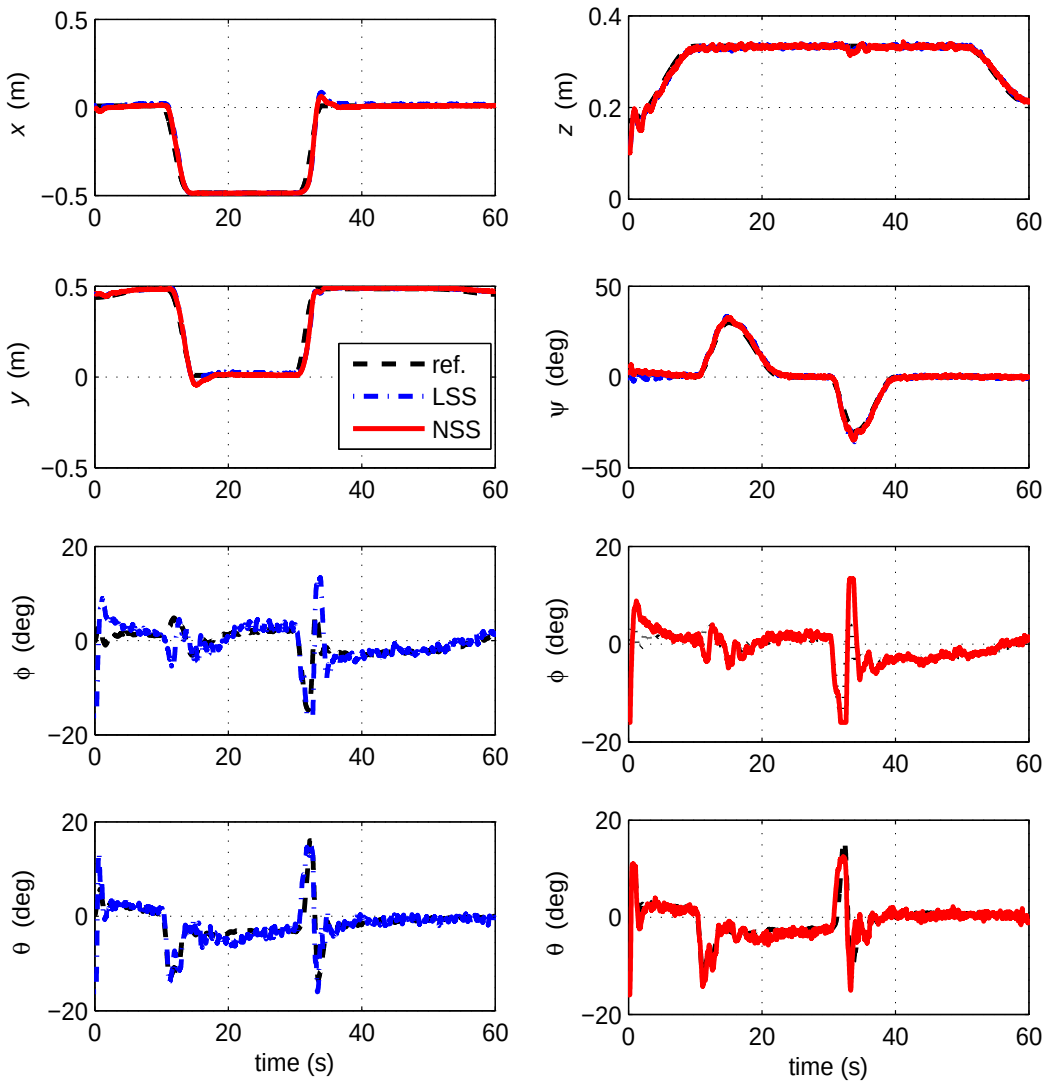

FIGURE 6.3: Trajectory tracking without disturbance

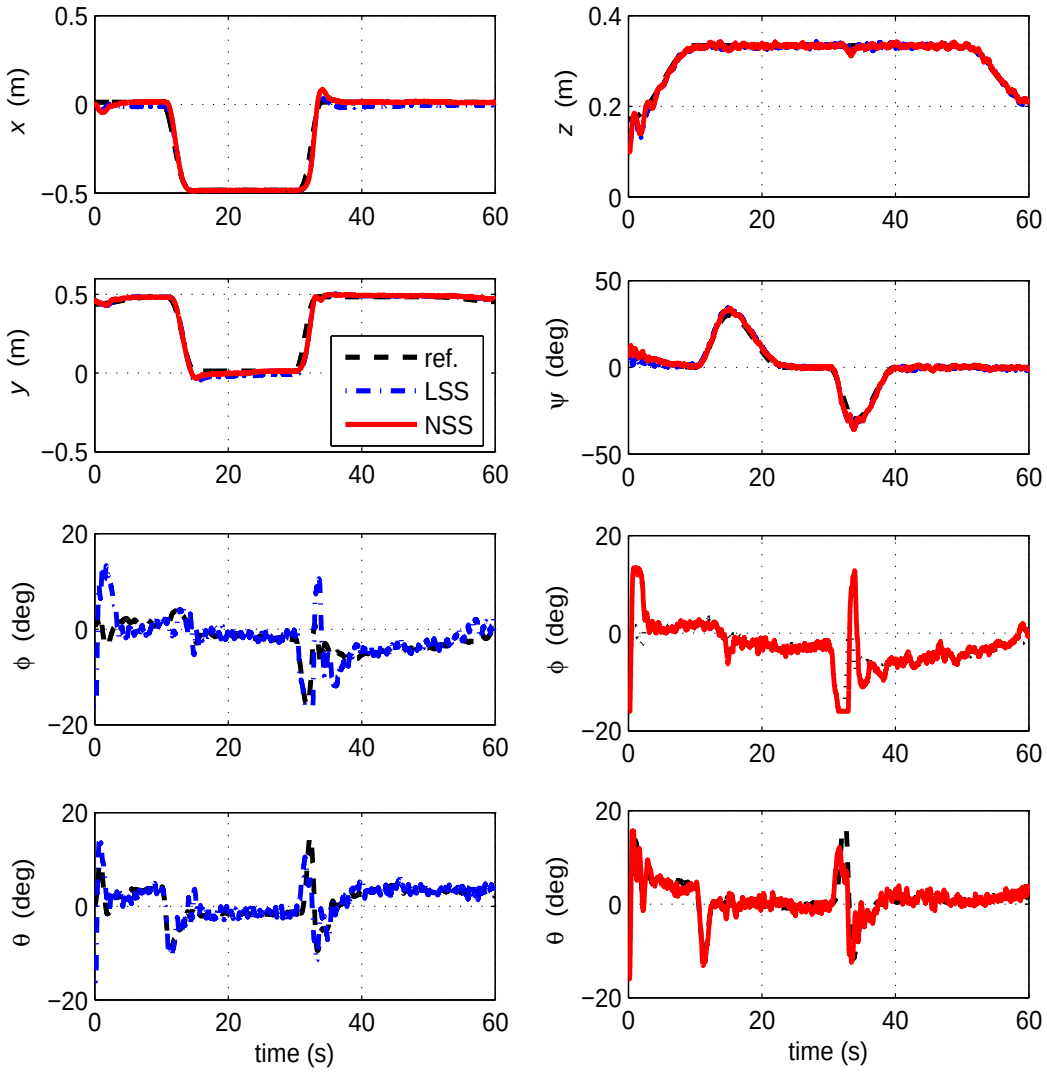

FIGURE 6.4: Trajectory tracking under wind disturbance

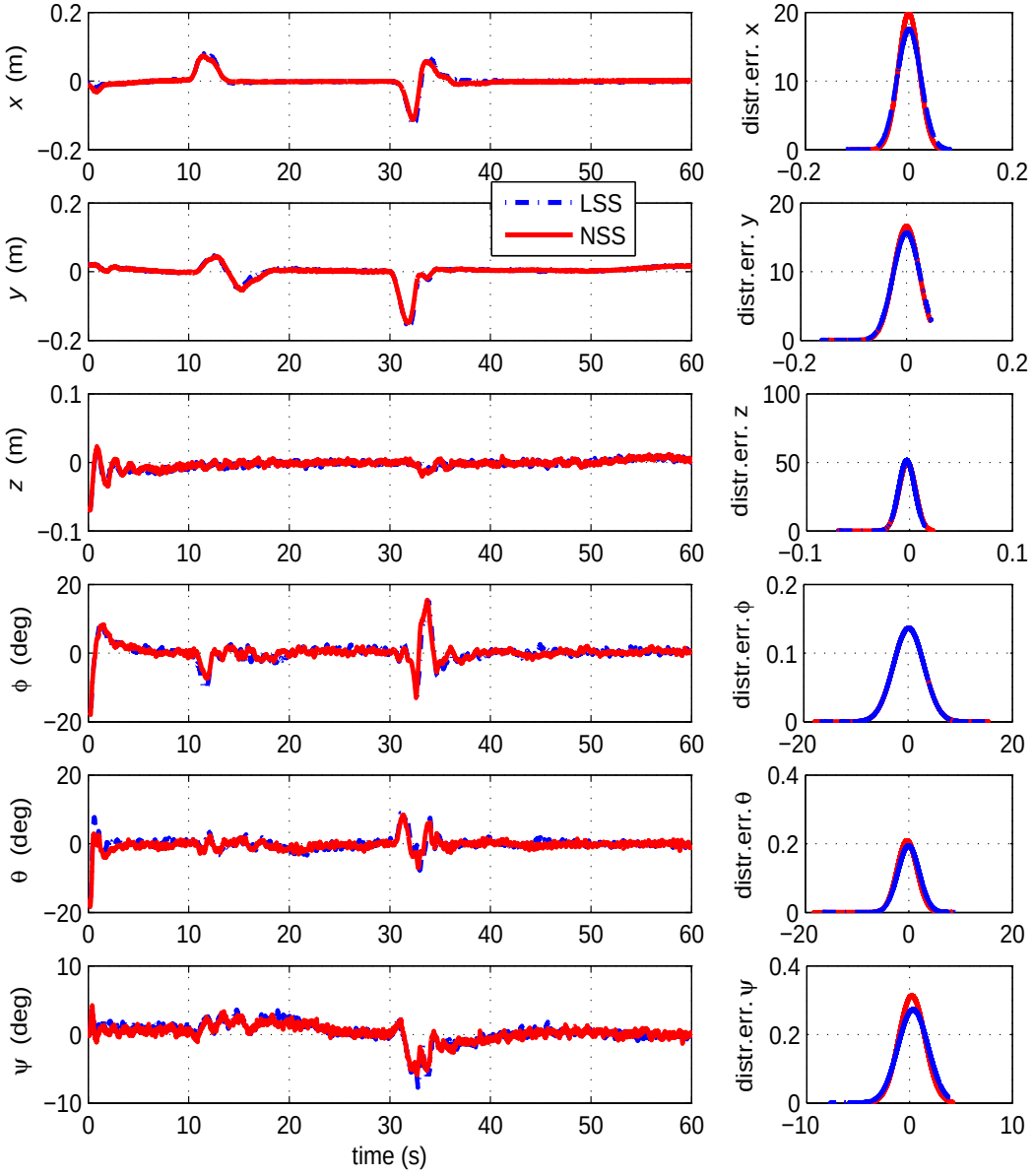

FIGURE 6.5: Tracking error and its distribution without disturbance

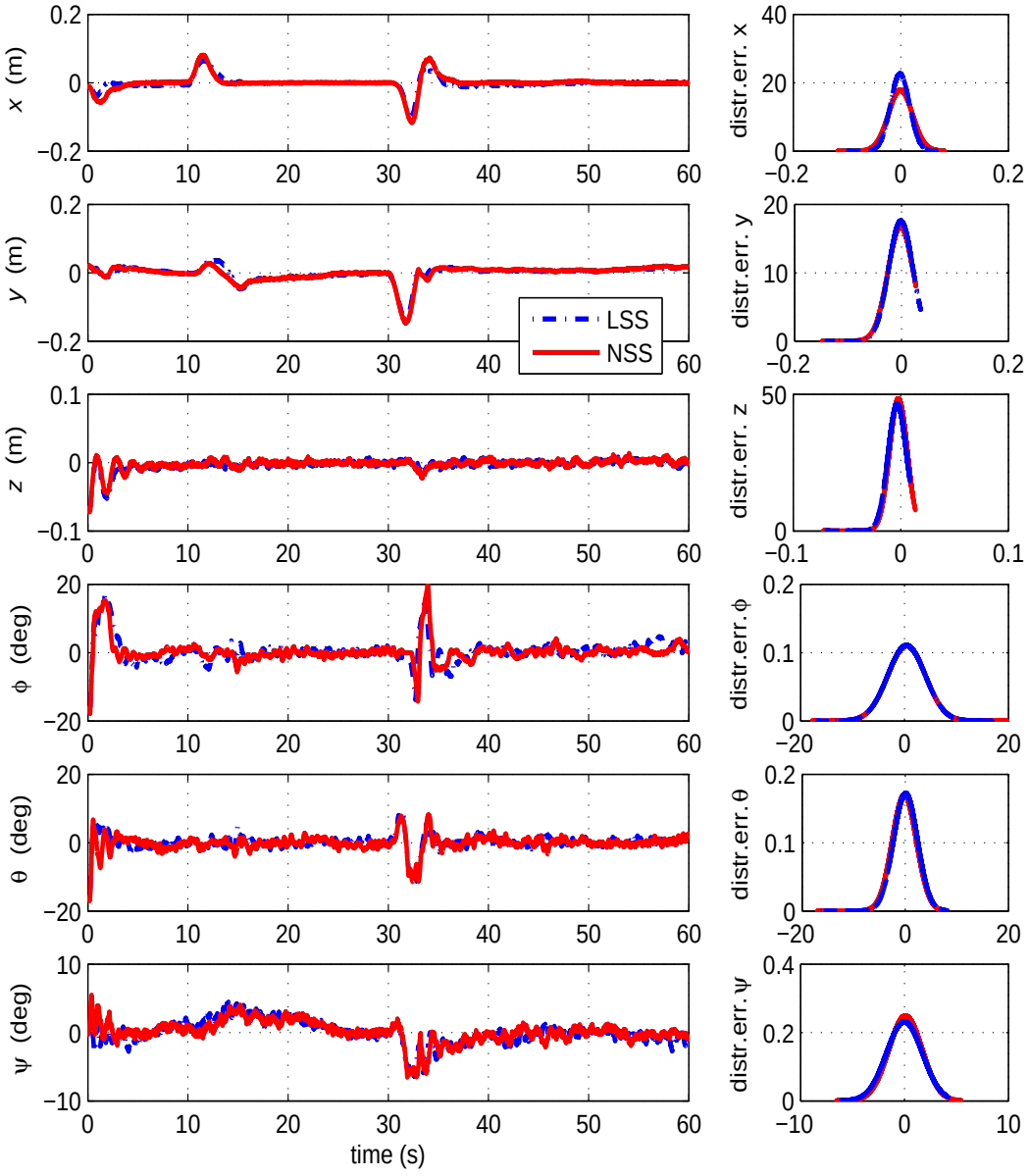

FIGURE 6.6: Tracking error and its distribution under low wind disturbance

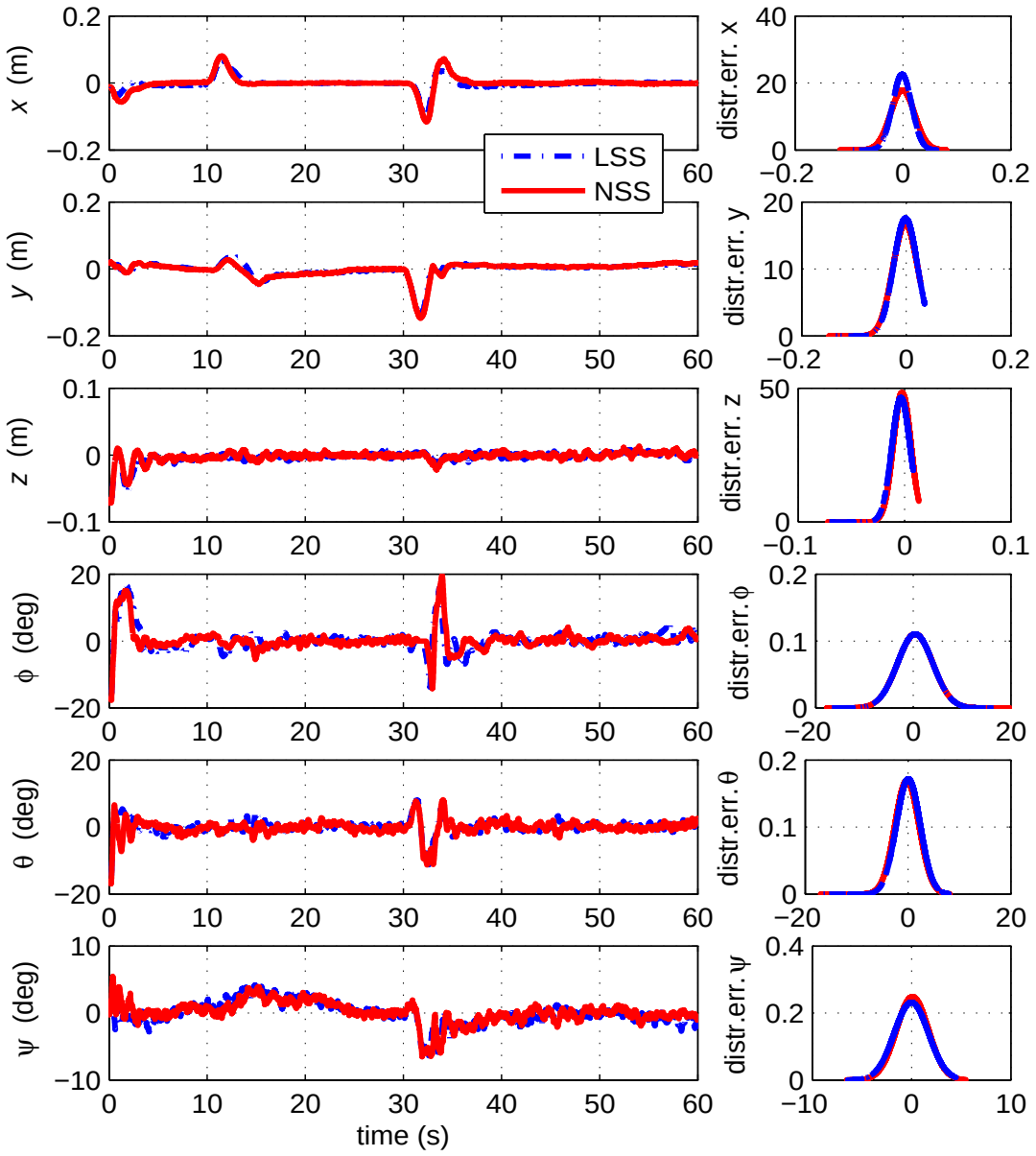

FIGURE 6.7: Tracking error and its distribution under high wind disturbance

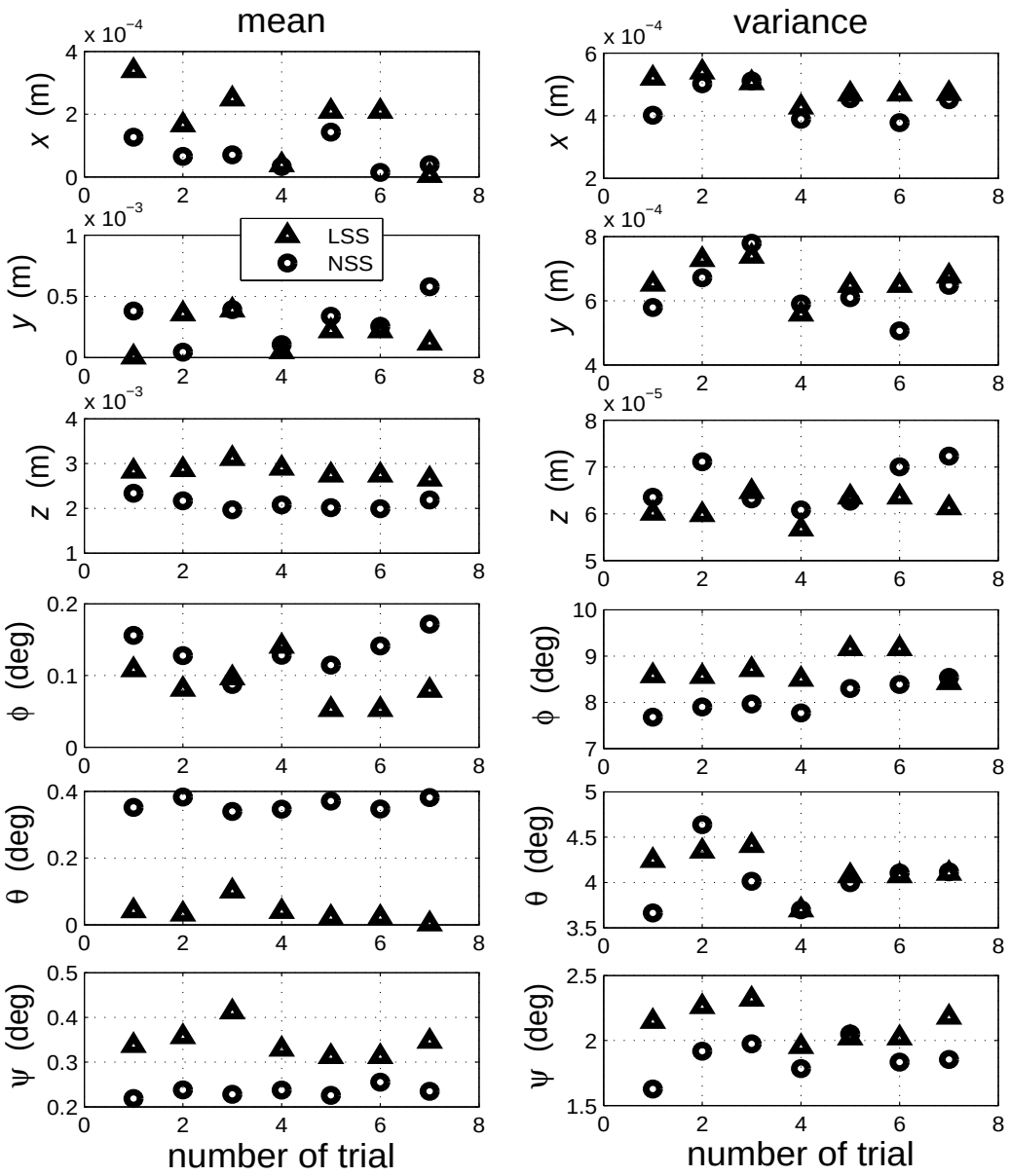

FIGURE 6.8: RSME and error variance for experiments without disturbance

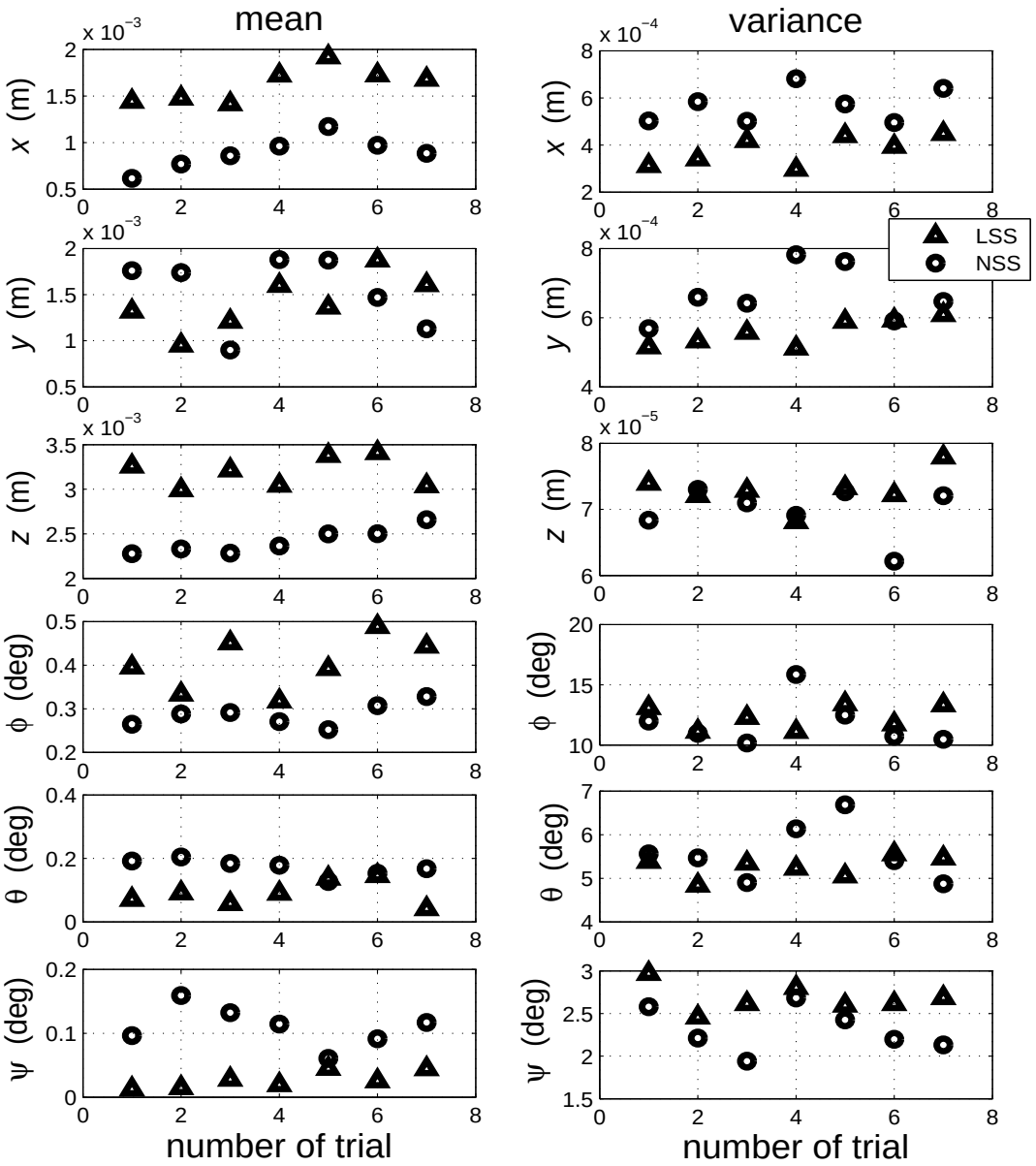

FIGURE 6.9: RSME and error variance for experiments under low wind disturbance

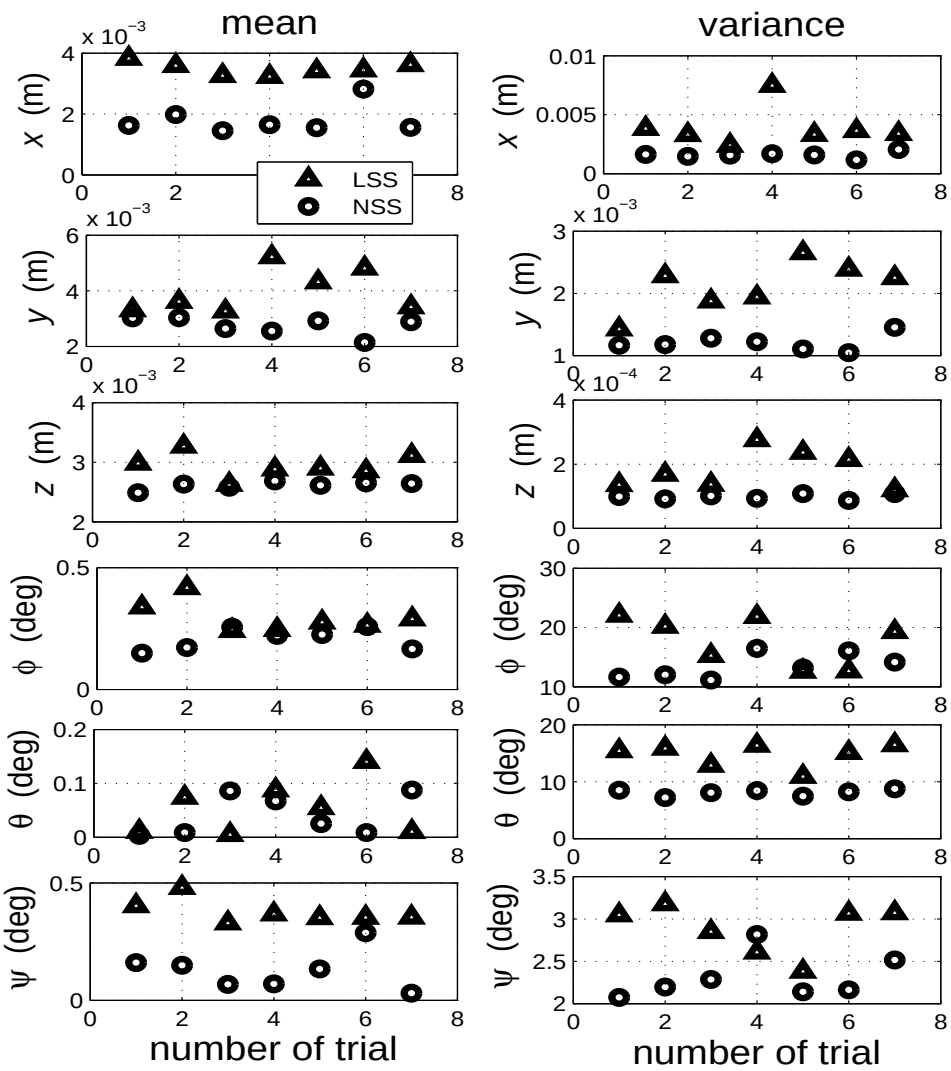

FIGURE 6.10: RSME and error variance for experiments under high wind disturbance

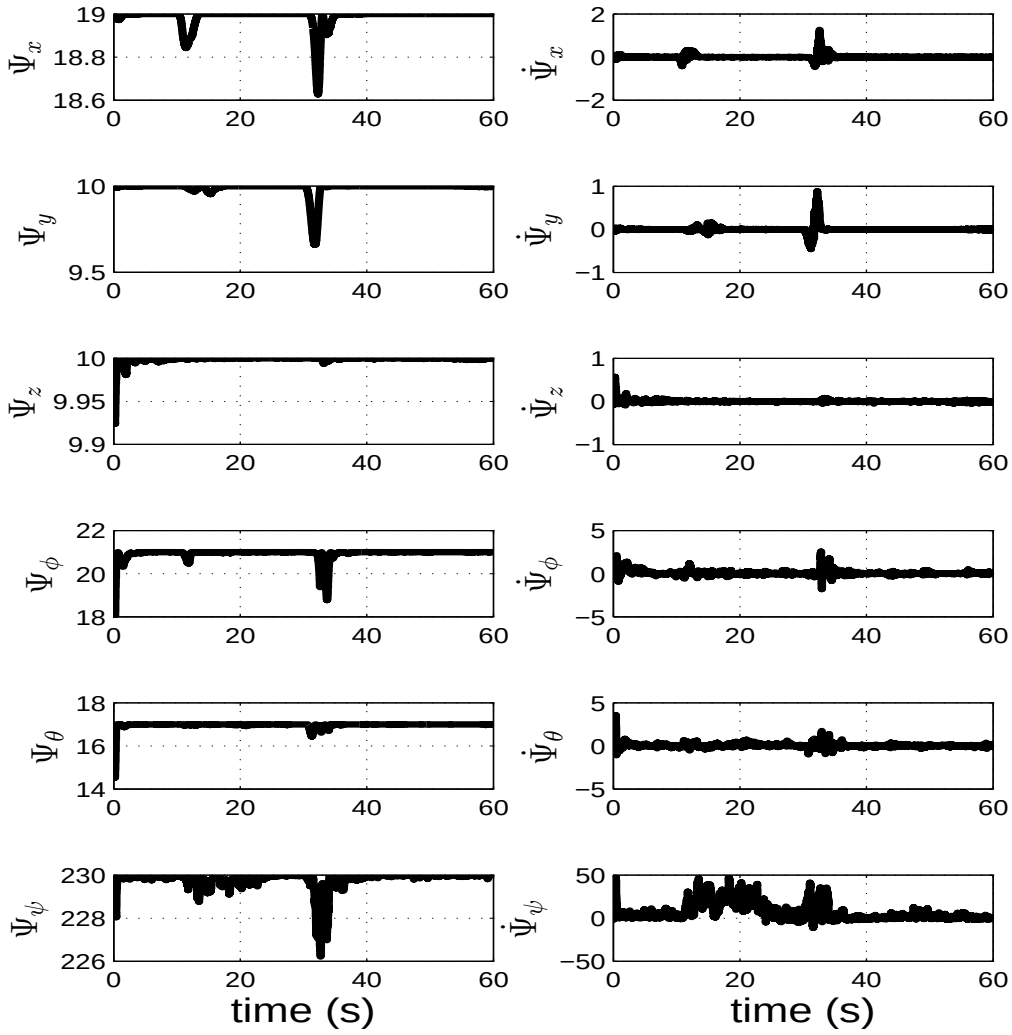

FIGURE 6.11: Profiles of Ψ and $\dot{\Psi}$ in experiment without disturbance

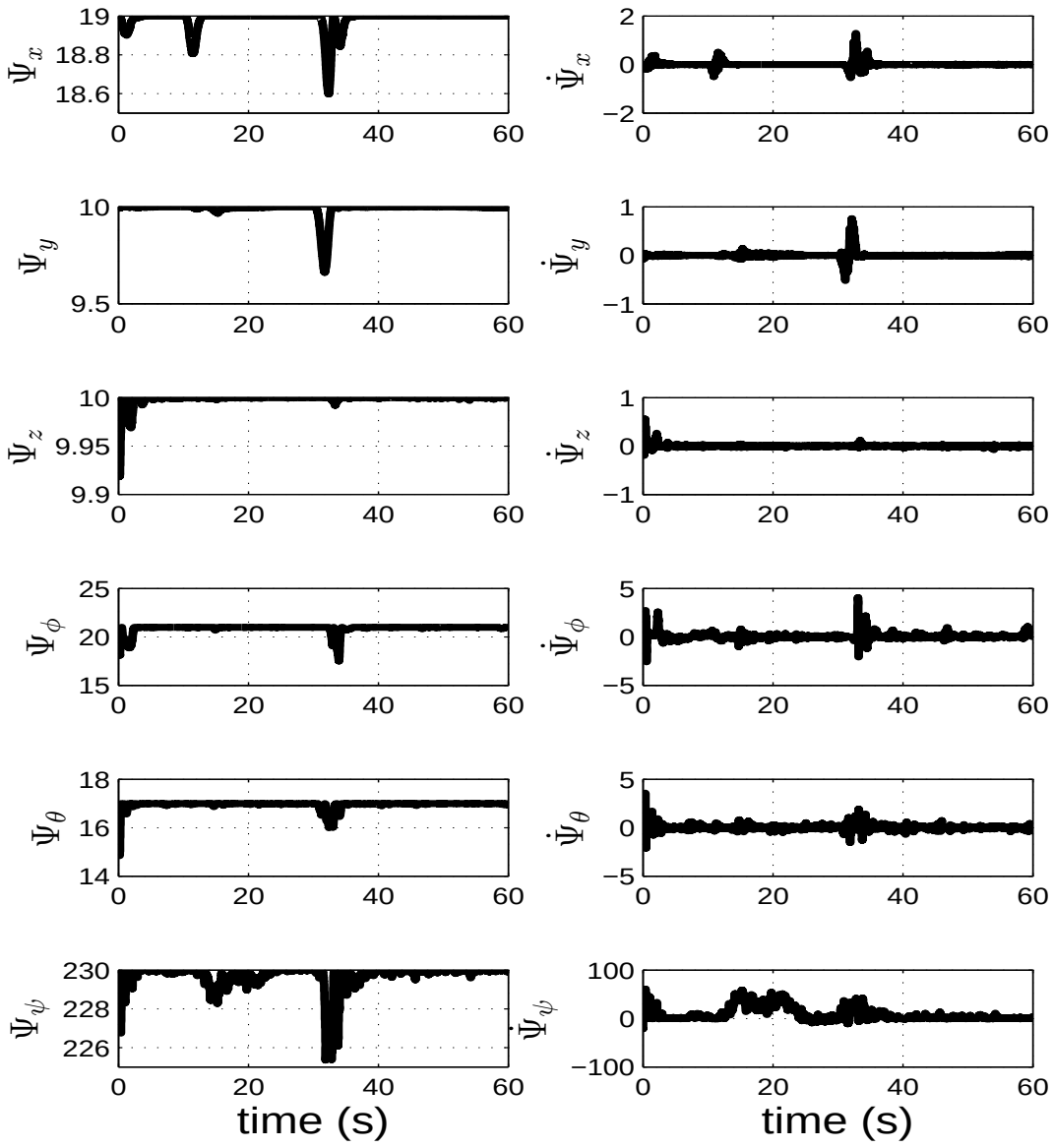

FIGURE 6.12: Profiles of Ψ and $\dot{\Psi}$ in experiment under low wind disturbance

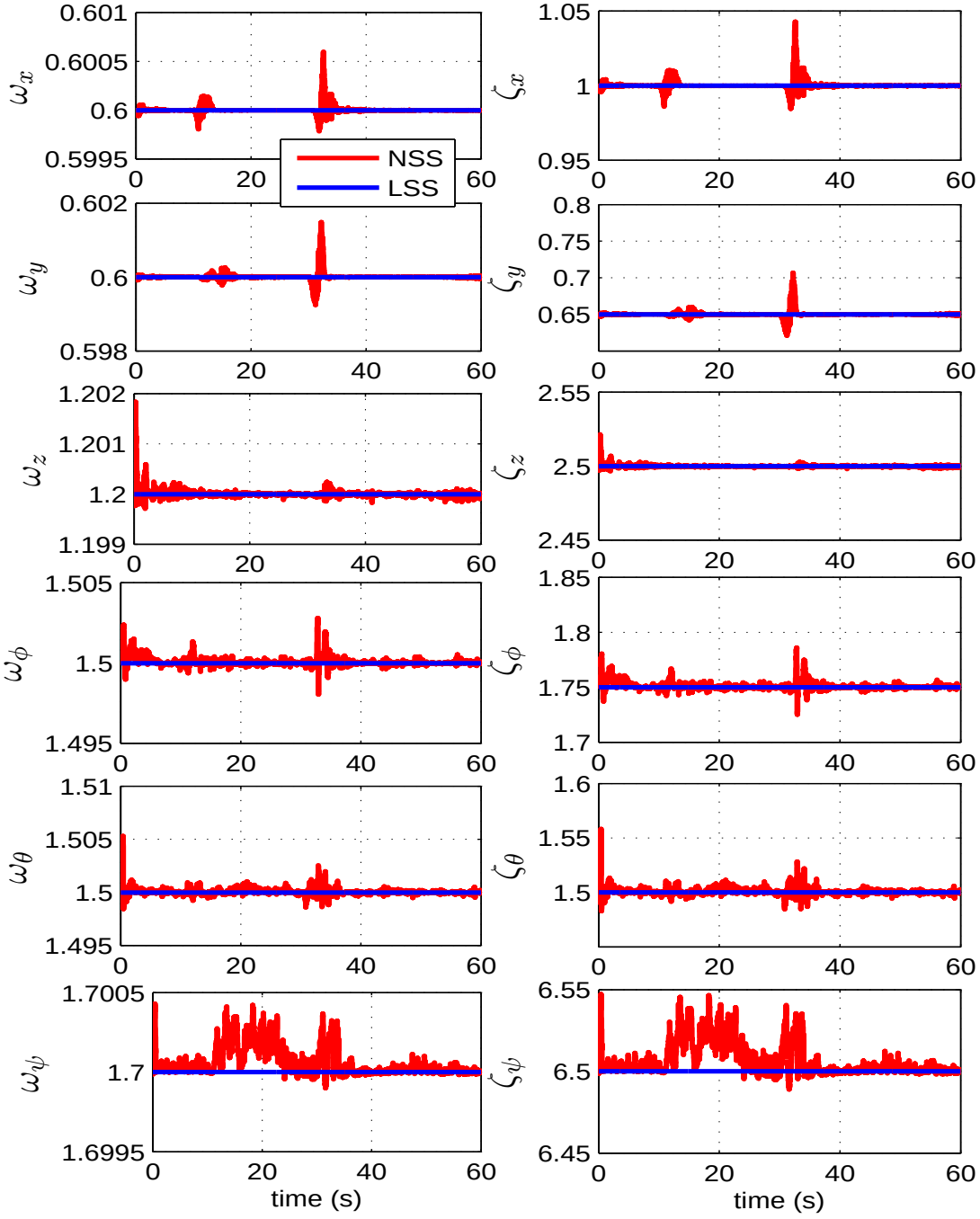

FIGURE 6.13: Profiles of closed-loop properties in experiment without wind disturbance

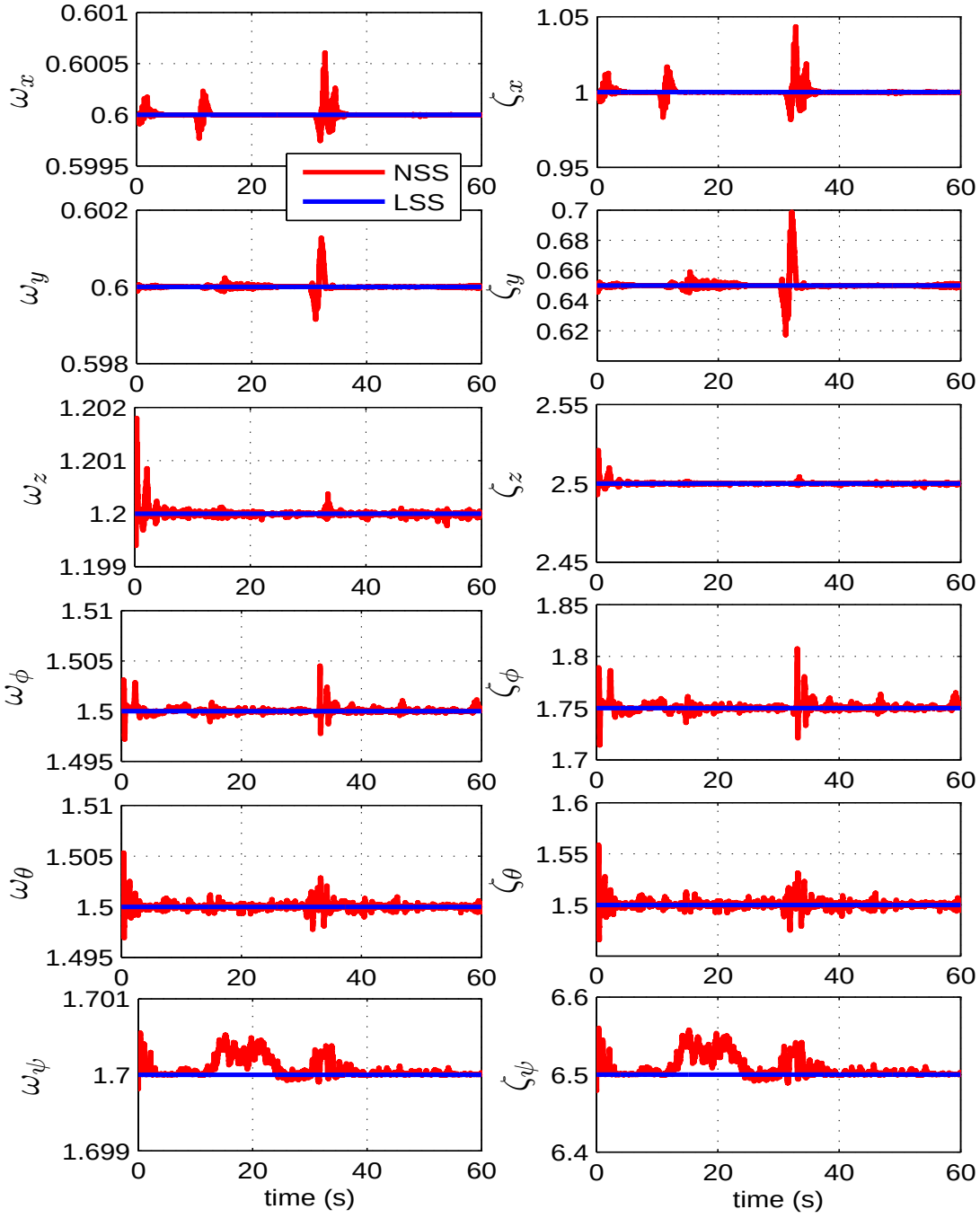

FIGURE 6.14: Profiles of closed-loop properties in experiment under low wind disturbance

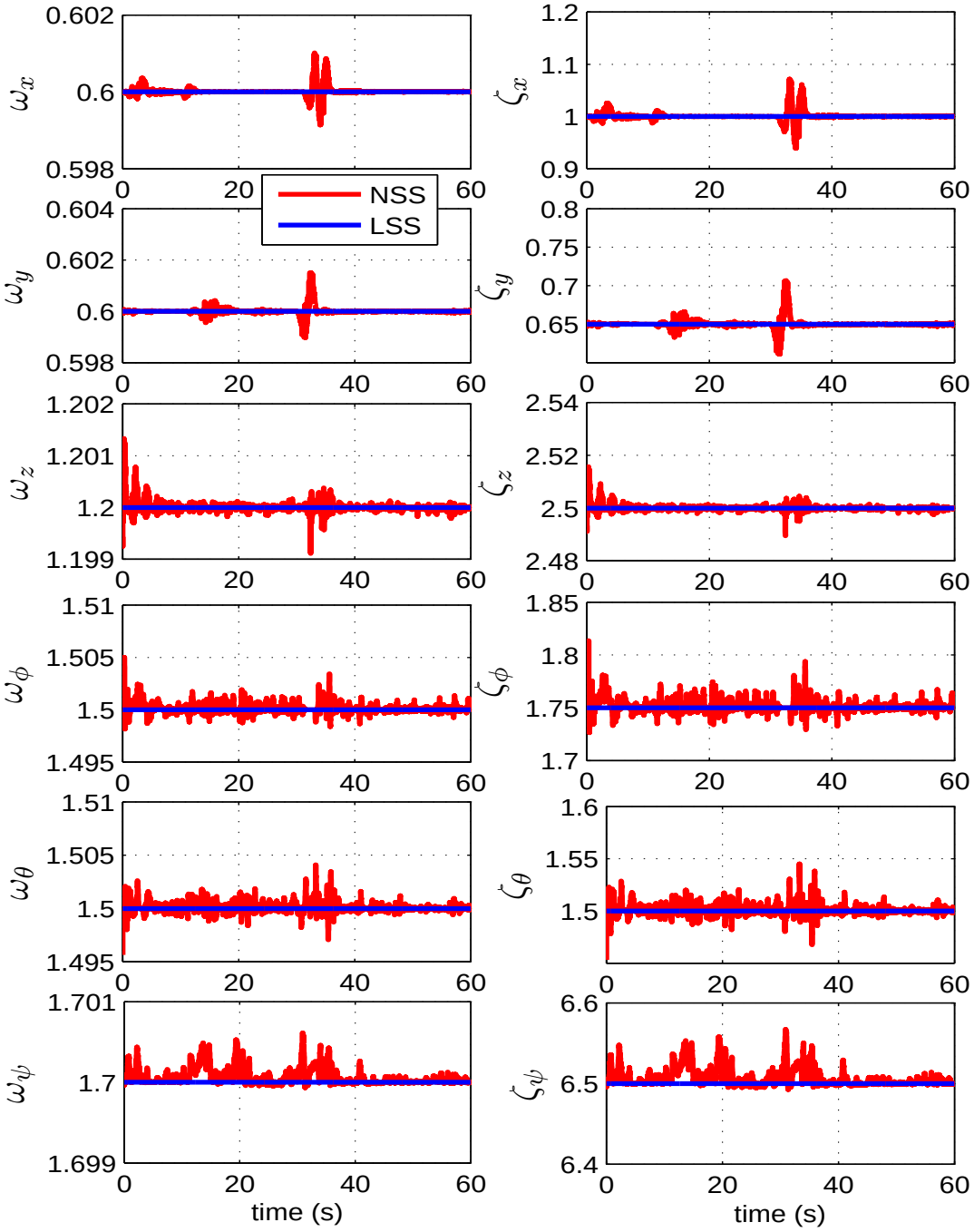

FIGURE 6.15: Profiles of closed-loop properties in experiment under high wind disturbance

6.3.2 Energy Evaluation

The variance of Ψ, $\dot{\Psi}$ and closed-loop properties as shown in Figs. 6.11– 6.15 contribute to the profiles of control inputs as shown in Figs. 6.16 and 6.17, and power applied on each actuator as shown in Figs. 6.18 and 6.19. From profiles of power on each actuator, it is seen that the SMC with LSS provides higher power than that with NSS, especially on motor M_3 for experiment without disturbance, and motor M_2 and motor M_3 for experiment under wind disturbance. By

integrating the power applied on each actuator during the flight control, total energy consumed on each actuator can be obtained. By summing the energy consumption on all four actuators, total electric energy consumed by all actuators is calculated and shown in Fig. 6.20. It is seen that our proposed method effective to reduce energy consumption during completion a mission in conditions without and under wind disturbance. On average, the second-order SMC with NSS reduces total energy consumed by all four actuators from the second-order SMC with LSS by about 4.8% when the disturbance does not exist, and by about 5.4% when a low disturbance exists. By applying a high wind disturbance, the NSS can reduces the energy by about 2.9%.

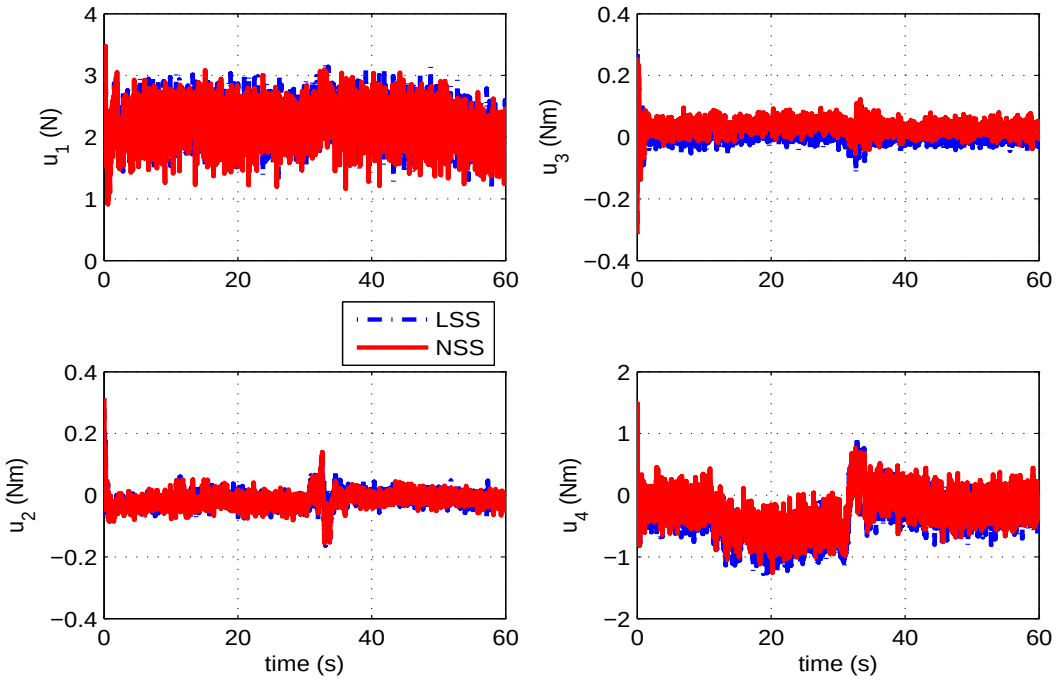

FIGURE 6.16: Profiles of control inputs in experiment without disturbance

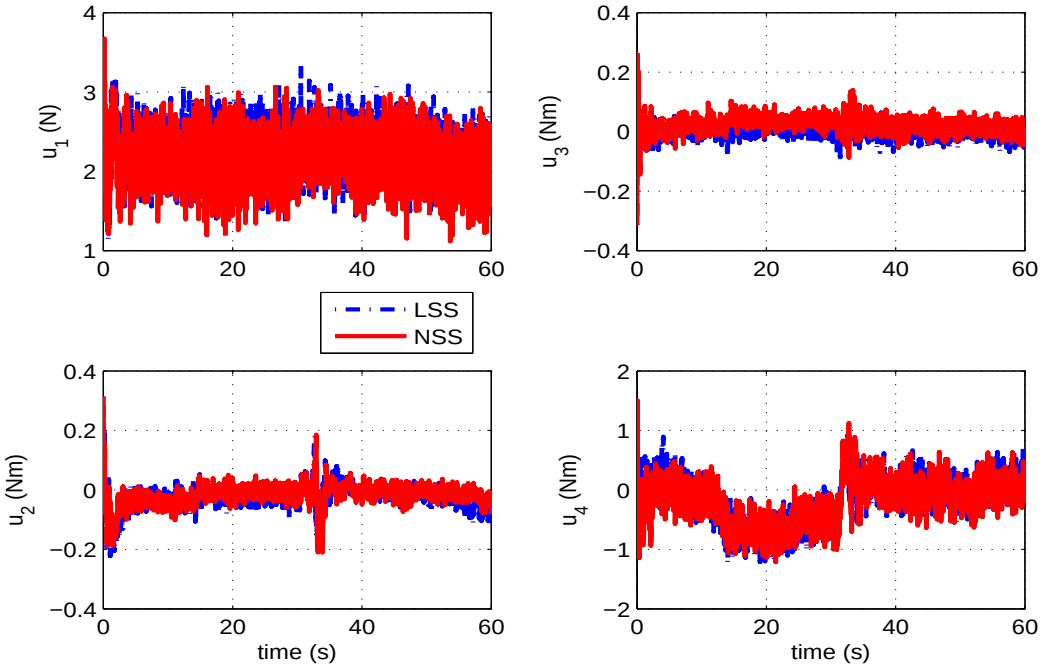

FIGURE 6.17: Profiles of control inputs in experiment under low wind disturbance

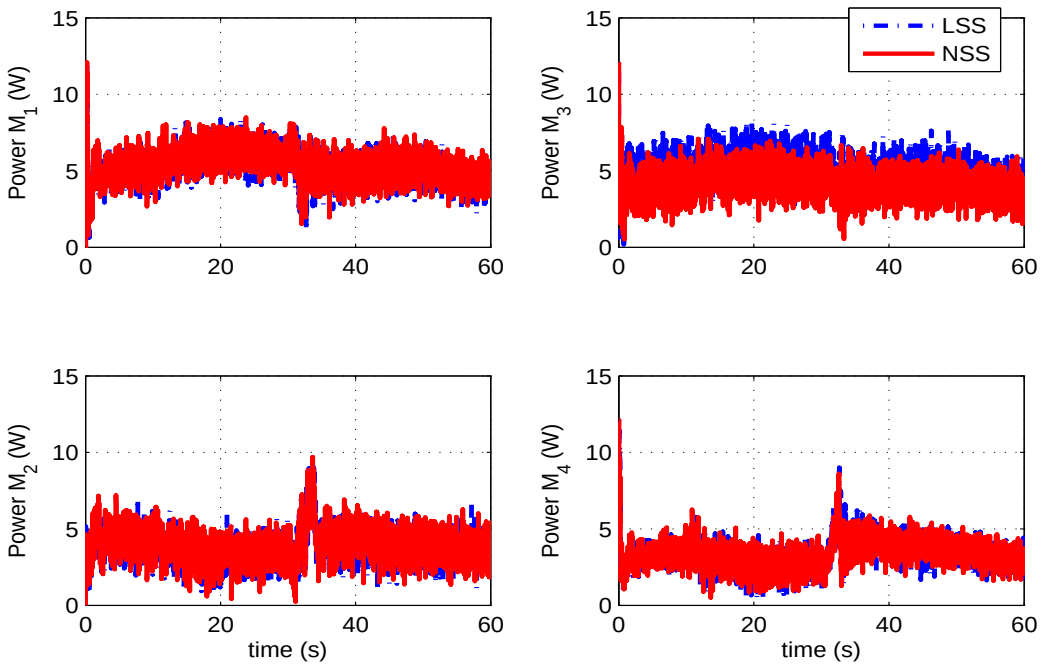

FIGURE 6.18: Profiles of power applied on each actuator in experiment without disturbance

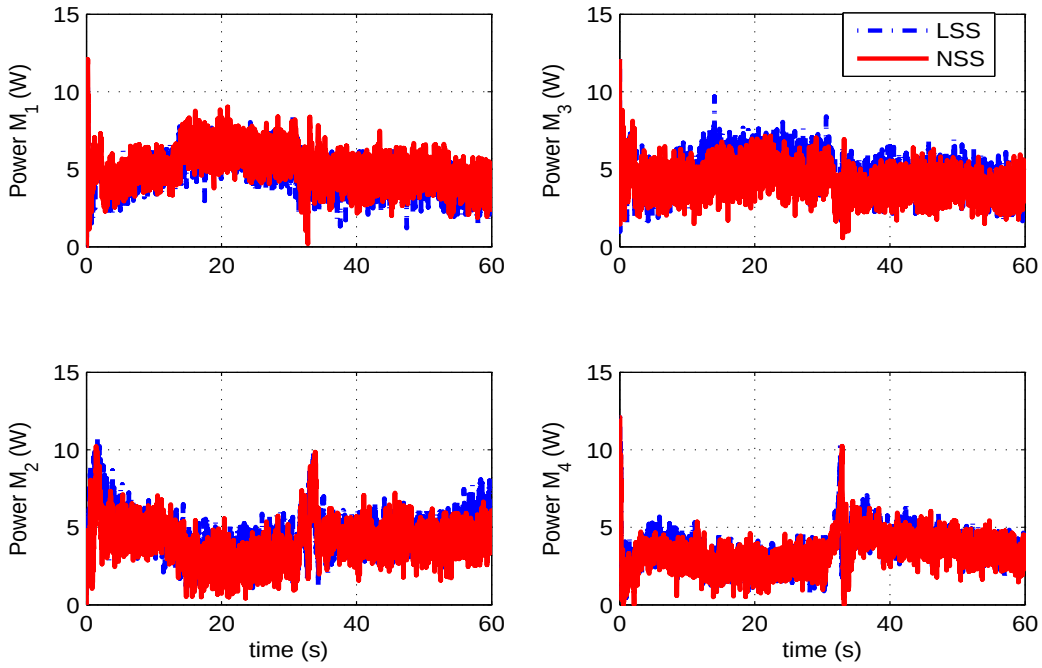

FIGURE 6.19: Profiles of power applied on each actuator in experiment under low wind disturbance

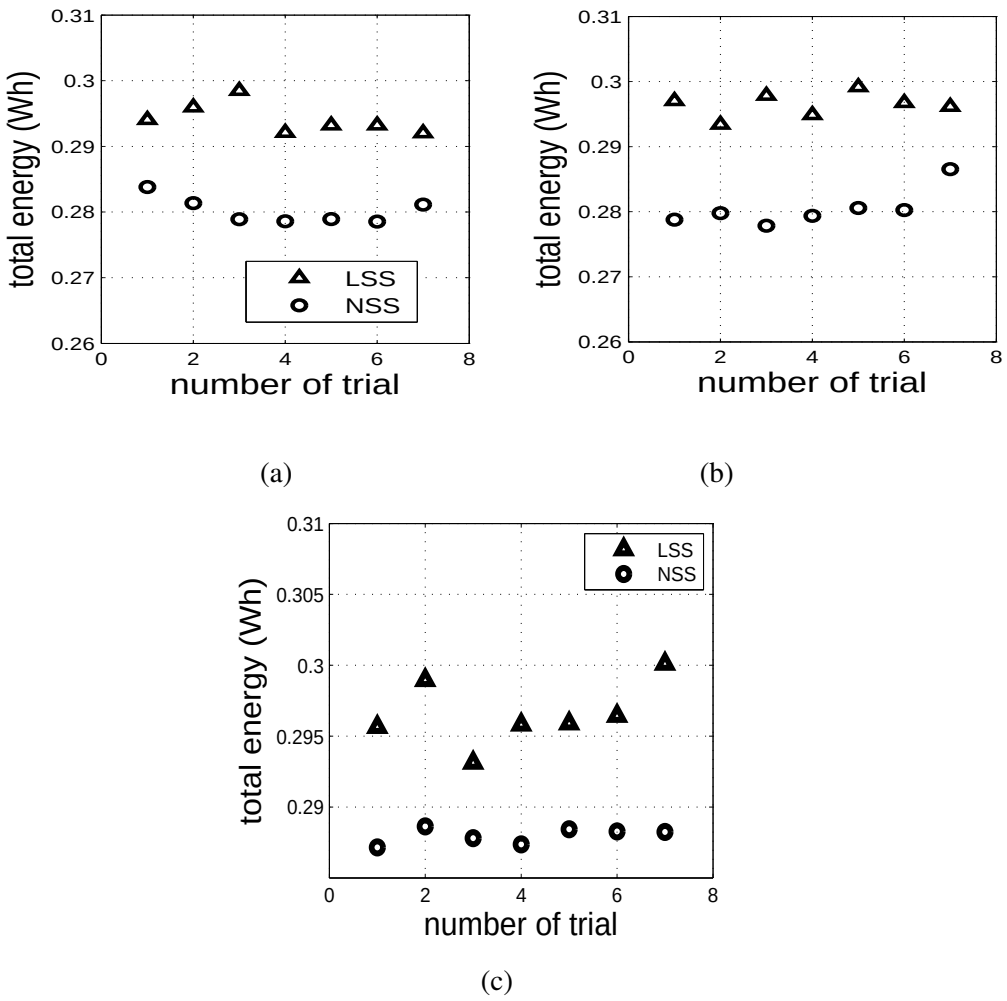

FIGURE 6.20: Profiles of energy; (a) without disturbance; (b) under low wind disturbance; (c) under high wind disturbance.

6.4 Conclusion

In this study, a nonlinear sliding surface for the second-order SMC is proposed for a robust and energy-efficient controller design of a quadcopter. Stability of the proposed control system is proved by the Lyapunov stability theory both in the sliding mode condition and beyond the sliding mode condition. Effectiveness and reliability of the proposed method are evaluated by performing several times experiments with an experimental quadcopter testbed. The proposed method reduces the energy consumption from the second-order SMC with LSS in the experiments without and under disturbance and improves the robustness performance by producing relatively smaller RSME and/or error variance.

Chapter 7

Summary and Future Works

7.1 Summary

This thesis proposes a robust and energy-efficient controller for a quadcopter. First, a simple and general control structure for the quadcopter is designed using a cascade structure. This structure is divided into two loops: an outer loop and an inner loop. The outer loop handles the translational motion, and the inner loop handles the rotational motion. The control law is applied through synthetic input, which is designed in each motion. To cope with the under-actuated problem of the quadcopter, the desired outputs are chosen as a translational position (x_d, y_d, z_d) and heading or yaw angle (ψ_d). The outer loop derives the original control input for the translational motion by utilizing a least-squares algorithm to take into account all dynamics in the translational motion. The outer loop also provides the desired role angle (ϕ_d) and pitch angle (θ_d) using an algebraic calculation based on the translational motion dynamics. The original inputs for the rotational motion are solved simply by applying the synthetic inputs obtained from the control design in the inner loop to the rotational dynamics of the quadcopter. Using this control structure, any general control algorithm can be applied easily for controlling the quadcopter.

In this study, the robust control strategy is designed based on the SMC algorithm. The controller is designed by considering the energy reduction in its operation. We initially reduced the energy consumption from the SMC design by reducing the chattering phenomenon. The chatter reduction is attempted by designing a thin boundary layer around the sliding surface. From the experiments, it is seen that the chatter reduction is effective in reducing the energy consumption. Unfortunately, using the boundary layer method, which changes the discontinuous control input to a continuous one within this layer, the robustness of the control system is reduced.

The behavior of closed-loop dynamics for the SMC strategy can be determined from the design of the sliding surface, which is originally designed with a linear differential equation; therefore,

the system has constant closed-loop properties. In this study, two nonlinear sliding surfaces are proposed as a function of error to vary the time-constant within the sliding mode condition. These nonlinear sliding surfaces have different characteristics in varying the time-constant as changing of error. The first nonlinear sliding surface (NSS-1) reduces the time-constant if the error increases; therefore, the control system responds faster to reduce the error. By reducing the error, which converges to zero, the time-constant increases and converges to a constant value. The second nonlinear sliding surface (NSS-2) is designed with an opposite characteristic from NSS-1. NSS-2 increases the time-constant if error increases, and the time-constant decreases to a constant value when the error converges to zero. In a zero or small error state, the control system response is faster; therefore, the controller reacts more strongly to the change in this condition. These nonlinear sliding surfaces also provide a variation in the properties of the overall closed-loop dynamics (damping ratio and natural frequency). The stability of these proposed methods is evaluated by employing the Lyapunov stability theory. Furthermore, the effectiveness of these two nonlinear sliding surfaces is evaluated using the experimental quadcopter testbed. The experimental results show that both nonlinear sliding surfaces are effective in improving the robustness of the control system in a wind disturbance condition from the SMC strategy with a linear sliding surface, resulting in smaller root-squared mean error and error variance. These nonlinear sliding surfaces are also effective in reducing the energy consumption in the wind disturbance condition. With both nonlinear sliding surfaces, NSS-2 is seen as more effective than NSS-1, as shown in the experimental results.

Robustness and energy saving are important factors in designing the control system. With the SMC strategy, the discontinuous control input provides robustness in the sliding mode condition. Therefore, it is important to keep this control input property, although it is also useful to reduce the chatter for reducing the energy consumption. The second-order SMC strategy offers a good solution for reducing the chattering phenomenon by keeping the discontinuous control part. With this control strategy, the discontinuous control input is shifted into the second-order time-derivative of the sliding surface function while in the standard SMC strategy, the discontinuous control input occurs in the first-order time-derivative of the sliding surface function. This control strategy is also effective in improving the tracking performance because it includes an integral part in the control input calculation. Among the designs for the second-order SMC, STA becomes a reasonable choice because it needs only the sliding surface information. However, the original STA only provides strong behavior around the origin of the sliding surface. To also provide strong behavior when the states are far from the origin of the sliding surface, a linear stabilizing term is included, which is known as generalized-STA (GSTA). Furthermore, to reduce energy consumption during the control operation, NSS-2 is utilized. The stability of this proposed control strategy is guaranteed in the sense of the Lyapunov stability theory. The effectiveness of the proposed method is evaluated by performing several repetitions of an experiment using the experimental quadcopter testbed. The experimental results show that GSTA with

a nonlinear sliding surface improves the robustness in comparison with GSTA using a linear sliding surface by providing a relatively smaller root-squared mean error (RSME) and/or error variance. In addition, GSTA with a nonlinear sliding surface consumes lesser energy than that with a linear sliding surface.

To evaluate the performance of the control strategies discussed in this thesis in terms of robustness and energy efficiency, the experimental results are summarized in the following tables:

TABLE 7.1: Root-squared mean error (RSME) and error variance (Var) for experiment without disturbance.

	Translational motion		Rotational motion	
	RSME (mm)	Var (mm)	RSME (deg)	Var (deg)
PD controller	16.11	0.334	2.838	5.517
PID controller	1.823	0.264	0.968	5.354
SMC with sign (PD LSS)	11.698	0.265	2.861	5.301
SMC with sat (PD LSS)	21.048	0.529	2.841	6.056
SMC with sign (PID LSS)	1.101	0.208	1.014	6.062
SMC with sat (PID LSS)	2.885	0.375	1.052	5.903
SMC with NSS-1	11.249	0.241	1.395	2.341
SMC with NSS-2	11.211	0.282	1.167	3.142
GSTA with LSS	1.067	0.404	0.156	4.995
GSTA with NSS	0.825	0.378	0.242	4.658

TABLE 7.2: Root-squared mean error (RSME) and error variance (Var) for experiment under wind disturbance.

	Translational motion		Rotational motion	
	RSME (mm)	Var (mm)	RSME (deg)	Var (deg)
PD controller	27.54	0.69	2.979	10.016
PID controller	2.729	0.406	0.745	7.714
SMC with sign (PD LSS)	23.946	0.598	2.681	8.206
SMC with sat (PD LSS)	33.345	0.962	3.018	11.304
SMC with sign (PID LSS)	1.777	0.380	0.616	7.367
SMC with sat (PID LSS)	3.785	0.481	0.648	7.473
SMC with NSS-1	15.247	0.347	1.380	4.690
SMC with NSS-2	14.877	0.444	1.071	3.893
GSTA with LSS	2.078	0.337	0.173	6.756
GSTA with NSS	1.615	0.434	0.189	6.563

TABLE 7.3: Total energy consumption during the control operation.

	without disturbance (mWh)	under disturbance (mWh)
PD controller	283.189	287.527
PID controller	288.165	298.036
SMC with sign (PD LSS)	281.383	283.216
SMC with sat (PD LSS)	278.095	282.902
SMC with sign (PID LSS)	283.568	282.152
SMC with sat (PID LSS)	283.592	279.872
SMC with NSS-1	278.455	280.071
SMC with NSS-2	277.261	278.718
GSTA with LSS	294.132	296.446
GSTA with NSS	280.171	280.446

Tables 7.1 and 7.2 show that GSTA with a nonlinear sliding surface (NSS) is superior in comparison with the other approaches by providing relatively small RSME for both translational and rotational motion in conditions with and without wind disturbance. GSTA with NSS also provides uniform performance in condition with and without wind disturbance by consuming energy in a small difference amount, as shown in Table 7.3.

7.2 Future Works

- In this thesis, two nonlinear sliding surfaces (NSS-1 and NSS-2) are designed with different characteristics in the sliding mode condition. NSS-1 has stronger behavior if the error is relatively large, and the NSS-2 has stronger behavior if the error is relatively small or close to zero. However, the nonlinear sliding surface is not a unique function. Therefore, it will be useful if the sliding surface function is designed with strong behavior in all conditions.

- In this thesis, the magnitude of disturbances included in the quadcopter dynamics is unknown and assumed to be bounded. However, if the magnitude of disturbances can be estimated, it will be useful for improving control performance. In future works, this thesis will be extended by applying a robust disturbance observer.

- Performance of the control strategies proposed in this thesis depends on the control parameter values. However, it is difficult to obtain appropriate values. In future works, it will be useful if an adaptive algorithm can be designed to estimate the control parameters so that optimum performance can be obtained.

- The effectiveness and performance of all controller strategies discussed in this thesis are evaluated using an experimental quadcopter testbed. In the future, this work will be extended by applying the proposed control strategies in a real autonomous quadcopter.

Appendix A

Overview of reduced-order observer

In the work of Katayama and Aoki [84], they considered a nonlinear sampled-data strict-feedback system as follows:

$$\begin{aligned} \dot{\zeta}_1 &= f_1(\zeta_1) + g_1(\zeta_1)\zeta_2 \\ \dot{\zeta}_2 &= f_2(\zeta_1, \zeta_2, u) \\ y_1(k) &= \zeta_1(kT) \end{aligned} \tag{A.1}$$

where $\zeta_1 \in \Re^{n_1}$ and $\zeta_2 \in \Re^{n_2}$ are continuous time states, $u \in \Re^m$ is the control input realized through a zero-order hold, and $y_1 \in \Re^{n_1}$ is a sampled-output from the sensor, and $T > 0$ is a sampling period. The system in Eq. (A.1) naturally appears in the digital control of mechanical systems where ζ_1 and ζ_2 express the position and velocity, respectively, and $y_1(k) = \zeta_1(kT)$ means that only the position measurement at each sampling time is available for control. It is also assumed that

A1: The mappings f_1, f_2, and g_1 are smooth over the compact domain of interest, $f_1(0) = 0$, and $f_2(0,0,0) = 0$.

A2: The $m \times m$ matrix $\Phi(\cdot) = g_1(\cdot)^T g_1(\cdot)$ is nonsingular and its inverse is bounded over the compact domain of interest.

Let $u(t) = u(kT) =: u(k)$ for any $t \in [kT, (k+1)T)$. Then the difference equations corresponding to the exact model and the Euler approximate model of the system in Eq. (A.1) are given by

$$\begin{aligned} \eta_1(k+1) &= \eta_1(k) + \int_{kT}^{(k+1)T} [f_1(\eta_1(s)) + g_1(\eta_1(s))\eta_2(s)]\mathrm{d}s \\ \eta_2(k+1) &= \eta_2(k) + \int_{kT}^{(k+1)T} [f_2(\eta_1(s), \eta_2(s), u(k))]\mathrm{d}s \\ y_1(k) &= \eta_1(k) \end{aligned} \tag{A.2}$$

and

$$\begin{aligned}\eta_1(k+1) &= \eta_1(k)+T[f_1(\eta_1(k))+g_1(\eta_1(k))\eta_2(k)]\\ \eta_2(k+1) &= \eta_2(k)+T[f_2(\eta_1(k),\eta_2(k),u(k))]\\ y_1(k) &= \eta_1(k),\end{aligned} \tag{A.3}$$

respectively. Note that $(\zeta_1,\zeta_2)(kT)=(\eta_1,\eta_2)(k)$ for the exact model. The exact model cannot be generally computable, and hence the Euler approximate model is used for design purpose. Then the following equation

$$\hat{\eta}_2(k+1)=(I-TH)\hat{\eta}_2(k)+TN_T(y_1(k),\rho y_1(k),u(k)) \tag{A.4}$$

can be a reduced-order observer of the Euler model in Eq. (A.3), where H=diag$\{h_1,\ldots,h_{n_2}\}$, $|1-Th_i|<1, i=1,\ldots,n_2$, ρ denotes the shift operator, *i.e.*, $(\rho y_1)(k)=y_1(k+1)$,

$$\begin{aligned}N_T(y_1,\rho y_1,u) &= H\Psi_T(y_1,\rho y_1)+f_2(y_1,\Psi_T(y_1,\rho y_1),u),\\ \Psi_T(y_1,\rho y_1) &= \Phi(y_1)^{-1}g_1(y_1)^T\left\{\frac{\rho y_1-y_1}{T}-f_1(y_1)\right\}.\end{aligned}$$

This observer is semiglobal and practical in T for the exact model in Eq. (A.2), *i.e.*, there exist $\beta\in\mathcal{KL}$ such that for any $D>d>0$ and the compact sets $\Omega_1\in\Re^{n_1}$, $\Omega_2\in\Re^{n_2}$, $U\in\Re^m$ we can find $T^*>0$ with the property that $||\eta_2(0)-\hat{\eta}_2(0)||\le D$ and $\eta_1(k)\in\Omega_1$, $\eta_2(k)\in\Omega_2$, and $u(k)\in U$ for any $k\ge 0$ imply $||\eta_2(k)-\hat{\eta}_2(k)||\le\beta(||\eta_2(0)-\hat{\eta}_2(0)||,kT)+d$ for all $T\in(0,T^*)$ [84], where $\beta\in\mathcal{KL}$ means that for any fixed $t\ge 0$, a function $\beta(\cdot,t)$ is continuous, zero at zero, strictly increasing, and for each fixed $s\ge 0$, $\beta(s,\cdot)$ is decreasing to zero as its argument tends to infinity [93]. The robustness of the observer in Eq. (A.4) against sampled observation noise was also discussed in [94].

Bibliography

[1] J.F. Roberts, J.-C. Zufferey, and D. Floreano. Energy management for indoor hovering robots. In *IEEE/RSJ International Conference on Intelligent Robots and Systems (IROS)*, pages 1242–1247, 2008.

[2] D. Aleksandrov and I. Penkov. Optimal gap distance between rotors of mini quadrotor helicopter. In *The 8th International Conference of DAAAM Baltic*, pages 251–255, 2012.

[3] E. Fresk and G. Nikolakopoulos. Experimental model derivation and control of a variable pitch propeller equipped quadrotor. In *IEEE Conference on Control Applications (CCA)*, pages 723–729, 2014.

[4] L. Luque-Vega, B. Castillo-Toledo, and A.G. Loukianov. Block linearization control of a quadrotor via sliding mode. In *American Control Conference (ACC)*, pages 149–154, 2012.

[5] M.R. Mokhtari and B. Cherki. A new robust control for minirotorcraft unmanned aerial vehicles. *ISA Transactions*, 56:86–101, 2015.

[6] E.H. Zheng, J.J. Xiong, and J.L. Luo. Second order sliding mode control for a quadrotor UAV. *ISA Transactions*, 53(4):1350–1356, 2014.

[7] R. Xu and U. Ozguner. Sliding mode control of a quadrotor helicopter. In *The 45th IEEE Conference on Decision and Control*, pages 4957–4962, 2006.

[8] M.O. Efe. Robust low altitude behavior control of a quadrotor rotorcraft through sliding modes. In *Mediterranean Conference on Control Automation*, pages 1–6, 2007.

[9] L.R. Garcia-Carrillo, E. Rondon, A. Dzul, A. Sanche, and R. Lozano. Hovering quad-rotor control: A comparison of nonlinear controllers using visual feedback. In *The 49th IEEE Conference on Decision and Control (CDC)*, pages 1662–1667, 2010.

[10] L. Luque-Vega, B. Castillo-Toledo, and Alexander G. Loukianov. Robust block second order sliding mode control for a quadrotor. *Journal of the Franklin Institute*, 349(2):719–739, 2012.

[11] F. Kendoul, D. Lara, I. Fantoni, and R. Lozano. Nonlinear control for systems with bounded inputs: Real-time embedded control applied to UAVs. In *The 45th IEEE Conference on Decision and Control (CDC)*, pages 5888–5893, 2006.

[12] E. Zheng and J. Xiong. Quad-rotor unmanned helicopter control via novel robust terminal sliding mode controller and under-actuated system sliding mode controller. *Optik-International Journal for Light and Electron Optics*, 125(12):2817–2825, 2014.

[13] S. Gonzalez-Vazquez and J. Moreno-Valenzuela. Motion control of a quadrotor aircraft via singular perturbations. *International Journal of Advanced Robotic Systems*, 10(368): 1–16, 2013.

[14] D. Lee, H. Jin Kim, and S. Sastry. Feedback linearization vs. adaptive sliding mode control for a quadrotor helicopter. *International Journal of Control, Automation and Systems*, 7 (3):419–428, 2009.

[15] E. Altug, J.P. Ostrowski, and C.J. Taylor. Control of a quadrotor helicopter using dual camera visual feedback. *The International Journal of Robotics Research*, 24(5):329–341, 2005.

[16] E. Altug, J.P. Ostrowski, and R. Mahony. Control of a quadrotor helicopter using visual feedback. In *IEEE International Conference on Robotics and Automation (ICRA)*, volume 1, pages 72–77, 2002.

[17] H. Bouadi and M. Tadjine. Nonlinear observer design and sliding mode control of four rotors helicopter. *International Journal of Engineering and Applied Sciences*, 3(6):333–338, 2007.

[18] A. Mokhtari and A. Benallegue. Dynamic feedback controller of euler angles and wind parameters estimation for a quadrotor unmanned aerial vehicle. In *IEEE International Conference on Robotics and Automation (ICRA)*, volume 3, pages 2359–2366, 2004.

[19] A. Mokhtari, N.K. M'Sirdi, K. Meghriche, and A. Belaidi. Feedback linearization and linear observer for a quadrotor unmanned aerial vehicle. *Advanced Robotics*, 20(1):71–91, 2006.

[20] A. Benallegue, A. Mokhtari, and L. Fridman. High-order sliding-mode observer for a quadrotor UAV. *International Journal of Robust and Nonlinear Control*, 18(4-5):427–440, 2008.

[21] S. Bouabdallah and R. Siegwart. Backstepping and sliding-mode techniques applied to an indoor micro quadrotor. In *IEEE International Conference on Robotics and Automation (ICRA)*, pages 2247–2252, 2005.

[22] A.A. Mian and W. Daobo. Modeling and backstepping-based nonlinear control strategy for a 6 DOF quadrotor helicopter. *Chinese Journal of Aeronautics*, 21(3):261–268, 2008.

[23] Qiong Hu, Qing Fei, Qinghe Wu, and Qingbo Geng. Research and application of nonlinear control techniques for quad rotor UAV. In *The 31st Chinese Control Conference (CCC)*, pages 706–710, 2012.

[24] L. Besnard, Y.B. Shtessel, and B. Landrum. Quadrotor vehicle control via sliding mode controller driven by sliding mode disturbance observer. *Journal of the Franklin Institute*, 349(2):658–684, 2012.

[25] Jun Li and Yuntang Li. Dynamic analysis and PID control for a quadrotor. In *International Conference on Mechatronics and Automation (ICMA)*, pages 573–578, 2011.

[26] G.M. Hoffmann, H.Huang, S.L. Waslander, and C.J. Tomlin. Precision flight control for a multi-vehicle quadrotor helicopter testbed. *Control Engineering Practice*, 19(9):1023–1036, 2011.

[27] P. Pounds, R. Mahony, and P. Corke. Modelling and control of a large quadrotor robot. *Control Engineering Practice*, 18(7):691–699, 2010.

[28] Paul E.I. Pounds, D.R. Bersak, and A.M. Dollar. Stability of small-scale UAV helicopters and quadrotors with added payload mass under PID control. *Autonomous Robots*, 33(1-2): 129–142, 2012.

[29] S. Bouabdallah, A. Noth, and R. Siegwart. PID vs LQ control techniques applied to an indoor micro quadrotor. In *IEEE/RSJ International Conference on Intelligent Robots and Systems (IROS)*, volume 3, pages 2451–2456, 2004.

[30] D. Lara, G. Romero, A. Sanchez, R. Lozano, and A. Guerrero. Robustness margin for attitude control of a four rotor mini-rotorcraft: Case of study. *Mechatronics*, 20(1):143–152, 2010.

[31] A. Tayebi and S. McGilvray. Attitude stabilization of a VTOL quadrotor aircraft. *IEEE Transactions on Control Systems Technology*, 14(3):562–571, 2006.

[32] Yushu Yu, Xilun Ding, and J. Jim Zhu. Attitude tracking control of a quadrotor UAV in the exponential coordinates. *Journal of the Franklin Institute*, 350(8):2044–2068, 2013.

[33] ZeFang He and L. Zhao. A simple attitude control of quadrotor helicopter based on ziegler-nichols rules for tuning PD parameters. *The Scientific World Journal*, 2014:1–13, 2014.

[34] S.A. Al-Hiddabi. Quadrotor control using feedback linearization with dynamic extension. In *The 6th International Symposium on Mechatronics and its Applications (ISMA)*, pages 1–3, 2009.

[35] H. Voos. Nonlinear control of a quadrotor micro-UAV using feedback-linearization. In *IEEE International Conference on Mechatronics (ICM)*, pages 1–6, 2009.

[36] N. Sydney, B. Smyth, and D.A. Paley. Dynamic control of autonomous quadrotor flight in an estimated wind field. In *The 52nd IEEE Annual Conference on Decision and Control (CDC)*, pages 3609–3616, 2013.

[37] J. Ghandour, S. Aberkane, and J-C. Ponsart. Feedback linearization approach for standard and fault tolerant control: Application to a quadrotor UAV testbed. *Journal of Physics: Conference Series*, 570(8):1–11, 2014.

[38] DongBin Lee, T.C. Burg, D.M. Dawson, Dule Shu, Bin Xian, and Enver Tatlicioglu. Robust tracking control of an underactuated quadrotor aerial-robot based on a parametric uncertain model. In *IEEE International Conference on Systems, Man and Cybernetics (SMC)*, pages 3187–3192, 2009.

[39] Pedro Castillo, A. Dzul, and R. Lozano. Real-time stabilization and tracking of a four-rotor mini rotorcraft. *IEEE Transactions on Control Systems Technology*, 12(4):510–516, 2004.

[40] J.F. Guerrero-Castellanos, N. Marchand, A. Hably, S. Lesecq, and J. Delamare. Bounded attitude control of rigid bodies: Real-time experimentation to a quadrotor mini-helicopter. *Control Engineering Practice*, 19(8):790 797, 2011.

[41] S. Salazar-Cruz, A. Palomino, and R. Lozano. Trajectory tracking for a four rotor mini-aircraft. In *The 44th IEEE Conference on Decision and Control and European Control Conference (CDC-ECC)*, pages 2505–2510, 2005.

[42] H. Bouadi, M. Bouchoucha, and M. Tadjine. Modelling and stabilizing control laws design based on sliding mode for an UAV type-quadrotor. *Engineering Letters*, 15(2):1–6, 2007.

[43] B. Sumantri, N. Uchiyama, and S. Sano. Least square based sliding mode control for a quad-rotor helicopter. In *IEEE/SICE International Symposium on System Integration (SII)*, pages 324–328, 2013.

[44] S.L. Waslander, G.M. Hoffmann, Jung Soon Jang, and C.J. Tomlin. Multi-agent quadrotor testbed control design: integral sliding mode vs. reinforcement learning. In *IEEE/RSJ International Conference on Intelligent Robots and Systems (IROS)*, pages 3712–3717, 2005.

[45] X. Gong, Z.C. Hou, C.J. Zhao, Y. Bai, and Y.T. Tian. Adaptive backstepping sliding mode trajectory tracking control for a quad-rotor. *International Journal of Automation and Computing*, 9(5):555–560, 2012.

[46] F. Sharifi, M. Mirzaei, B.W. Gordon, and Y. Zhang. Fault tolerant control of a quadrotor UAV using sliding mode control. In *Conference on Control and Fault-Tolerant Systems (SysTol)*, pages 239–244, 2010.

[47] A. Das, F.L. Lewis, and K. Subbarao. *Sliding Mode Approach to Control Quadrotor Using Dynamic Inversion*, pages 3–24. InTech, 2011.

[48] H.A.F. Mohamed, S.S. Yang, and M. Moghavvemi. Sliding mode controller design for a flying quadrotor with simplified action planner. In *ICCAS-SICE, 2009*, pages 1279–1283, 2009.

[49] A.R. Patel, M.A. Patel, and D.R. Vyas. Modeling and analysis of quadrotor using sliding mode control. In *The 44th Southeastern Symposium on System Theory (SSST)*, pages 111–114, 2012.

[50] M. Guisser and H. Medromi. A high gain observer and sliding mode controller for an autonomous quadrotor helicopter. *International Journal of Intelligent Control and Systems*, 14(3):204–212, 2009.

[51] J.J. Xiong and E.H. Zheng. Position and attitude tracking control for a quadrotor UAV. *ISA Transactions*, 53(3):725 – 731, 2014.

[52] L. Derafa, L. Fridman, A. Benallegue, and A. Ouldali. Super twisting control algorithm for the four rotors helicopter attitude tracking problem. In *The 11th International Workshop on Variable Structure Systems (VSS)*, pages 62–67, 2010.

[53] M. Bouchoucha, S. Seghour, and M. Tadjine. Classical and second order sliding mode control solution to an attitude stabilization of a four rotors helicopter: From theory to experiment. In *IEEE International Conference on Mechatronics (ICM)*, pages 162–169, 2011.

[54] L. Derafa, A. Benallegue, and L. Fridman. Super twisting control algorithm for the attitude tracking of a four rotors UAV. *Journal of the Franklin Institute*, 349(2):685–699, 2012.

[55] B. Sumantri, N. Uchiyama, and S. Sano. Second order sliding mode control for a quadrotor helicopter with a nonlinear sliding surface. In *IEEE Conference on Control Applications (CCA)*, pages 742–746, 2014.

[56] U. Itkis. *Control Systems of Variable Structure*. New York: John Wiley & Sons Inc., 1976.

[57] V. Utkin. Variable structure systems with sliding modes. *IEEE Transactions on Automatic Control*, 22(2):212–222, 1977.

[58] J.Y. Hung, W. Gao, and J.C. Hung. Variable structure control: a survey. *IEEE Transactions on Industrial Electronics*, 40(1):2–22, 1993.

[59] J.J.E. Slotine and W. Li. *Applied Nonlinear Control*. New Jersey: Prentice Hall, 1991.

[60] N. Promkajin and M. Parnichkun. Attitude and altitude control of a four-rotor hovercraft using sliding mode control with adaptive sliding surface. In *IEEE International Conference on Robotics and Biomimetics (ROBIO)*, pages 1285–1290, 2011.

[61] V. Utkin and Jingxin Shi. Integral sliding mode in systems operating under uncertainty conditions. In *The 35th IEEE Conference on Decision and Control (CDC)*, volume 4, pages 4591–4596, 1996.

[62] K. Nonaka and H. Sugizaki. Integral sliding mode altitude control for a small model helicopter with ground effect compensation. In *American Control Conference (ACC)*, pages 202–207, 2011.

[63] F. Piltan, N. Sulaiman, S. Soltani, M.H. Marhaban, and R. Ramli. An adaptive sliding surface slope adjustment in PD sliding mode fuzzy control for robot manipulator. *International Journal of Control and Automation*, 4(3):65–76, 2011.

[64] A. Kareem and M.F. Azeem. A novel adaptive super-twisting sliding mode controller with a single input-single output fuzzy logic control based moving sliding surface. *International Journal of Control and Automation*, 6(3):183–197, 2013.

[65] F. Yorgancioglu and H. Komurcugil. Decoupled sliding-mode controller based on time-varying sliding surfaces for fourth-order systems. *Expert Systems with Applications*, 37 (10):6764 – 6774, 2010.

[66] T. Orowska-Kowalska, M. Kaminski, and K. Szabat. Implementation of a sliding-mode controller with an integral function and fuzzy gain value for the electrical drive with an elastic joint. *IEEE Transactions on Industrial Electronics*, 57(4):1309–1317, 2010.

[67] M.U. Salamci and G.S. Tombul. Sliding mode control design with time varying sliding surfaces for a class of nonlinear systems. In *IEEE International Conference on Control Applications*, pages 996–1001, 2006.

[68] S. Tokat, I. Eksin, and M. Guzelkaya. Sliding mode control using a nonlinear time-varying sliding surface. In *The 10th Mediterranean Conference on Control and Automation*, pages 1–6, 2002.

[69] C. Binglong, L. Xiangdong, and C. Zhen. Exponential time-varying sliding mode control for large angle attitude eigenaxis maneuver of rigid spacecraft. *Chinese Journal of Aeronautics*, 23(4):447–453, 2010.

[70] D. Fulwani, B. Bandyopadhyay, and L. Fridman. Non-linear sliding surface: towards high performance robust control. *Control Theory Applications, IET*, 6(2):235–242, 2012.

[71] Abd El Khalick Mohammad, A.M., N. Uchiyama, and S. Sano. Energy saving in feed drive systems using sliding-mode-based contouring control with a nonlinear sliding surface. *IEEE/ASME Transactions on Mechatronics*, 20(2):572–579, 2015.

[72] S. Mobayen. An LMI-based robust controller design using global nonlinear sliding surfaces and application to chaotic systems. *Nonlinear Dynamics*, 79(2):1075–1084, 2015.

[73] A. Boubakir, F. Boudjema, and S. Labiod. A neuro-fuzzy-sliding mode controller using nonlinear sliding surface applied to the coupled tanks system. *International Journal of Automation and Computing*, 6(1):72–80, 2009.

[74] A. Boubakir, F. Boudjema, C. Boubakir, and S. Labiod. A fuzzy sliding mode controller using nonlinear sliding surface applied to the coupled tanks system. *International Journal of Fuzzy Systems*, 10(2):112–118, 2008.

[75] Wen-Jun Cao and Jian-Xin Xu. Nonlinear integral-type sliding surface for both matched and unmatched uncertain systems. *IEEE Transactions on Automatic Control*, 49(8):1355–1360, 2004.

[76] S. Mondal and C. Mahanta. Nonlinear sliding surface based second order sliding mode controller for uncertain linear systems. *Communications in Nonlinear Science and Numerical Simulation*, 16(9):3760–3769, 2011.

[77] Qinglei Hu. Variable structure maneuvering control with time-varying sliding surface and active vibration damping of flexible spacecraft with input saturation. *Acta Astronautica*, 64(11–12):1085–1108, 2009.

[78] A. Levant. Sliding order and sliding accuracy in sliding mode control. *International Journal of Control*, 58(6):1247–1263, 1993.

[79] J.A. Moreno and M. Osorio. A lyapunov approach to second-order sliding mode controllers and observers. In *The 47th IEEE Conference on Decision and Control (CDC)*, pages 2856–2861, 2008.

[80] J.A. Moreno. A linear framework for the robust stability analysis of a generalized super-twisting algorithm. In *6th International Conference on Electrical Engineering, Computing Science and Automatic Control*, pages 1–6, 2009.

[81] I.A. Raptis and K.P. Valavanis. *Linear and Nonlinear Control of Small-Scale Unmanned Helicopter*. Springer, 2011.

[82] T. Hamel, R. Mahony, R. Lozano, and J. Ostrowski. Dynamic modelling and configuration stabilization for an X4-flyer. In *The 15th IFAC World Congress*, volume 15, pages 846–846, 2002.

[83] B. Sumantri, N. Uchiyama, and S. Sano. Least square based sliding mode control for a quad-rotor helicopter and energy saving by chattering reduction. *Mechanical Systems and Signal Processing*, 66–67:769–784, 2016.

[84] H. Katayama and H. Aoki. Reduced-order observers for nonlinear sampled-data systems with application to marine systems. In *The 52nd IEEE Annual Conference on Decision and Control (CDC)*, pages 5072–5077, 2013.

[85] N.S. Nise. *Control Systems Engineering-6th edition*. John Wiley & Sons Inc., 2011.

[86] B. Sumantri, N. Uchiyama, and S. Sano. Robust tracking control of a quad-rotor helicopter utilizing sliding mode control with a nonlinear sliding surface. *Journal of System, Design and Dynamics*, 7(2):226–241, 2013.

[87] T. Orowska-Kowalska, M. Kaminski, and K. Szabat. Implementation of a sliding-mode controller with an integral function and fuzzy gain value for the electrical drive with an elastic joint. *IEEE Transactions on Industrial Electronics*, 57(4):1309–1317, 2010.

[88] R. de Castro, R.E. Araujo, and D. Freitas. Wheel slip control of EVs based on sliding mode technique with conditional integrators. *IEEE Transactions on Industrial Electronics*, 60(8): 3256–3271, 2013.

[89] B. Beltran, T. Ahmed-Ali, and M. Benbouzid. High-order sliding-mode control of variable-speed wind turbines. *IEEE Transactions on Industrial Electronics*, 56(9):3314–3321, 2009.

[90] Alexander G. Loukianov, J.M. Canedo, L.M. Fridman, and A. Soto-Cota. High-order block sliding-mode controller for a synchronous generator with an exciter system. *IEEE Transactions on Industrial Electronics*, 58(1):337–347, 2011.

[91] B. Sumantri, N. Uchiyama, and S. Sano. Generalized super-twisting sliding mode control with a nonlinear sliding surface for robust and energy efficient control of a quad-rotor helicopter. *Journal of Mechanical Engineering Science*, submitted on April, 4th, 2015.

[92] L. Fridman and A. A. Levant. *Sliding Mode Control In Engineering: Higher order sliding modes*. New York: Marcel Dekker Inc., 2002.

[93] H.K. Khalil. *Nonlinear Systems*. Prentice Hall, 2002.

[94] H. Katayama and H. Aoki. Straight-line trajectory tracking control for sampled-data underactuated ships. *IEEE Transactions on Control Systems Technology*, 22(4):1638–1645, 2014.

Publications

Journal papers:

1. Bambang Sumantri, Naoki Uchiyama, Shigenori Sano, and Yuma Kawabata, Robust tracking control of a quad-rotor helicopter utilizing sliding mode control with a nonlinear sliding surface, Journal of System Design and Dynamics, vol. 7, no. 2, pp. 226-241, 2013.

2. Bambang Sumantri, Naoki Uchiyama, and Shigenori Sano, Least square based sliding mode control for a quad-rotor helicopter and energy saving by chattering reduction, Mechanical Systems and Signal Processing, vol. 66–67, pp. 769–784, 2016. (*5-Year Impact Factor: 2.870*)

Conference papers:

1. Bambang Sumantri, Naoki Uchiyama, Shigenori Sano, and Yuma Kawabata, "Sliding mode control of a quad rotor helicopter using nonlinear sliding surface," 18th International Symposium on Artificial Life and Robotics (ISAROB), Daejeon, Korea, 2013.

2. Bambang Sumantri, Naoki Uchiyama, and Shigenori Sano, "Least square based sliding mode control for a quad-rotor helicopter," IEEE/SICE International Symposium on System Integration (SII), Kobe, Japan, 2013.

3. Bambang Sumantri, Naoki Uchiyama, and Shigenori Sano, "Second order sliding mode control for a quad-rotor helicopter with a nonlinear sliding surface," IEEE Conference on Control Applications (CCA) Part of IEEE Multi-conference on Systems and Control, Antibes, France, 2014.

Acknowledgements

All praises are to ALLAH, the most beneficent and merciful, the Lord of universe. Without His blessings, this works could not be accomplished.

I would like to express my deep appreciation to Prof. Naoki Uchiyama for his sincere advice and passionate guidance. I have learned not only scientific knowledge, but also the method of scientific thinking, how to identify the problems and formulate the method to find the solutions. I have also learned much about how to communicate an idea to other people so that it could be understandable and acceptable.

I would like to express my gratitude to the committee members, Prof. Kazuhiko Terashima and Prof. Shinichi Suzuki, for their great support and valuable advice and comments. I also would like to thank to Assoc. Prof. Shigenori Sano, Assoc. Prof. Hitoshi Katayama, and Assistant Prof. Tatsuhiko Sakaguchi for giving me valuable discussions and suggestions in completion of this work. In addition, I also would like to thank to all members of Robotics and Mechatronics Laboratory for their assistance and friendship during my study.

Furthermore, I would like to thank to DIKTI (Directorate General of Higher Education, Indonesia) for providing me scholarship during my study and Electronic Engineering Polytechnic Institute of Surabaya (EEPIS) which gives me the chance and support to study at Toyohashi University of Technology. I also would like to thank to Hori Sciences and Arts Foundation for their financial support and thanks to all Toyohashi University staff members for their kindly assistance and friendship.

With my endless love, I am grateful to my wife Catur Arik Kurniawati. Her love, patience, encouragement, and support are undeniably. Her understanding and tolerance during accompanying me is a testament of her unyielding devotion and love. To my daughter and son, Hana-Chan and Kei-Kun, you give me spirit and inspiration.

I extend my sincere gratitude to my parents for their endless support, supplication, sacrifice, and unconditional love. I also thank to my brothers, sisters, and all my family for your encouragement, support, and supplication.

Last but not least, I would like to thank to Batch-I of EEPIS-TUT collaboration, Agus-san, Bima-san, and Hero-san, PPI (Indonesian Student Association) members, and Toyohashi Muslim Community for brotherhood and togetherness. I also would like to thank to Pak Udin and family for your help and kindness during me and my family live in Toyohashi.

Bambang Sumantri